KU LEUVEN

ARENBERG DOCTORAL SCHOOL
Faculty of Science

The influence of magnetic fields on light–matter interaction

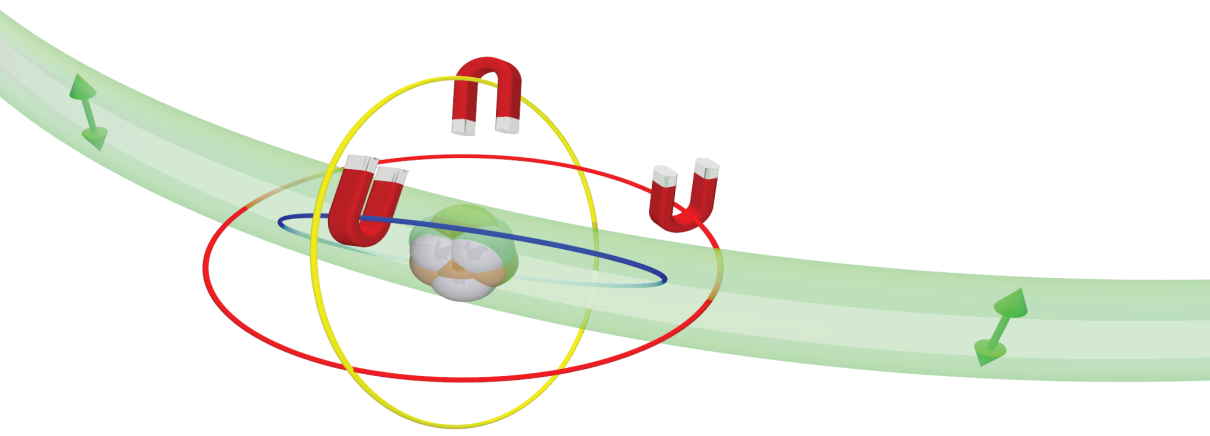

Stefaan Vandendriessche

Dissertation presented in partial fulfillment of the requirements for the degree of Doctor in Science

May 2014

The influence of magnetic fields on light–matter interaction

Stefaan VANDENDRIESSCHE

Supervisory Committee:
Prof. Dr. Koen Clays, chair
Prof. Dr. Thierry Verbiest, supervisor
Dr. Ventsislav K. Valev, co-supervisor
Prof. Dr. Guy Koeckelberghs
Prof. Dr. Tatjana Vogt
Prof. Dr. Steven De Feyter
Prof. Dr. André Persoons
Prof. Dr. Peter A. Bobbert
(Technische Universiteit Eindhoven)

Dissertation presented in partial fulfillment of the requirements for the degree of Doctor in Science

May 2014

Uitgegeven in eigen beheer, Stefaan Vandendriessche, Celestijnenlaan 200D box 2425, B-3001 Heverlee (Belgium)

ISBN 978-90-8649-706-5

D/2014/10.705/15

Preface

As a child, my dream was to follow in my parent's footsteps and complete a PhD in exact sciences. Initially I did not want to follow the exact same academic track, so I even briefly considered engineering. Finally I decided to start a bachelor in biochemistry. Despite my attempts to avoid it, it turns out there is a genotype-environment correlation for studying chemistry, which inevitably led me to a master in chemistry. It was while writing my master's thesis that Thierry turned my attention to physical chemistry, and more specifically to nonlinear and magneto-optics. The result is the booklet you hold in your hands (or the pdf you are reading on your screen).

This thesis would never have come to fruition without the unwavering, unquestioning support of my parents. They provided me with the best environment imaginable for me to develop and discover the world. Words fail to express my gratitude for their hard work and for putting up with me. My mother never missed an opportunity to make our childhood a happy one, and though she is not here to see the result, this thesis would never even have started without her care. Without the many late-night chess sessions with my father I might never have developed the skills necessary to pursue a PhD, and his incessant drive and KISS attitude greatly shaped me. Finally, reading Jurassic Park with both of my parents before going to bed is the first scientific memory I have, and it was undoubtedly the start of the scientific curiosity necessary to complete a PhD.

Though she entered my life at a later stage, Mieke was instrumental to this thesis as well. I want to thank her for caring deeply for me, knowing precisely how to relax me but also when to motivate me, and for accepting the many late nights. The joy she brings me gave me the energy and drive necessary to finish this thesis. Not only this thesis but my life would not be complete without her and her playful smile.

My “home” environment was also essential for the work you are reading. Thanks to Annemie for her great cooking, being there for us and for making my father happy. Mary was a great Spanish connection, and I would like to thank her for her linguistic help and view on things. Titi’s graphic design expertise and creativity formed the base of my graphic abilities, which – though they remain limited – have improved.

During lunch break, after work hours and even abroad, my friends were a great source of inspiration and relaxation. I wouldn’t have made it through these four years without the countless liters of ice cream I both received and bought. You guys were great Gio, Jolien, Koen, P.-J., Wouter, Tine and Ward.

On campus, Thierry provided me with just the right work environment. He gave me great independence and freedom, but was always there with the right answers when I got stuck. His door was always open, and regardless of the state you entered his office in, his motivational skills and scientific knowledge ensured that you left his office smiling, with a plan on how to finally grasp that elusive Science article.

Ventsi’s diligence and scientific drive were just the introduction I needed into experimental nonlinear and magneto-optics, and though sometimes initially time-consuming, his advice and methodology ended up saving me many hours of wasted PhD time. Guy’s knowledge of the behavior of organic molecules such as polythiophenes, along with his willingness to synthesize anything scientifically possible was also instrumental to this thesis.

Thanks to my LCBD and other colleagues who made 200D a fun place to work in; the cake was awesome! In particular thanks to Bram, Kevin, P.-J., Stefan and Steven. With Maarten, Maarten and Ward present, the office was never a dull place, and each time we played Gangnam style was better than the last. A special note of thanks needs to go to Frans and Rik: more than just support engineers, their ideas helped shape my research and many of my unusual ideas could never have been tested without their skills and insight. Finally thanks to Pieter; without him the liquid crystal article would still be a draft waiting for more product.

It is not easy to make the time to read an entire thesis, especially with a busy schedule. For this reason I would like to thank my examination committee. Thank you for your time and effort Prof. K. Clays, Prof. G. Koeckelberghs, Prof. T. Vogt, Prof. S. De Feyter and Prof. A. Persoons. A specific word of thanks to Prof. P. Bobbert for crossing international borders in order to evaluate my thesis.

Finally I would like to thank FWO-Vlaanderen for financing me with an Aspirant fellowship: it turns out all the studying might have been worth it after all.

Abstract

In this dissertation we sought to improve the understanding of the influence of magnetic fields on light–matter interaction. While this influence is small, it is crucial for optical communication as well as next-generation networks. It was discovered almost two centuries ago and was initially characterized in glass by Michael Faraday, who stated "Still, I have at last succeeded in illuminating a magnetic curve or line of force, and in magnetizing a ray of light…". Since then great progress has been made in understanding Faraday rotation as well as other magneto-optical effects, and they have become an important but unseen part of everyday life. From our perspective of nonlinear optics we sought to contribute to the field of magneto-optics.

We built a setup in order to magneto-optically characterize materials. This setup contains a single photoelastic modulator and simultaneously measures circular dichroism, circular birefringence, magnetic circular dichroism and Faraday rotation. Because of the importance of this setup to this dissertation, we analyzed it and verified the measurements, both in an ideal framework and taking into account photoelastic modulator non-idealities.

As with other nonlinear optical effects, scientists first investigated Faraday rotation in inorganic materials. However, organic materials provide many advantages over inorganic materials, such as flexibility in processing and synthesis, leading to our initial focus on organic materials. Using both computational methods and experimental measurements, we created a model to predict the Faraday rotation of organic compounds. Our model accurately predicts the Faraday rotation of small organic compounds in a wavelength region off-resonance, and can be expanded to include larger molecules or additional chemical groups. Despite the usefulness of calculating or predicting the Faraday rotation of molecules off-resonance, we subsequently demonstrated that resonance can have an important effect on Faraday rotation. We observed giant Faraday rotation in a class of mesogenic organic molecules, and we hypothesize that it is caused by resonance with a triplet state at that energy.

This hypothesis is strengthened by time-dependent density functional theory calculations revealing triplet transitions close to these wavelengths.

Certain inorganic materials also warrant further investigation for magneto-optical effects. Superparamagnetic nanoparticles offer an interesting combination of relatively easy synthesis, flexibility in processing and sample preparation and a very strong magnetic response. We therefore chose to analyze their behavior in alternating current magnetic field measurements. They show a characteristic response at the uneven harmonics of the applied magnetic field strength frequency. This enables rapid identification and analysis, even in complex samples consisting of multiple types of magnetic materials. Subsequently we showed that superparamagnetic nanoparticles also hold promise for higher order nonlinear optical measurements such as magnetization-induced second harmonic generation.

Our results improved the understanding of the influence of magnetic fields on light–matter interaction. Progress has been made in understanding the optical response of both organic materials and superparamagnetic materials in a magnetic field. Both materials show promise for further fundamental research as well as practical applications such as magnetometers and magnetoencephalography. In addition, our results provide a solid basis that future research can build on in order to deepen the understanding of the influence of a magnetic field on light–matter interactions.

Beknopte samenvatting

Dit doctoraatsproefschrift heeft als doel de invloed van magnetische velden op licht–materie interactie beter te begrijpen. Het bestaan van deze invloed bewees Michael Faraday bijna twee eeuwen geleden door metingen in glas. Sinds die eerste metingen is het onderzoeksveld enorm gevorderd en is het begrip van Faradayrotatie en andere magneto-optische effecten sterk gebeterd. Vanuit ons perspectief van de niet-lineaire optica wilden wij aan dit begrip bijdragen.

Om het onderzoeksveld te verrijken is een experimentele setup nodig die materialen magneto-optisch kan karakteriseren. Wij bouwden, kalibreerden en testten een setup die met gebruik van een enkele photoelastic modulator simultaan circulair dichroïsme, circulaire dubbele breking, magnetische circulair dichroïsme en Faradayrotatie meet. Omdat deze setup aan de basis ligt van onze verdere metingen en experimenten, hebben wij hem eerst grondig gekarakteriseerd.

Net als bij andere niet-lineaire optische effecten hebben wetenschappers oorspronkelijk Faradayrotatie onderzocht in anorganische materialen. Omdat organische materialen veel voordelen bieden ten opzichte van anorganische materialen, zoals hun flexibiliteit in verwerking en synthese, hebben wij ons onderzoek initieel gericht op organische materialen. Door vergelijkingen van computationele berekeningen met experimentele metingen ontwikkelden wij een model om de Faradayrotatie van kleine organische moleculen te voorspellen. Het model werkt in golflengtegebieden verwijderd van resonantie en is zo opgebouwd dat het uitgebreid kan worden naar grotere moleculen of bijkomende functionele groepen. Ondanks het nut van het berekenen van Faradayrotatie in golflengtegebieden verwijderd van resonantie hebben wij daarna aangetoond dat resonantie een belangrijke invloed kan hebben op de Faradayrotatie. Wij namen gigantische Faradayrotatie waar op een klasse van moleculen met vloeibare kristallijne eigenschappen. Onze hypothese is dat deze gigantische Faradayrotatie veroorzaakt wordt door resonantie met een triplet toestand dichtbij die energie. Wij onderbouwen deze hypothese met tijdsafhankelijke

dichtheidsfunctionaaltheorie berekeningen waarin triplet transities dichtbij deze energieën te vinden zijn.

Buiten de nieuwe organische materialen zijn er nog steeds anorganische materialen waarop verder magneto-optisch onderzoek nuttig kan zijn. Superparamagnetische nanopartikels bieden een uitstekende combinatie van relatief eenvoudige synthese, flexibiliteit in staalvoorbereiding en -verwerking en een zeer sterke magnetische respons. Daarom hebben wij hun gedrag geanalyseerd in metingen met een wisselend magneetveld. Deze nanopartikels vertonen een karakteristieke respons bij de oneven harmonischen van de frequentie van het aangelegde magneetveld, waardoor ze zelfs in complexe stalen snel geïdentificeerd en geanalyseerd kunnen worden. Verdere metingen in constante magneetvelden toonden hun beloftevolle eigenschappen aan voor hogere orde niet-lineaire optische metingen zoals magnetisch geïnduceerde tweede harmonische generatie.

Onze resultaten hebben bijgedragen tot het begrijpen van de invloed van magnetische velden op licht–materie interactie. Wij hebben vooruitgang geboekt in het verstaan van de optische respons van zowel organische materialen als superparamagnetische materialen in een magneetveld. Beide soorten materialen tonen zijn veelbelovend voor zowel toekomstig, fundamenteel onderzoek als in verscheidene toepassingen zoals magnetometers en magnetoencephalografie. De in dit onderzoek verkregen resultaten bieden een vruchtbare basis voor verder onderzoek naar het optisch gedrag van deze materialen in een magneetveld.

List of abbreviations

6-31+G**	split valence Pople basis functions with the addition of diffuse functions and polarized functions on all atoms
AC	alternating current
aug-cc-pVDZ	Dunning double-ζ basis set augmented with diffuse functions
B3LYP	Becke three-parameter Lee–Yang–Parr exchange-correlation functional
BHLYP	Becke half-and-half Lee–Yang–Parr exchange-correlation functional
BP	Becke-Perdew
BTB*	1,3-bis[(*S*)-3,7-dimethyloctyloxy)]-5-fluoro-2,4,6-tris[(4-nitrophenyl)ethynyl]-benzene
CB	circular birefringence
CCCBDB	computational chemistry comparison and benchmark database
CD	circular dichroism
CGS units	centimeter–gram–second system of units
DC	direct current
DFG	difference frequency generation
DFT	density functional theory
DFWM	degenerate four-wave mixing
EOM	electro-optic modulator
HF	Hartree-Fock
HSE	Health, Safety & Environment
KISS	keep it simple stupid
LHCP	left-handed circularly polarized

LIA	lock-in amplifier
MCD	magnetic circular dichroism
MP2	Møller–Plesset perturbation theory up to the second order
MRI	magnetic resonance imaging
MSHG	magnetization-induced second harmonic generation
MTBE	methyl *tert*-butyl ether
MTHG	magnetization-induced third harmonic generation
NCB	natural circular birefringence
NMR	nuclear magnetic resonance
PEM	photoelastic modulator
PMMA	poly(methyl methacrylate)
PMT	photomultiplier tube
RHCP	right-handed circularly polarized
RPA	random phase approximation
SHG	second harmonic generation
SI units	International System of Units
SQUID	superconducting quantum interference device
TD-DFT	time-dependent density functional theory
TDA	Tamm-Dancoff approximation
THF	tetrahydrofuran
THG	third harmonic generation
THP	tetrahydropyran
TTB	1,3,5-tris[(4-nitrophenyl)ethynyl]-2,4,6-tris(*n*-decyloxy)benzene
TTB*	1,3,5-tris[(*S*)-3,7-dimethyloctyloxy]-2,4,6-tris[(4-nitrophenyl)ethynyl]benzene
TZVP	triple-ζ polarized
UV	ultraviolet
VSM	vibrating sample magnetometer
WP	Wollaston prism

List of symbols

B	magnetic induction
$\chi^{(1),mm}$	magnetic susceptibility
$\chi^{(2),eee}$	second order electric susceptibility
d	length of propagation
δ	dynamic retardation of a photoelastic modulator
E	electric field
H	applied magnetic field strength
k	wave vector of light
k_B	Boltzmann constant
λ	wavelength of light
M	magnetization
m	magnetic moment
M_S	saturation magnetization
μ_0	magnetic permeability of vacuum
μ	magnetic permeability
n	refractive index
ω	frequency of light
P	polarization
T	temperature
θ	Faraday rotation
V	Verdet constant

Contents

Chapter 1

Introduction

This PhD dissertation investigates the interaction of light and matter in the presence of a magnetic field. While the influence of magnetic fields on light–matter interaction may seem far removed from our everyday world, this effect in fact plays an important role in the technology we use in our day-to-day lives. Magneto-optically active elements such as optical isolators are essential for lasers and for fiber optics, and their importance in next-generation networks should not be underestimated. Magneto-optic measurements on the other hand are essential for data storage and retrieval, the visualization and measurement of magnetic fields and are even applied in anti-counterfeiting measures. To understand these important interactions, a rudimentary understanding of "classical" linear optics is necessary, as described in section 1.1.1. However, the influence of a magnetic field is best described in the context of nonlinear optics, which is elaborated upon in section 1.1.2. The specific magnetic field effects studied in this dissertation are analyzed in detail in sections 1.2 and 1.3, culminating in our research focus in section 1.4.

1.1 Introduction to linear and nonlinear optics

1.1.1 Linear optics

Light is a type of electromagnetic radiation that consists of a time and space varying electric field perpendicular to a time and space varying magnetic field. Light traveling in the z-direction can be described by the solutions to Maxwell's

equations[1]

$$\vec{E}(z,t) = \vec{E}_0 \sin(kz - \omega t) \tag{1.1}$$

$$\vec{B}(z,t) = \vec{B}_0 \sin(kz - \omega t) \tag{1.2}$$

where $\vec{E}(z,t)$ and $\vec{B}(z,t)$ are the electric field and the magnetic induction of light, which are perpendicular to each other. $\vec{E}_0$ and $\vec{B}_0$ are the amplitudes of the electric field and magnetic induction of light, k is the wave vector and $w = 2\pi f$ where f is the frequency of the light. k and f are related by $k = \frac{2\pi f n}{c} = \frac{2\pi n}{\lambda}$, where n is the refractive index, c is the speed of light and λ is the wavelength of the light.

The time-varying electric field of light will interact with charges: positive charges will move in the direction of the field and negative charges will move in the opposite direction. Because matter contains negatively charged electrons and positively charged protons, light will interact with matter when passing through it. Protons have a far greater mass than electrons, and therefore move less on the timescales of the electric field of light than electrons. This means we can approximate the interaction of light with matter as electrons moving away from their equilibrium positions around static nuclei, creating induced dipole moments $\mu(\omega)$ that oscillate with the same frequency ω as the electric field of light. For a single molecule, this is written as[2]

$$\mu(\omega) = \alpha(\omega) E(\omega) \tag{1.3}$$

with $\alpha(\omega)$ the molecular first-order polarizability and $E(\omega)$ the electric field of light. Because measurements almost always probe more than one molecule, we need to relate this to the induced polarization of the entire medium $P(\omega)$

$$P(\omega) = N f_\omega \alpha(\omega) E(\omega) = \chi^{(1),ee}(\omega) E(\omega) \tag{1.4}$$

where N is the number density of the molecules. f_ω, a local field factor, takes into account the changes in the incident light field due to the induced dipoles. $\chi^{(1),ee}(\omega)$ is the first-order electric susceptibility, which can be understood as a macroscopic version of the molecular first-order electric polarizability $\alpha(\omega)$. The first e in the ee superscript indicates that $\chi^{(1),ee}(\omega)$ refers to an induced electric polarization. The second e indicates that the cause of the polarization described by $\chi^{(1),ee}(\omega)$ is an electric field. Finally, the 1 indicates this is a linear or first-order susceptibility. This induced polarization at frequency ω leads to light emission at frequency ω. We can now include magnetic fields in this expression; defining magnetization using the following three susceptibilities

$$P(\omega) = \chi^{(1),ee}(\omega) E(\omega) + \chi^{(1),em}(\omega) B(\omega) \tag{1.5}$$

$$M(\omega) = \chi^{(1),me}(\omega) E(\omega) + \chi^{(1),mm}(\omega) B(\omega) \tag{1.6}$$

where an m as a first letter in the superscript indicates that we are describing an induced magnetization, and an m as a second letter indicates that the induced effect is caused by a magnetic field strength. The magnetic terms are typically much smaller than the electric terms; hence they are frequently approximated to be 0. This dissertation demonstrates that magnetic terms can indeed be relevant, but it is instructive to first understand the electric terms before continuing on to the magnetic terms.

P, E, μ and α depend on the frequency of light ω, but in the rest of this thesis, we will omit the explicit ω where it is obvious from the context or not essential in order to lighten notation. $\chi^{(1),ee}$ is also frequency-dependent, but the dependence is somewhat more complex. A susceptibility $\chi^{(n)}$ describes the interaction of $n-1$ electric or magnetic waves $\omega_0, \omega_1, \ldots \omega_{n-1}$ to create a new electric or magnetic wave ω_m. $\chi^{(n)}$ depends on the frequency of all of these waves. To make this clear we write[3] $\chi^{(n)}(-\omega_m; \omega_0, \omega_1, \ldots \omega_{n-1})$. However, seeing as this is a very heavy notation, we will again omit this notation where obvious or not essential. Because of the law of conservation of energy, for $\chi^{(1)}$ the frequency of the new wave must be the same as the incident wave, and so we can write $\chi^{(1)}(-\omega; \omega) = \chi^{(1)}(\omega)$.

In the expression for the polarization of the medium eq. (1.4), P and E are vectors (or rank 1 tensors, see appendix A), and $\chi^{(1),ee}$ is a rank 2 tensor consisting of 9 elements. We can make this explicit by writing

$$\begin{bmatrix} P_x \\ P_y \\ P_z \end{bmatrix} = \begin{bmatrix} \chi^{(1),ee}_{xx} & \chi^{(1),ee}_{xy} & \chi^{(1),ee}_{xz} \\ \chi^{(1),ee}_{yx} & \chi^{(1),ee}_{yy} & \chi^{(1),ee}_{yz} \\ \chi^{(1),ee}_{zx} & \chi^{(1),ee}_{zy} & \chi^{(1),ee}_{zz} \end{bmatrix} \begin{bmatrix} E_x \\ E_y \\ E_z \end{bmatrix} \tag{1.7}$$

This can also be written using a summation

$$P_i = \sum_j \chi^{(1),ee}_{ij} E_j \tag{1.8}$$

In what follows we will use the Einstein summation convention, which implies summation over all the indexed terms in a formula, lightening eq. (1.8) to

$$P_i = \chi^{(1),ee}_{ij} E_j \tag{1.9}$$

This simple approach to the interaction of light and matter suffices to explain most of the light effects we see every day, from the dispersion of light in a prism to the blue color of the sky. It does however fall short of explaining many other interesting optical effects.

1.1.2 Nonlinear optics

While many optical phenomena can be explained based on the linear optics described in section 1.1.1, for certain effects it is necessary to include higher-order terms. These are the result of the interaction of matter with more than one electric or magnetic field simultaneously. This can also be viewed as a series expansion of the induced polarization (eq. (1.8)) in the electric field of light[3]

$$P = \chi^{(1),ee}E(\omega) + \chi^{(2),eee} : E(\omega)E(\omega) + \chi^{(3),eeee} \vdots E(\omega)E(\omega)E(\omega) + \cdots \tag{1.10}$$

The induced polarization now contains components at multiple frequencies, resulting in the emission of light at multiple frequencies. Each nonlinear susceptibility can be related to certain optical effects and holds its own symmetry properties. In this thesis we will focus on the effects where the electric field is the incident electric field of light – however it is important to realize that similar expansions can be made for external electric fields. Expansions in function of static fields result in effects such as the Pockels or electro-optic effect,[4] while expansions with another light beam result in effects such as difference frequency generation.

The term containing $\chi^{(2),eee}$ describes second-order effects, because it requires the interaction of two electric fields. Two photons combine to form a new photon with a frequency equal to the sum of the frequencies of the original photons. The most relevant effect for this thesis is second harmonic generation (SHG), described by $\chi^{(2),eee}(-2\omega;\omega,\omega)$ which depends on symmetry breaking, making it intrinsically sensitive to chirality[5–8] and surfaces (section 1.3.1).[9–11]

The $\chi^{(3),eeee}$ terms are third-order effects as they require the interaction of three electric fields. For this thesis the most important is third harmonic generation (THG), $\chi^{(3),eeee}(-3\omega;\omega,\omega,\omega)$, which in practice is also sensitive to interfaces and is used in nonlinear optical microscopy.[12–14] Another important effect is degenerate four-wave mixing, $\chi^{(3),eeee}(-\omega;\omega,\omega,-\omega)$, which is useful to characterize third-order nonlinear optical materials or to achieve phase conjugation.[15, 16]

This expansion of the induced polarization in the electric field of light yields many effects which constitute research domains in their own right. Expanding the induced polarization in the electric field of light makes sense as the electric field of light suffices to explain many optical effects. It is also possible to expand the induced magnetization as a function of the incident electric field of light. While this is fundamentally interesting, these effects are typically very small and less important in the nonlinear optical response. Alternatively, we can expand the induced polarization (eq. (1.8)) as a series, taking into account the

magnetic induction B

$$\begin{aligned} P = {} & \chi^{(1),ee} E(\omega) + \chi^{(2),eem} : E(\omega)B(\omega) \\ & + \chi^{(2),eee} : E(\omega)E(\omega) + \chi^{(3),eeem} \vdots E(\omega)E(\omega)B(\omega) \\ & + \chi^{(3),eeee} \vdots E(\omega)E(\omega)E(\omega) + \chi^{(4),eeeem} \vdots\!\vdots E(\omega)E(\omega)E(\omega)B(\omega) \\ & + \cdots \end{aligned} \tag{1.11}$$

Initially it is not necessary to specify whether this is a static external magnetic induction $B(0)$ or the magnetic induction of light $B(\omega)$. The new terms that appear can be related to magneto-optical effects. When we consider a static magnetic induction $B(0)$, the imaginary part of the xyz component of $\chi^{(2),eem}(-\omega;\omega,0)$ becomes Faraday rotation. Again considering a static magnetic induction $B(0)$, $\chi^{(3),eeem}(-2\omega;\omega,\omega,0)$ relates to magnetization-induced second harmonic generation (MSHG); under the same circumstances, $\chi^{(4),eeeem}(-3\omega;\omega,\omega,\omega,0)$ relates to magnetization-induced third harmonic generation (MTHG). The terms in function of a magnetic induction other than that of the incident light are the terms we researched in this thesis, and we will now explore them theoretically.

1.2 Faraday rotation

1.2.1 Principles

Michael Faraday discovered Faraday rotation in 1845 while trying to investigate the effect of magnetic fields on light.[17] He observed that when linearly polarized light passes through a material and a magnetic field is applied in the direction of propagation of light, the polarization of the light rotates. This can be described by the formula

$$\theta = VBd \tag{1.12}$$

where d is the length that light travels through the material in the magnetic field, B is the magnetic induction in the direction of propagation of light and θ is the rotation of the polarization of the light. V, the Verdet constant, is a material parameter that determines how much a material rotates polarization in the presence of a magnetic induction. It is wavelength and temperature-dependent. For the visible wavelength region, we can derive the wavelength dependence

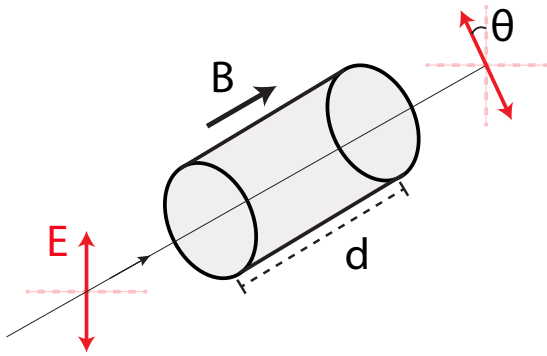

Figure 1.1: Faraday rotation is the rotation of linearly polarized light in a material where a magnetic field is present in the direction of propagation of light.

from the combination of the Becquerel formula[18]

$$V = \frac{e}{2mc}\lambda\frac{\mathrm{d}n}{\mathrm{d}\lambda} \tag{1.13}$$

and Cauchy's equation, which is only valid in the visible wavelength region in the absence of absorption[19]

$$n(\lambda) = A + \frac{B}{\lambda^2} + \frac{C}{\lambda^4} + \cdots \tag{1.14}$$

This yields a λ^{-2} dependence for the Verdet constant in the visible wavelength region in the absence of absorption. Faraday rotation is actually magnetically-induced circular birefringence, caused by Zeeman splitting of the relevant energy levels.[20, 21] This means that right-handed circularly polarized (RHCP) light and left-handed circularly polarized (LHCP) light "see" a different material. They no longer experience the same refractive index and one of the two will travel faster through the medium than the other. Because linearly polarized light can be described as the sum of RHCP and LHCP light, when both differ in speed, rotation of polarization ensues.

The empirical formula Faraday discovered (eq. (1.12)) does not appear similar to the formula we previously derived (eq. (1.11)), but it is straightforward to relate the two.[2] Faraday rotation derives from the polarization at frequency ω

$$P(\omega) = \chi^{(1),ee}(\omega)E(\omega) + \chi^{(2),eem}(-\omega;\omega,0)E(\omega)B(0) \tag{1.15}$$

Because rotation of linearly polarized light is caused by a difference in the refractive index for LHCP and RHCP light, we will solve this equation for

both. We define our axes such that light propagates along the z axis, with the magnetic field strength also along the z axis. In these coordinates, circularly polarized light is the sum of linearly polarized light along the x-axis and 90° phase shifted linearly polarized light along the y-axis. In complex notation this phase shift becomes a shift of i, and we obtain

$$E_{\mathrm{LHCP}}(\omega) = E_x - iE_y \tag{1.16}$$

$$E_{\mathrm{RHCP}}(\omega) = E_x + iE_y \tag{1.17}$$

$$E_{\pm}(\omega) = E_x \pm iE_y \tag{1.18}$$

Filling this into eq. (1.15) yields[2, 22]

$$P^{\pm}(\omega) = \chi^{(1),ee}(\omega)E_{\pm}(\omega) \pm i\chi^{(2),eem}(-\omega;\omega,0)E_{\pm}(\omega)B_z(0) \tag{1.19}$$

$$= \chi_{\pm}^{(1),effective}(\omega)E_{\pm}(\omega) \tag{1.20}$$

where i is the imaginary unit.

We can relate the effective susceptibility to the refractive index n_ω via[2]

$$n_\omega^2 = 1 + 4\pi\chi^{(1),effective}(\omega) \tag{1.21}$$

Combining eqs. (1.20) and (1.21) and omitting ω for clarity yields

$$n_{\pm}^2 = 1 + 4\pi(\chi^{(1),ee} \pm i\chi^{(2),eem}B_z) \tag{1.22}$$

$$= n_0^2 \pm 4\pi i\chi^{(2),eem}B_z \tag{1.23}$$

$$n_{\pm} = \sqrt{n_0^2 \pm 4\pi i\chi^{(2),eem}B_z} \tag{1.24}$$

where we have defined n_0 as the refractive index in the absence of magnetic induction. Because Faraday rotation only has a small effect on the refractive index, we can write the Taylor series of $n_\pm$ as a function of $\chi^{(2),eem}$ around 0

$$n_{\pm}(\chi^{(2),eem}) \approx n_{\pm}(0) + \frac{\mathrm{d}n_{\pm}}{\mathrm{d}\chi^{(2),eem}}(0) \times (\chi^{(2),eem} - 0) + \cdots \tag{1.25}$$

$$n_{\pm} \approx n_0 \pm \frac{2\pi i\chi^{(2),eem}B_z}{n_0} + \cdots \tag{1.26}$$

Since Faraday rotation is due to the difference in the refractive index for LHCP and RHCP, we can write[21]

$$\theta = \frac{\pi d}{\lambda}(n_- - n_+) \tag{1.27}$$

$$= \frac{\pi d}{\lambda}\left(\left[n_0 - \frac{2\pi i\chi^{(2),eem}B_z}{n_0}\right] - \left[n_0 + \frac{2\pi i\chi^{(2),eem}B_z}{n_0}\right]\right) \tag{1.28}$$

$$= -\frac{4\pi^2 i\chi^{(2),eem}B_z d}{\lambda n_0} \tag{1.29}$$

Combining this with the empirical Faraday eq. (1.12), we see that

$$V = \frac{4\pi^2 i\chi^{(2),eem}}{\lambda n_0} \tag{1.30}$$

This shows the relation between eqs. (1.11) and (1.12).

An important property of Faraday rotation is that it is non-reciprocal. The easiest way to understand this is to compare it to natural circular birefringence (NCB), the rotation of polarization of light when passing through a chiral material (fig. 1.2). NCB is reciprocal, while Faraday rotation is non-reciprocal.

When linearly polarized light passes through a chiral material, its polarization rotates due to NCB. When this light is reflected back through the sample, it travels in the opposite direction, but it "sees" the same material. The beam will rotate again, in the same direction when viewed in the coordinate system of the reflected light because it is "seeing" the same material. However, from an external viewpoint, this corresponds to rotating in the opposite direction, and so it rotates the beam back to the original state. The net result of reflecting light back through the same chiral material is zero rotation.
For Faraday rotation the situation is different. When a beam is reflected back through the sample, it "sees" a magnetic field in the opposite direction; the magnetic field breaks time-reversal symmetry. Because of the opposite magnetic field, the light will rotate in the opposite direction viewed in its own coordinate system. From an external viewpoint, this corresponds to further rotation. The net result of reflecting light back through a material is double the Faraday rotation. While fundamentally interesting, it also provides a handy way to increase Faraday rotation, both for measurement and applications.

1.2.2 Measurement

While Faraday rotation is present in all materials, magnetic or not, it is typically relatively small. For a 1 µm spin coated polymer sample, we can expect a

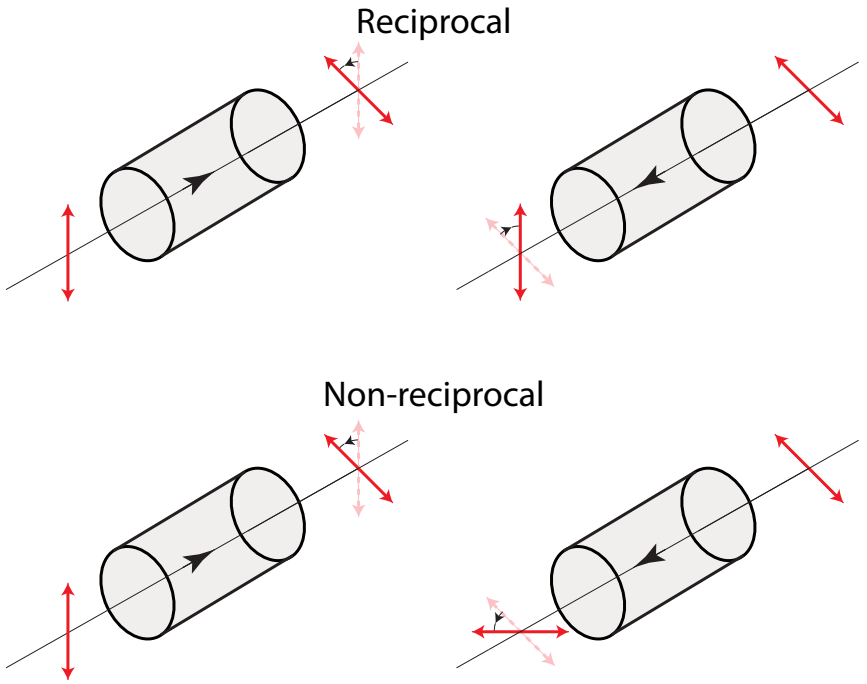

Figure 1.2: Reflection of light back through a sample results in zero rotation for a reciprocal effect such as chirality-induced optical rotation while it results in a doubling of rotation for a non-reciprocal effect such as Faraday rotation.

rotation of 500 µdeg using a desktop permanent magnet (1 T) and measuring in the visible wavelength region. This means specialized experimental setups are required to measure Faraday rotation. The most important caveat to keep in mind when designing and using such systems is the spatial extent of the magnetic field. The magnetic field strength that causes Faraday rotation in the sample can also cause undesired Faraday rotation in other optical components and can interfere with detection electronics such as lock-in amplifiers(LIAs) or photomultiplier tubes(PMTs).

Crossing polarizer and analyzer

The simplest approach to measuring Faraday rotation consists of a light source followed by a polarizer, the sample, and then an analyzer and a detector. In the absence of circular birefringence (CB) (natural or Faraday rotation), no light

will be detected when the polarizer and analyzer are at 90° (crossed) relative to each other. When CB is present in the sample, for instance Faraday rotation caused by the application of a magnetic field, the polarization of light rotates in the sample. The light is no longer at 90° relative to the analyzer once it has passed through the sample, which allows some of the light to pass through the analyzer and reach the detector. The measurement technique consists of rotating the analyzer until the detector again does not detect any light. Once the detector no longer detects any light, the analyzer is rotated as much as the CB in the sample, and simply reading the rotation of the analyzer yields the value of CB in the sample. While this is a very simple detection technique, it is not very sensitive. In order to improve the sensitivity it is necessary to introduce modulation to the measurement setup.

Using a photoelastic modulator

A photoelastic modulator (PEM) is an optical component that periodically alters the polarization of light.[23] PEMs make use of the photoelastic effect, which is stress-induced birefringence. Applying stress to a material can cause birefringence; choosing the correct material and amount of stress allows for precise control over the birefringence. Using piezoelectric crystals, a periodic voltage can be converted into a periodic stress on the PEM crystal. Thus the polarization is rapidly modulated from LHCP over linear polarization to RHCP. With the correct choice of analyzer and detection frequency, the resulting varying intensities of transmitted light can be related to the CB in the sample.[24]
In order to measure Faraday rotation, CB is measured for a set of discrete magnetic field strengths (H) applied over the sample. Fitting these results linearly to the resulting magnetic induction (B) according to eq. (1.12) yields the Verdet constant. This technique allows for a precise and rapid determination of Faraday rotation. With little extra effort, it can simultaneously provide information on circular dichroism (CD) and magnetic circular dichroism (MCD).[24] A full derivation of the mathematics behind the setup and certain extra precautions necessary when using PEMs are provided in chapter 2.

Using an alternating current magnetic field

Instead of modulating the polarization of the light, it is also possible to modulate the magnetic field. This is achieved through a setup similar to the crossed polarizer/analyzer setup, but with an alternating current (AC) magnetic field.[25] Detection at the frequency of the magnetic field yields the Faraday rotation. An improvement to this type of setup can be made by using a Wollaston prism (WP) instead of an analyzer. A WP separates a beam of light

into two diverging beams of orthogonal polarization. By detecting the difference in intensity for each of these beams, much of the background noise can be removed and Faraday rotation can be detected with far greater precision.[26, 27] Measurements are performed for a set of discrete applied magnetic field strengths (H), similar to the PEM setup. These results yield the Verdet constant by linear fitting to the resulting magnetic induction (B) (see eq. (1.12)). The advantage of using an AC magnetic field is that this setup is both more sensitive than the setup using a PEM, and that it has a much smaller detection limit. The disadvantage is that while AC magnetic fields cause AC Faraday rotation, they also cause electronic interference which is picked up by the lock-in amplifier. This type of interference, which is very difficult to avoid completely, can cause subtle effects on the measurements that can be difficult to isolate. As such, far more experimental care is necessary when performing measurements on this type of setup.

1.2.3 Calculation

Verdet constants and the associated Faraday rotation can be calculated using computational methods. The first step is to optimize the geometry of the molecule under investigation. The most common methods for geometry optimization are Møller–Plesset perturbation theory (frequently MP2) and DFT, typically using Pople basis sets such as 6-31+G** or Dunning basis sets such as aug-cc-pVDZ.[28] Using this optimized geometry, the Verdet constant can be calculated with a variety of methods.[29–33] In this dissertation we used quadratic response theory[34] as implemented in Dalton[35] for time-dependent density functional theory (TD-DFT) calculations. In TD-DFT, the energy is calculated from the electron density using functionals (functions of another function). Response theory measures how this electron density, and by extension the molecular properties, change due to perturbations. A Verdet constant can be seen as the variation of the electric dipole moment due to the perturbation of an external electric field and a static external magnetic field in the direction of the light.

1.2.4 Materials

Faraday rotation is linear as a function of the magnetic induction B present in the sample (eq. (1.12)). Typically, the magnetic induction is achieved by applying a magnetic field strength H. The relation between B and H depends on the type of material used, displayed in fig. 1.3 and elaborated in the next paragraphs, and is written in centimeter–gram–second system of units (CGS

units) as[36–38]

$$B = H + 4\pi M \tag{1.31}$$

$$M = \chi^{(1),mm} H \tag{1.32}$$

$$B = (H + 4\pi\chi^{(1),mm} H) = (1 + 4\pi\chi^{(1),mm})H = \mu H \tag{1.33}$$

where M is the magnetization, $\chi^{(1),mm}$ is the magnetic susceptibility and μ is the magnetic permeability of the material. Materials are classified according to the size and linearity of $\chi^{(1),mm}$.

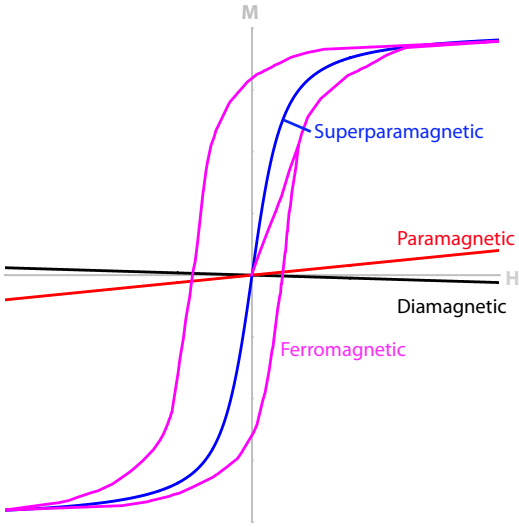

Figure 1.3: Each type of material responds differently to an applied magnetic field strength H, as can be seen in the resulting magnetization M. Dia- and paramagnetic materials display a small, linear magnetization as a function of the applied magnetic field strength. Ferro- and superparamagnetic materials display nonlinear magnetization behavior, with ferromagnetic materials showing remanent magnetization after removal of the external applied magnetic field strength.

Diamagnetic materials

Diamagnetic materials have a small, constant, negative $\chi^{(1),mm}(0)$. Consequently, applying a magnetic field strength induces a small magnetization in the material counter to the applied magnetic field strength. The result is a magnetic induction B which is slightly smaller than the magnetic field strength H; however the difference is typically negligible. It follows that for diamagnetic materials, in most cases, $B \approx H$ (or $\mu \approx 1$) is a valid approximation, meaning there is no need to take the difference into account when analyzing Faraday rotation. Most common organic materials and solvents, such as toluene and methanol, are diamagnetic.

Paramagnetic materials

Paramagnetic materials have a larger, constant, positive $\chi^{(1),mm}(0)$. Applying a magnetic field strength induces a larger magnetization in the same direction as the applied magnetic field strength. The magnetic induction is thus slightly larger than the magnetic field strength, however it is again sufficiently small to allow the approximation $B \approx H$ (or $\mu \approx 1$) when analyzing most Faraday rotation measurements. Many minerals that contain iron are paramagnetic at room temperature,[39] and many metal complexes are also paramagnetic.[40]

Ferromagnetic materials

Besides dia- and paramagnetic materials, there are many other types of magnetic materials. The ones of relevance for this dissertation are the ferromagnetic and the superparamagnetic materials. Ferromagnetic materials typically show a very large $\chi^{(1),mm}(0)$, but it is not linear as a function of the applied magnetic field strength and saturates at high magnetic fields. They also differ from dia- and paramagnetic materials in that they show a magnetic memory due to their hysteresis. Their magnetization thus depends not only on the currently applied magnetic field strength, but also their history. While this is crucial for certain applications such as magnetic memory,[41] it complicates their analysis and is detrimental for other applications.

Superparamagnetic materials

Superparamagnetic materials are a special class of paramagnetic materials. It is easiest to picture them as materials consisting of non-interacting units with one giant spin or magnetization. The lowest energy for this giant spin is

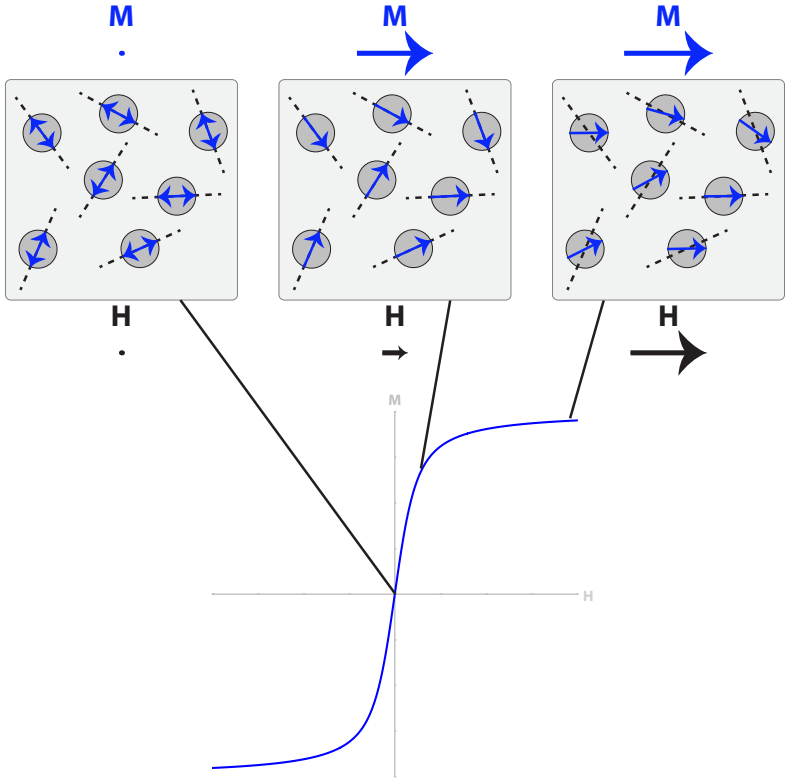

Figure 1.4: In the absence of an external magnetic field strength, the individual units in a superparamagnetic material flip randomly between the orientations along their easy axis (dashed black line) and there is no net magnetization. Application of a small external magnetic field strength flips the individual magnetizations in the direction closest to the applied magnetic field strength, causing a rapid increase in magnetization at low magnetic field strengths. Larger magnetic field strengths slowly pull the individual magnetizations away from their easy axis and parallel to the applied magnetic field strength, increasing the magnetization of the material at a much slower pace. This process explains the shape of the magnetization curve of a superparamagnetic material.

parallel to a specific axis (the easy axis), but the direction along this axis is inconsequential.[42–44] In the absence of an external magnetic field strength, the individual units flip between both orientations along their easy axis due to thermal fluctuations and there is no net magnetization. When an external magnetic field strength is applied, the individual units stay along their easy axis but flip in the direction closest to the applied magnetic field strength. This sudden flipping causes a rapid increase in magnetization at low magnetic field strengths. Further increases in the magnetic field strength no longer flip the individual spins, but slowly pull them away from their easy axis and parallel to the applied magnetic field strength. This process further increases the magnetization of the material, but at a much slower pace, resulting in a saturation of magnetization at higher magnetic fields. This process, depicted in fig. 1.4, explains the shape of the magnetization curve of a superparamagnetic material, which is described by a Langevin equation.
As with the ferromagnetic materials, there is no longer a simple linear relation between B and H; however there is no dependence on the magnetization history, rendering measurements with these materials easier to analyze than those with ferromagnetic materials. A typical example of such a material is a superparamagnetic iron oxide nanoparticle.[45–47] These nanoparticles are so small they can only support one magnetic domain. As such they behave as a single magnetization or a giant spin. The magneto-optical behavior of certain superparamagnetic systems has been studied spectrally both theoretically and experimentally, coupling their magneto-optical spectra to magnetically active transitions in the material.[48–51]

1.2.5 Applications

Since Faraday rotation has many applications, research into Faraday rotating materials has both fundamental and industrial significance.

One of the oldest applications, made famous by Stephen Hawking's quote "... I wasn't going to do something boring like Faraday rotation",[52] is in cosmology. Certain light sources in space, such as pulsars and quasars, are known to be polarized. Because vacuum does not display Faraday rotation, any observed polarization in the interstellar medium rotation must be attributed to free electrons. Thus the rotation of polarization of the light observed from pulsars and quasars can be used to derive information on the distribution and size of magnetic fields in space and the free electron density distribution.[53]

Instead of measuring Faraday rotation to determine magnetic and magneto-optical properties of materials, it can also be used with materials of a known Verdet constant in order to determine magnetic fields. Faraday rotation-based

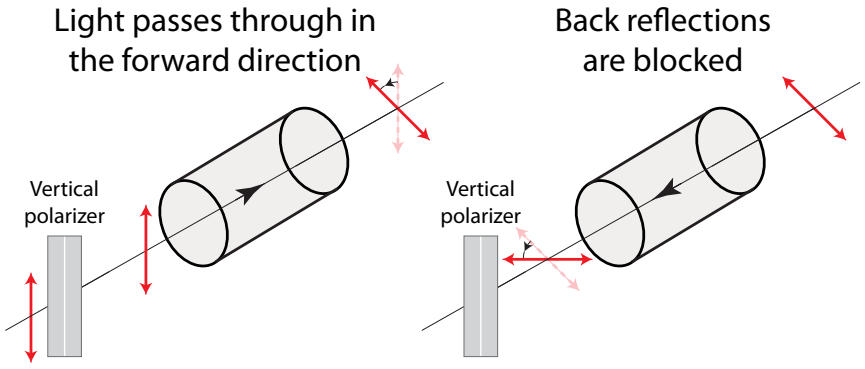

Figure 1.5: An optical isolator uses the non-reciprocity of Faraday rotation to allow light to pass in the forward direction, but to block unwanted back reflections.

magnetometers can detect both the direction and size of sub-nT magnetic fields[54] and can be made quite compact. Constant improvements in materials, sensor size and sensitivity are making these sensors small and sensitive enough to perform magnetoencephalography.[55] Typically, in order to achieve high sensitivity, the Faraday rotation of specific transitions of atomic vapors are used, quite often those in rubidium.

A final application – perhaps the best known in the optics community – is the use of Faraday rotation to make optical isolators (fig. 1.5).[56–59] In most optical setups that use a laser, back-reflections of other optical components into the laser are highly undesirable.[60] Because of the non-reciprocity of Faraday rotation, it is an excellent method to distinguish between desired forward light beams and unwanted back-reflections. Using a simple combination of polarizer, 45° Faraday rotating material and analyzer at 45°, the distinction can be made for linearly polarized light. Slightly more complicated designs exist to perform the same distinction on unpolarized light. For most Faraday isolators currently commercially available, substituted iron garnets are used.[61] They display Verdet constants on the order of $10 \times 10^6\,^\circ\,\mathrm{T}^{-1}\,\mathrm{m}^{-1}$ at 1550 nm, a laser wavelength frequently used in telecommunications.

1.2.6 State of the art

At telecommunication wavelengths, rare-earth iron garnets are typically used as Faraday rotating materials. Despite the fact that their properties were

discovered many decades ago,[62] they remain the most performant materials around 1550 nm, achieving Verdet constants up to $10^8 \circ \mathrm{T}^{-1}\,\mathrm{m}^{-1}$. In the visible wavelength region, rare-earths are used to achieve high Verdet constants in inorganic materials. Doping glasses with rare-earths, magnetic nanoparticles or rare-earth doped nanoparticles results in relatively transparent materials with Verdet constants up to $10^7 \circ \mathrm{T}^{-1}\,\mathrm{m}^{-1}$ around 500 nm with absorption coefficients around $1\,\mathrm{cm}^{-1}$.[63–65]

Organic materials, on the other hand, show much smaller Faraday rotation. Their Verdet constants are typically smaller than $10^3 \circ \mathrm{T}^{-1}\,\mathrm{m}^{-1}$ at 400 nm,[66, 67] with two notable exceptions. Polythiophenes have been shown to have Verdet constants exceeding $10^4 \circ \mathrm{T}^{-1}\,\mathrm{m}^{-1}$ at 400 nm, but these results are controversial and have reproducibility issues.[68] Graphene, on the other hand, displays enormous Faraday rotation, with a Verdet constant close to $10^9 \circ \mathrm{T}^{-1}\,\mathrm{m}^{-1}$.[69, 70] The important caveat to these measurements is that the Verdet constant is a measure of rotation per unit of length, and the extremely minute thickness of a sheet of graphene causes this constant to be large. The rotation of graphene does not, however, scale with thickness, as graphite does not show the same magneto-optical activity as graphene. This limits the applicability of graphene in devices.

1.3 Magnetization-induced second harmonic generation

In order to understand MSHG, comprehending SHG is a prerequisite. We will first briefly describe the principles of SHG, followed by a concise explanation of its measurement, the materials used and finally some applications. With this knowledge in place, we will proceed to explain MSHG.

1.3.1 Second harmonic generation

Principles

The relevant term of eq. (1.10) for SHG is

$$P(2\omega) = \chi^{(2),eee}(-2\omega;\omega,\omega) : E(\omega)E(\omega) \tag{1.34}$$

This equation shows that a polarization is induced at 2ω, causing light to be emitted at this frequency. Two photons at frequency ω have combined to become

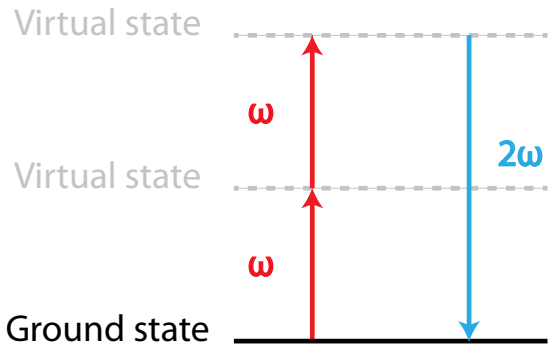

Figure 1.6: In second harmonic generation, two photons at frequency ω combine and are emitted as one photon at frequency 2ω.

one photon at frequency 2ω, the second harmonic (fig. 1.6) – hence the name of this effect.

The most important characteristics of SHG can be attributed to the second-order polarizability $\chi^{(2),eee}(-2\omega;\omega,\omega)$, a rank 3 tensor consisting of 27 elements. When SHG is generated from a single fundamental beam, 18 of these elements, at most, are independent. The number of independent, non-zero elements is typically much smaller, and depends on the symmetry of the material being studied. The most important symmetry property is that for centrosymmetric materials $\chi^{(2),eee}(-2\omega;\omega,\omega) = 0$ and SHG is forbidden.[71] For other symmetries, we can write this in compact notation. In this notation, when we write abc, the a indicates the direction of the emitted electric field and b and c indicate the direction of the incident electric field

$$\chi^{(2),eee}(-2\omega;\omega,\omega) = \begin{bmatrix} xxx & xyy & xzz & xyz & xxz & xxy \\ yxx & yyy & yzz & yyz & yxz & yxy \\ zxx & zyy & zzz & zyz & zxz & zxy \end{bmatrix} \tag{1.35}$$

The reason we can use this compact notation for SHG from a single laser beam with frequency ω is that the physical process cannot distinguish between a "first" and a "second" photon. Consequently the last two indices can be switched: $\chi^{(2),eee}_{xyz}(-2\omega;\omega,\omega) = \chi^{(2),eee}_{xzy}(-2\omega;\omega,\omega)$. The presence of a single 180° rotation axis along the z-axis (a C_2 axis) gives a sample the following second-order susceptibility

$$\chi^{(2),eee}(-2\omega;\omega,\omega) = \begin{bmatrix} 0 & 0 & 0 & xyz & xxz & xxy \\ 0 & 0 & 0 & yyz & yxz & 0 \\ zxx & zyy & zzz & 0 & 0 & zxy \end{bmatrix} \tag{1.36}$$

The second-order susceptibility for SHG reduces from 18 to 9 non-zero independent elements. A C_4 axis yields

$$\chi^{(2),eee}(-2\omega;\omega,\omega) = \begin{bmatrix} 0 & 0 & 0 & xyz & xxz & 0 \\ 0 & 0 & 0 & xxz & -xyz & 0 \\ zxx & zxx & zzz & 0 & 0 & 0 \end{bmatrix} \tag{1.37}$$

The four-fold rotation axis has reduced the number of non-zero independent components to 4. Adding an xz mirror plane, which also implies a yz mirror plane because of the C_4 symmetry, yields a C_{4v} symmetry and reduces the second-order susceptibility to

$$\chi^{(2),eee}(-2\omega;\omega,\omega) = \begin{bmatrix} 0 & 0 & 0 & 0 & xxz & 0 \\ 0 & 0 & 0 & xxz & 0 & 0 \\ zxx & zxx & zzz & 0 & 0 & 0 \end{bmatrix} \tag{1.38}$$

There are now only 3 remaining non-zero independent elements. The key difference between the C_4 and C_{4v} symmetry is the $\chi^{(2),eee}_{xyz}(-2\omega;\omega,\omega) = -\chi^{(2),eee}_{yxz}(-2\omega;\omega,\omega)$ component. This component is inherent to chiral systems; for achiral systems it is by definition zero. A correct choice of input and output polarization makes it possible to probe only this component, which explains the high sensitivity of SHG to chirality.

Adding more symmetry elements, such as rotation axes and mirror planes, reduces the number of independent, non-zero components in the second-order susceptibility. This high sensitivity of the second-order susceptibility, and by extension of SHG, to symmetry and symmetry-breaking makes SHG an excellent tool to study chirality[7, 8, 72, 73] as well as interfaces.[10, 74, 75]

Measurement

SHG is typically a weak effect, but it depends quadratically on the incident electric field (eq. (1.34)). It follows that a doubling of the incident light power results in a quadrupling of the SHG, illustrating the benefits of using intense, pulsed lasers as light sources. SHG measurement systems are thus designed around high-power incident light intensities. Efficient SHG can be obtained by phase matching or poling of materials; however this is beyond the scope of this dissertation. The advantage to measuring SHG is that the generated light is at half the wavelength (or double the frequency) of the incident light, which enables relatively easy filtering of the incident fundamental light. Despite this, SHG is typically so weak that a PMT is necessary in order to detect it.[10, 76] Because of the quadratic dependence on the incident field, the peak power is most important, and the laser beam is typically pulsed and strongly focused.

Materials

Initial SHG research focused on inorganic materials.[77] Seeing as SHG requires non-isotropic materials, the materials had to be to either intrinsically anisotropic or chiral; alternatively, anisotropy had to be introduced, for example by poling. Typical crystals employed to generate large amounts of SHG were quartz[78] and periodically poled $LiNbO_3$.[79] Due to improved processability and flexibility in synthesis, later research focused on organic molecules poled in a polymer matrix; Disperse Red 1 was a very common chromophore.[80, 81] Subsequent research examined SHG from polymers themselves, to avoid the disadvantages of using a poled chromophore/matrix combination.[82–86] The most recent research includes surface roughness,[9] surface interactions and assemblies,[10, 74] nanomaterials,[87, 88] biological materials[89, 90] and plasmonic materials.[91]

Applications

Nonlinear optical effects have a wide range of applications. The most industrially important applications are found in telecommunications[92] and laser light generation.[15, 93] While SHG does not have a direct application in telecommunications, it is very closely related to the electro-optic effect, which is the key principle in an electro-optic modulator. As such, SHG can be used to characterize and optimize materials for application in electro-optic modulators.

While limited in an industrial context, SHG has many applications in research and development. Its high sensitivity to symmetry and symmetry-breaking make it an excellent tool for characterizing surfaces and even buried interfaces, down to single atom resolution.[9, 10, 74, 75, 94] The sensitivity to symmetry can also be used to derive information on the (centro)symmetry and chirality of samples.[5, 95–98] SHG can also be detected using a microscope, providing spatial distribution information as well as symmetry and orientation information; in a biological context this is often even possible without the use of labels. SHG microscopy enables measurements of a wide array of effects, ranging from electric potential over membranes to space charge accumulation in organic bulk heterojunctions and the visualization of osteogenesis in bone.[87, 89, 90, 99, 100]

1.3.2 Magnetization-induced second harmonic generation

Principles

With an understanding of SHG we can now review the relevant terms of eq. (1.11) in order to understand MSHG

$$P(2\omega) = \chi^{(2),eee}(-2\omega;\omega,\omega)E(\omega)E(\omega) + \chi^{(3),eeem}(-2\omega;\omega,\omega,0)E(\omega)E(\omega)B(0) \tag{1.39}$$

Taking into account the magnetic induction present in the sample adds a new term to the polarization at 2ω. This is described by $\chi^{(3),eeem}(-2\omega;\omega,\omega,0)$, a rank 4 tensor consisting of 81 symmetry-dependent elements. The magnetic induction $B(0)$ can be the result of an externally applied magnetic field strength $H(0)$,[76, 101, 102] but can also be due to a magnetization present inside the material.[103] We see that the polarization at 2ω, normally associated with SHG, is now also influenced by a magnetic field: the number and polarization of the photons we detect at half the wavelength of the incident light will vary depending on the magnetic induction.

Measurement

MSHG can be measured the same way as SHG. The SHG setup is modified in order to be able to accommodate a direct current (DC) magnet. Subsequently, SHG is measured for a discrete set of magnetic fields and the results are processed in order to be able to distinguish the SHG from the MSHG. When adding a magnet to an optical setup, caution is required, just as in Faraday rotation setups. In the case of MSHG, the effect of the magnetic field on the PMT requires extra attention, as the measurements are typically very sensitive with high-voltage PMTs and low signal levels.

Materials

In the field of nonlinear optics, MSHG is still a relatively new research domain. Its greatest advantage is the capability of probing surfaces and interfaces, even if these are buried. The materials most investigated by MSHG are magnetic surfaces such as Fe-surfaces[104] and multilayers containing magnetic components.[105]

Applications

MSHG is used to characterize and analyze magnetic systems.[106] Recent pushes to the nanoscale have allowed MSHG to show its strength as a characterization tool. Single molecule magnets hold great promise in magnetic information storage, quantum computing and magnetic refrigeration, and MSHG is used extensively to characterize their properties, aiding in design and progress in the field.[107, 108] Magnetic metamaterials hold potential as materials for such applications as electromagnetic cloaks;[109] these materials can also be extensively characterized by MSHG, which can reveal the effect of a magnetic field on the interaction of light with these metamaterials.[101, 102] Finally, MSHG is also used to observe the behavior of specific magnetic phenomena such as superparamagnetism,[76] magnetization reversal[103] and the effects of additional layers on interface magnetism.[110]

1.4 Research goals

In section 1.1.2 equations were introduced to formulate the influence of magnetic fields on light–matter interaction. Some of the resulting terms are interactions that have been known for over a century, such as Faraday rotation. Others, such as MSHG, have only been researched for twenty years, yet they have already provided a plethora of information on magnetic materials. Despite the lengthy research performed on various magneto-optical effects and their importance in everyday applications such as optical networks, many avenues of research remain unexplored. The goal of this dissertation is to further the understanding of the interaction of light and matter in the presence of a magnetic field.

Organic materials show many advantages over inorganic materials in terms of applications, such as their high processability and the great flexibility in synthesis. These benefits caused a shift in research from inorganic to organic materials in SHG. This shift has not (yet) taken place in Faraday rotation research; consequently in a first research goal, we investigated the possibilities of using organic materials as Faraday rotating materials (chapters 3 and 4). Analyzing the measurement setup (chapter 2) is a critical first step which allows for correct interpretation of our Faraday rotation measurements.

Since magneto-optical effects were first discovered, new types of materials with exotic forms of magnetism have been discovered.[111] Many of these new forms of magnetism have been characterized by techniques using devices such as a vibrating sample magnetometer (VSM) or a superconducting quantum interference device (SQUID). However, much research remains to be done

on their magneto-optic characteristics. In this dissertation we also focus on superparamagnetism (see also section 1.2.4); this sort of magnetism is easily accessible through superparamagnetic iron oxide nanoparticles, but its magneto-optical implications are still poorly explored (chapters 5 and 6).

Chapter 2

Photoelastic modulator non-idealities in magneto-optical polarization measurements

In order to characterize Faraday rotation in organic materials, a specialized experimental setup must be used. This was already briefly discussed in section 1.2.2, but it is necessary to analyze the experimental setup in detail. This chapter is a proceedings from SPIE Optics + Photonics 2013 adapted to form for this dissertation.

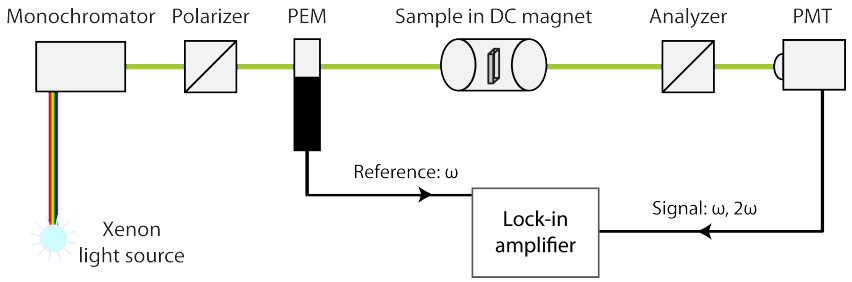

Photoelastic modulator non-idealities in magneto-optical polarization measurements
In Shaw, J. A. (Ed.), LeMaster, D. A. (Ed.), Polarization Science and Remote Sensing VI: Vol. 8873. Optics and Photonics, San Diego, USA, Aug 25, 2013 (pp. 88730Z1–88730Z11)
S. Vandendriessche and T. Verbiest

2.1 Abstract

Modifying and detecting the polarization of light is increasingly important in many contexts such as Faraday isolators and electro-optic modulators. In order to control the polarization of light, it is necessary to know the polarization characteristics of the materials used in the applications. To be able to (magneto-)optically characterize novel materials, we designed a setup using a photoelastic modulator (PEM) to simultaneously detect natural and magnetic circular dichroism and circular birefringence over a large spectral range. We then theoretically analyzed and experimentally characterized the effect of non-idealities in the PEM on the setup and the resulting data. Our results demonstrate an influence of PEM non-idealities on the measured signals, resulting in non-negligible mixing of circular birefringence and circular dichroism signals. Our measurements of the wavelength dependence of these non-idealities reveal larger non-idealities towards shorter wavelengths. These results illustrate the necessity to take PEM non-idealities into account when working with PEMs, especially at shorter wavelengths or when dealing with signals spanning different orders of magnitude. PEM non-idealities, while frequently neglected in experimental setup design and theoretical derivations, are expected to be more complicated and possibly exert a larger influence on obtained results for experimental setups with multiple PEMs.

2.2 Introduction

Polarization is an important fundamental property of electromagnetic waves.[112] Detecting and manipulating the polarization of light is essential for both fundamental research as well as for applications.[9, 74, 113–118] A variety of optical elements exist to manipulate the polarization of UV to infrared light.[119–121] It can be useful to be able to modulate this polarization, and photoelastic modulators modulate the polarization of light at high frequencies, based on the stress-dependence of birefringence in certain materials.[122] Photoelastic modulators have been used for well over 40 years,[23] finding applications in a wide variety of fields such as protein adsorption,[123] high-speed semiconductor growth monitoring,[124] liquid crystal characterization,[125] biosensing,[126] semiconductor analysis,[127, 128] following catalysis[129] and magneto-optical characterization of (nano)materials.[130–132]

When a magnetic field is applied in the direction of propagation of light, the complex refractive indices for left- and right-circularly polarized light are no longer equal.[67, 133–135] The difference in the real part of the refractive indices results in Faraday rotation. Faraday rotation can be observed as the rotation of

the polarization of linearly polarized light in a magnetic field along the direction of propagation of light. It is described by

$$\theta = VBd \tag{2.1}$$

where θ is the rotation of the polarization of light, V is the Verdet constant, a wavelength-dependent material parameter, B is the magnetic field in the direction of light and d is the distance light travels through the material in the magnetic field.[17] The difference in the imaginary part of the refractive indices for left- and right-circularly polarized light manifests itself as magnetic circular dichroism (MCD)[136–138]

$$\Delta A = \frac{A_{LCP} - A_{RCP}}{A_{LCP} + A_{RCP}} \tag{2.2}$$

where ΔA is the MCD signal and A_{LCP} and A_{RCP} are respectively the absorption of left- and right-hand circularly polarized light.

We designed a setup using a single photoelastic modulator (PEM) to simultaneously detect circular dichroism, both natural and magnetic, circular birefringence and Faraday rotation over a large spectral range. These optical effects have many uses in fundamental research[66] and applications,[139] both for chiral[140, 141] and achiral[45, 46, 49, 142] systems. For the analysis of simple optical systems it is not always necessary to even take into account the polarization of light.[143–145] However, polarization dependent samples and experimental setups such as ours require more complex analysis,[126, 131, 146, 147] and this is done using Stokes vectors and Mueller matrices.[148–151] Light, both polarized and depolarized, can be described by a Stokes vector

$$\vec{S} = \begin{bmatrix} S_0 \\ S_1 \\ S_2 \\ S_3 \end{bmatrix} \tag{2.3}$$

A detailed analysis of the Stokes parameters can be found elsewhere.[152] For our analysis, it is important that $S_0 = I$ where I is the intensity of the light beam. When light passes through an optical element with Mueller matrix M_a and then an optical element with Mueller matrix M_b, the outgoing light can be described as

$$\vec{S}_{out} = M_b M_a \vec{S}_{in} \tag{2.4}$$

Using Mueller calculus, we theoretically analyze and experimentally characterize the effect of PEM non-idealities on the data measured in our setup. We

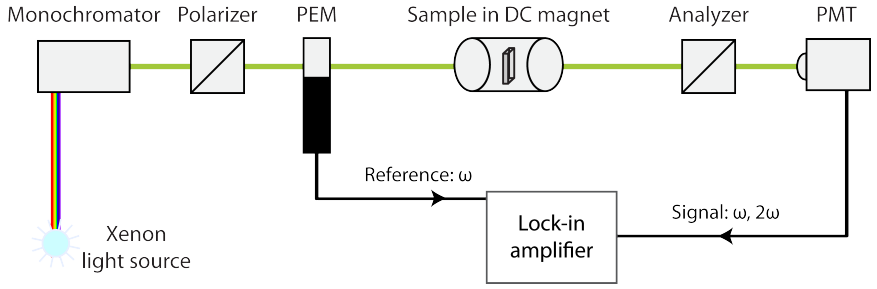

Figure 2.1: In the experimental setup, a single PEM is used to detect (magnetic) circular dichroism and birefringence.

demonstrate an influence of PEM non-idealities on the measured signals, resulting in non-negligible mixing of circular birefringence and circular dichroism signals. These results illustrate the necessity to take PEM non-idealities into account when working with PEMs, especially at shorter wavelengths or when dealing with signals spanning different orders of magnitude. Moreover, these results can be expanded to other experimental setups such as dedicated CD-spectrometers.

2.3 Experimental details

In the experimental setup (fig. 2.1), a laser driven light source (Energetiq LDLS EQ-99) is focused into a collimated beam. A polarizer polarizes the beam after it passes through a monochromator. The polarized beam passes through a photoelastic modulator (Hinds I/FS50) operating at 50 kHz, placed with its main axis 45 degrees relative to the polarization of the light. The beam then passes through a sample in a DC magnet, and after passing through an analyzer at 45 degrees with respect to the first polarizer it is detected by a photomultiplier tube. Two lock-in amplifiers (SR830) detect the resulting signal, one detecting at the fundamental frequency of the PEM (50 kHz), the other detecting the second harmonic (100 kHz). At discrete magnetic fields the signal value of each lock-in amplifier is read out by a personal computer. In the subsequent section, the relation between the 50 kHz and 100 kHz signal and the (magnetic) circular dichroism and the optical rotation and Faraday rotation is derived.

2.4 Theoretical and experimental results

2.4.1 General theoretical derivation

To be able to describe the setup, knowledge is necessary of the Mueller matrices of the components. For the first polarizer, at 45 degrees, the Mueller matrix is

$$M_{45degpolarizer} = \frac{1}{2}\begin{bmatrix} 1 & 0 & \pm 1 & 0 \\ 0 & 0 & 0 & 0 \\ \pm 1 & 0 & 1 & 0 \\ 0 & 0 & 0 & 0 \end{bmatrix} \tag{2.5}$$

The Mueller matrix for the PEM is

$$M_{PEM} = \begin{bmatrix} 1 & 0 & 0 & 0 \\ 0 & 1 & 0 & 0 \\ 0 & 0 & \cos(\delta) & \sin(\delta) \\ 0 & 0 & -\sin(\delta) & \cos(\delta) \end{bmatrix} \tag{2.6}$$

where δ is the dynamic retardation. The Mueller matrix for a general sample is

$$M_{sample} = \begin{bmatrix} m_{00} & m_{01} & m_{02} & m_{03} \\ m_{10} & m_{11} & m_{12} & m_{13} \\ m_{20} & m_{21} & m_{22} & m_{23} \\ m_{30} & m_{31} & m_{32} & m_{33} \end{bmatrix} \tag{2.7}$$

Finally, the Mueller matrix of the horizontal analyzer is

$$M_{horizontalpolarizer} = \frac{1}{2}\begin{bmatrix} 1 & 1 & 0 & 0 \\ 1 & 1 & 0 & 0 \\ 0 & 0 & 0 & 0 \\ 0 & 0 & 0 & 0 \end{bmatrix} \tag{2.8}$$

For the experimental setup, we can write:

$$\vec{S}_{out} = M_{analyzer} * M_{sample} * M_{PEM} * M_{polarizer} * \vec{S}_{in}$$

$$= \frac{1}{2}\begin{bmatrix} 1 & 1 & 0 & 0 \\ 1 & 1 & 0 & 0 \\ 0 & 0 & 0 & 0 \\ 0 & 0 & 0 & 0 \end{bmatrix} \begin{bmatrix} m_{00} & m_{01} & m_{02} & m_{03} \\ m_{10} & m_{11} & m_{12} & m_{13} \\ m_{20} & m_{21} & m_{22} & m_{23} \\ m_{30} & m_{31} & m_{32} & m_{33} \end{bmatrix} \tag{2.9}$$

$$* \begin{bmatrix} 1 & 0 & 0 & 0 \\ 0 & 1 & 0 & 0 \\ 0 & 0 & \cos(\delta) & \sin(\delta) \\ 0 & 0 & -\sin(\delta) & \cos(\delta) \end{bmatrix} \frac{1}{2} \begin{bmatrix} 1 & 0 & 1 & 0 \\ 0 & 0 & 0 & 0 \\ 1 & 0 & 1 & 0 \\ 0 & 0 & 0 & 0 \end{bmatrix} \vec{S}_{in}$$

$$= \frac{1}{4}\begin{bmatrix} m_{00}+m_{10} & m_{01}+m_{11} & m_{02}+m_{12} & m_{03}+m_{13} \\ m_{00}+m_{10} & m_{01}+m_{11} & m_{02}+m_{12} & m_{03}+m_{13} \\ 0 & 0 & 0 & 0 \\ 0 & 0 & 0 & 0 \end{bmatrix} \tag{2.10}$$

$$* \begin{bmatrix} 1 & 0 & 0 & 0 \\ 0 & 1 & 0 & 0 \\ 0 & 0 & \cos(\delta) & \sin(\delta) \\ 0 & 0 & -\sin(\delta) & \cos(\delta) \end{bmatrix} \begin{bmatrix} 1 & 0 & 1 & 0 \\ 0 & 0 & 0 & 0 \\ 1 & 0 & 1 & 0 \\ 0 & 0 & 0 & 0 \end{bmatrix} \vec{S}_{in}$$

$$= \frac{1}{4}\begin{bmatrix} m_{00}+m_{10} & m_{01}+m_{11} & m_{02}+m_{12} & m_{03}+m_{13} \\ m_{00}+m_{10} & m_{01}+m_{11} & m_{02}+m_{12} & m_{03}+m_{13} \\ 0 & 0 & 0 & 0 \\ 0 & 0 & 0 & 0 \end{bmatrix} \tag{2.11}$$

$$* \begin{bmatrix} 1 & 0 & 1 & 0 \\ 0 & 0 & 0 & 0 \\ \cos(\delta) & 0 & \cos(\delta) & 0 \\ -\sin(\delta) & 0 & -\sin(\delta) & 0 \end{bmatrix} \vec{S}_{in}$$

$$= \frac{1}{4}\begin{bmatrix} a+b\cos(\delta)-c\sin(\delta) & 0 & a+b\cos(\delta)-c\sin(\delta) & 0 \\ a+b\cos(\delta)-c\sin(\delta) & 0 & a+b\cos(\delta)-c\sin(\delta) & 0 \\ 0 & 0 & 0 & 0 \\ 0 & 0 & 0 & 0 \end{bmatrix} \vec{S}_{in} \tag{2.12}$$

Where we define

$$a = m_{00} + m_{10} \tag{2.13}$$

$$b = m_{02} + m_{12} \tag{2.14}$$

$$c = m_{03} + m_{13} \tag{2.15}$$

in order to lighten the notation. Because the initial light is unpolarized,

$$\vec{S}_{in} = \begin{bmatrix} I_0 \\ 0 \\ 0 \\ 0 \end{bmatrix} \tag{2.16}$$

This means that

$$\vec{S}_{out} = \frac{1}{4} \begin{bmatrix} a + b\cos(\delta) - c\sin(\delta) & 0 & a + b\cos(\delta) - c\sin(\delta) & 0 \\ a + b\cos(\delta) - c\sin(\delta) & 0 & a + b\cos(\delta) - c\sin(\delta) & 0 \\ 0 & 0 & 0 & 0 \\ 0 & 0 & 0 & 0 \end{bmatrix} \begin{bmatrix} I_0 \\ 0 \\ 0 \\ 0 \end{bmatrix} \tag{2.17}$$

$$= \frac{I_0}{4} \begin{bmatrix} a + b\cos(\delta) - c\sin(\delta) \\ a + b\cos(\delta) - c\sin(\delta) \\ 0 \\ 0 \end{bmatrix} \tag{2.18}$$

This means the outgoing light has an intensity detected by the photomultiplier tube

$$I_{out} = \frac{I_0}{4}(a + b\cos(\delta) - c\sin(\delta)) \tag{2.19}$$

In order to be able to understand this result, we need to fill in the dynamic retardation of a PEM, which can be written as[153]

$$\delta(\lambda) = A(\lambda)sin(\omega t) + \delta_0(\lambda) \tag{2.20}$$

With $\delta(\lambda)$ the dynamic retardation, $A(\lambda)$ the amplitude of oscillation, ω the vibration frequency and $\delta_0(\lambda)$ the static strain present in the PEM. For an ideal PEM, $\delta_0 = 0$ as there is no static strain. It is however precisely the important

non-ideality that $\delta_0 \neq 0$ that we will focus on later on in the derivation. Applying the trigonometrical sum of angle formulas

$$\cos(x+y) = \cos(x)\cos(y) - \sin(x)\sin(y) \tag{2.21}$$

$$\sin(x+y) = \sin(x)\cos(y) + \cos(x)\sin(y) \tag{2.22}$$

yields

$$\cos(\delta) = \cos(A(\lambda)sin(\omega t))\cos(\delta_0(\lambda)) - \sin(A(\lambda)sin(\omega t))\sin(\delta_0(\lambda)) \tag{2.23}$$

$$\sin(\delta) = \sin(A(\lambda)sin(\omega t))\cos(\delta_0(\lambda)) + \cos(A(\lambda)sin(\omega t))\sin(\delta_0(\lambda)) \tag{2.24}$$

Filling this into eq. (2.19) yields

$$\begin{aligned} I = \frac{I_0}{4}(a + b[&\cos(A(\lambda)sin(\omega t))\cos(\delta_0(\lambda)) - \sin(A(\lambda)sin(\omega t))\sin(\delta_0(\lambda))] \\ &- c[\sin(A(\lambda)sin(\omega t))\cos(\delta_0(\lambda)) + \cos(A(\lambda)sin(\omega t))\sin(\delta_0(\lambda))]) \end{aligned} \tag{2.25}$$

This expression can be regrouped to

$$\begin{aligned} I = \frac{I_0}{4}(a &- [b\sin(\delta_0(\lambda)) + c\cos(\delta_0(\lambda))]\sin(A(\lambda)sin(\omega t)) \\ &+ [b\cos(\delta_0(\lambda)) - c\sin(\delta_0(\lambda))]\cos(A(\lambda)sin(\omega t))) \end{aligned} \tag{2.26}$$

In order to understand the signal detected at ω and 2ω from eq. (2.26), $\cos(A(\lambda)\sin(\omega t))$ and $\sin(A(\lambda)\sin(\omega t))$ need to be expanded using Bessel functions

$$\cos(A\sin(\omega t)) = J_0(A) + 2\sum_{j=1} J_{2j}(A)\sin(2j\omega t) \tag{2.27}$$

$$\sin(A\sin(\omega t)) = 2\sum_{j=1} J_{2j-1}(A)\sin((2j-1)\omega t) \tag{2.28}$$

where J_n is the n-th Bessel function.

In the experimental setup, the PEM is configured such that $A = 2.4048$. This is chosen because $J_0(2.4048) = 0$, greatly simplifying the derivation

and interpretation of experimental results. Using this, and filling eqs. (2.27) and (2.28) into eq. (2.26) yields

$$\begin{aligned} I = \frac{I_0}{4}(a - [b\sin(\delta_0(\lambda)) + c\cos(\delta_0(\lambda))]2\sum_{j=1} J_{2j-1}(A)\sin((2j-1)\omega t) \\ + [b\cos(\delta_0(\lambda)) - c\sin(\delta_0(\lambda))]2\sum_{j=1} J_{2j}(A)\sin(2j\omega t)) \end{aligned} \tag{2.29}$$

Two lock-in amplifiers are connected to this output, one detecting at ω and the other at 2ω. The detected intensities become

$$I_{DC} = \frac{I_0}{4}a \tag{2.30}$$

$$I_\omega = -\frac{I_0}{4}[b\sin(\delta_0(\lambda)) + c\cos(\delta_0(\lambda))]2J_1(A) \tag{2.31}$$

$$I_{2\omega} = \frac{I_0}{4}[b\cos(\delta_0(\lambda)) - c\sin(\delta_0(\lambda))]2J_2(A) \tag{2.32}$$

These equations can be used to relate the measured signal to circular birefringence and dichroism. Faraday rotation is magnetic circular birefringence, and so a sample that displays Faraday rotation or magnetic circular dichroism can be described as having a magnetic-field dependent circular birefringence or circular dichroism. If the sample does not display any other anisotropy, its normalized Mueller matrix can be approximated as[148, 149]

$$M_{CB/CDSample} = \begin{bmatrix} 1 & 0 & 0 & CD \\ 0 & 1 & CB & 0 \\ 0 & -CB & 1 & 0 \\ CD & 0 & 0 & 1 \end{bmatrix} \tag{2.33}$$

Using definition of a, b and c (eqs. (2.13) to (2.15)), eqs. (2.31) and (2.32) become

$$I_\omega = -I_{DC}[CB\sin(\delta_0(\lambda)) + CD\cos(\delta_0(\lambda))]2J_1(A) \tag{2.34}$$

$$I_{2\omega} = I_{DC}[CB\cos(\delta_0(\lambda)) - CD\sin(\delta_0(\lambda))]2J_2(A) \tag{2.35}$$

With knowledge of $\delta_0(\lambda)$ it would now be possible to determine the circular birefringence and dichroism of a sample. Two possible approaches exist to this problem. The first, described in section 2.4.2, employs an ideal PEM approximation. The alternative is to characterize $\delta_0(\lambda)$, which is described in section 2.4.3.

2.4.2 Measuring circular birefringence and dichroism with an ideal PEM

Under the assumption of an ideal PEM with little or no static strain ($\delta_0(\lambda) \approx 0$), eqs. (2.34) and (2.35) simplify to

$$I_\omega = I_{DC} \cdot CD \cdot 2J_1(A) \tag{2.36}$$

$$I_{2\omega} = I_{DC} \cdot CB \cdot 2J_2(A) \tag{2.37}$$

$$CD = \frac{I_\omega}{I_{DC} 2J_1(A)} = 0.9630 \frac{I_\omega}{I_{DC}} \tag{2.38}$$

$$CB = \frac{I_{2\omega}}{I_{DC} 2J_2(A)} = 1.1579 \frac{I_{2\omega}}{I_{DC}} \tag{2.39}$$

These are the well-known results that linearly correlate the size of the observed signals on both lock-in amplifiers to the circular dichroism and birefringence present in the samples.[154] Under this approximation, it is possible to measure e.g. Faraday rotation by detecting at 2ω without needing to take into account any circular dichroism present in the sample.

2.4.3 Measuring circular birefringence and dichroism with a real PEM

The previous section used the simplification that $\delta_0(\lambda) \approx 0$. For a real PEM, this is not always a correct simplification, and in order to verify it, it is necessary to measure a sample that meets certain requirements. A sample is required with no natural or magnetic circular dichroism, and no linear birefringence or dichroism. Such a sample is easily found, e.g. toluene. For this sample,[148] $m_{03} = 0$ and $m_{13} = 0$, and so $a = 1$, $b = CB$ and $c = CD = 0$. We can then divide eq. (2.34) by eq. (2.35)

$$\frac{I_\omega}{I_{2\omega}} = \frac{-I_{DC}[CB \sin(\delta_0(\lambda)) + CD \cos(\delta_0(\lambda))] 2J_1(A)}{I_{DC}[CB \cos(\delta_0(\lambda)) - CD \sin(\delta_0(\lambda))] 2J_2(A)} \tag{2.40}$$

$$\frac{I_\omega}{I_{2\omega}} = \frac{-\sin(\delta_0(\lambda)) J_1(A)}{\cos(\delta_0(\lambda)) J_2(A)} \tag{2.41}$$

$$\tan(\delta_0(\lambda)) = \frac{I_\omega J_2(A)}{I_{2\omega} J_1(A)} \tag{2.42}$$

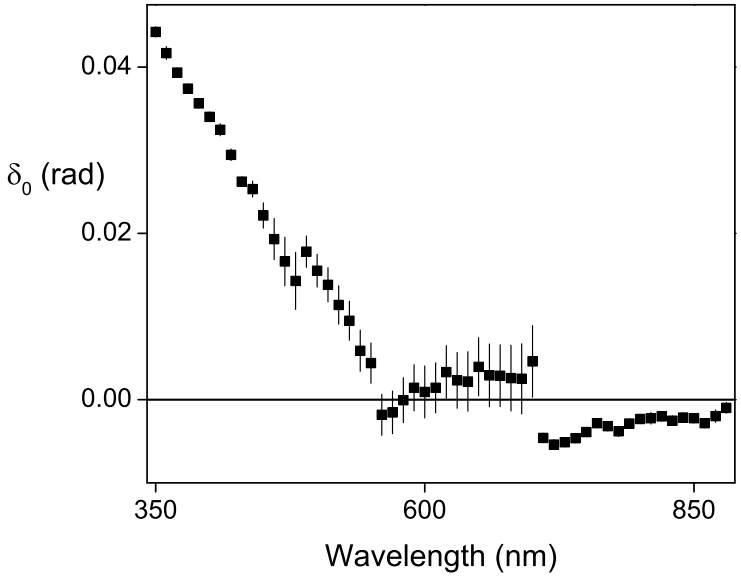

Figure 2.2: δ_0 of the employed PEM shows a typical decline towards longer wavelengths. At wavelengths longer than 550 nm δ_0 is smaller than the detection limit. At shorter wavelengths it becomes significantly larger than 0, invalidating the ideal PEM approximation ($\delta_0 \approx 0$).

And because $J_1(2.4048) = 0.5192$ and $J_2(2.4048) = 0.4318$

$$\tan(\delta_0(\lambda)) = 0.8316 \frac{I_\omega}{I_{2\omega}} \tag{2.43}$$

For each wavelength where $I_{2\omega} \neq 0$, it is now possible to calculate $\delta_0(\lambda)$. In order to induce $I_{2\omega} \neq 0$, a magnetic field is applied, causing Faraday rotation. We performed the measurements from 350 nm to 880 nm on toluene in a quartz cuvette with an optical path length of 1 cm, in magnetic fields up to 1 T. For each wavelength, the value detected by the lock-in amplifiers (I_ω and $I_{2\omega}$) was recorded for a discrete set of magnetic fields. Using eq. (2.43) it is possible to determine δ_0 .

δ_0 of the employed PEM shows a typical decline towards longer wavelengths (fig. 2.2).[155] At wavelengths longer than 550 nm δ_0 is smaller than the detection

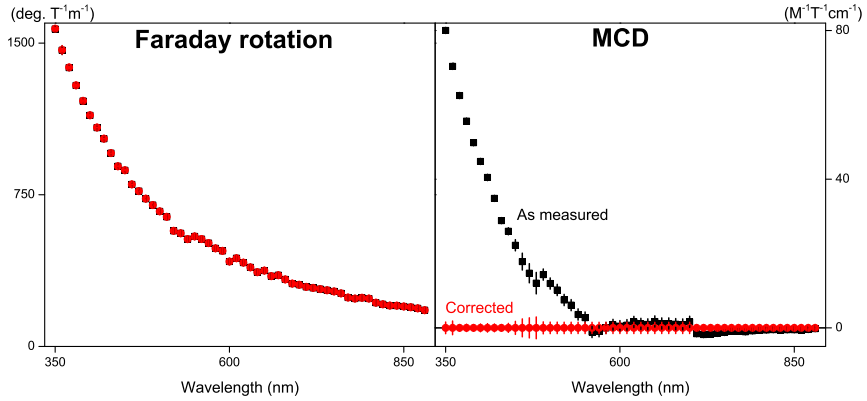

Figure 2.3: Correcting the measured signals for PEM non-idealities reveals significant differences in the data, which is even more clear when one of the signals is at least an order of magnitude larger than the other.

limit. At shorter wavelengths it becomes significantly larger than 0, invalidating the ideal PEM $\delta_0 \approx 0$ approximation frequently used. At 350 nm, $\delta_0 > 0.04$ rad, resulting in $\sin(\delta_0) > 0.04$, causing a signal "leakage" of the circular birefringence into the circular dichroism of more than 4 %. The effect of this leakage on measurements can be demonstrated by filling in eqs. (2.34) and (2.35) with the correct value of δ_0, and deriving the actual Faraday rotation and MCD.

When a magnetic field is applied to toluene, there is large circular birefringence and no circular dichroism. Taking into account PEM non-idealities, the measured Faraday rotation is almost unchanged from the ideal PEM approximation ($< 0.1\%$). The MCD is however greatly influenced, changing from an apparent nonzero signal, increasing with decreasing wavelength, to a zero signal (fig. 2.3). This false positive illustrates the importance of taking PEM non-idealities into account, particularly at shorter wavelengths. A small MCD contribution at a short wavelength can be entirely indiscernible due to the leakage of Faraday rotation signal into the MCD channel.

2.5 Discussion and perspectives

Controlling the polarization of light is an important domain of research. In order to be able to (magneto-) optically characterize novel materials to control the polarization of light, we designed a single PEM experimental setup. We

theoretically analyzed and experimentally characterized the effect of non-idealities in the PEM on our data. The theoretical results can be summarized by eqs. (2.34) and (2.35), from which it is apparent that PEM non-idealities cause leakage of signal from the circular dichroism to the circular birefringence channel and vice versa. For our PEM, δ_0, calculated via eqs. (2.34) and (2.35) from measurements on toluene, increases towards shorter wavelengths, reaching a value of more than 0.04 rad at 350 nm, invalidating the ideal PEM approximation. Because $\sin(\delta_0) > 0.04$, a leakage of CD signal into the CB channel and vice versa occurs, at more than 4 %. At these values, the ideal PEM approximation to measure Faraday rotation or circular dichroism no longer holds, and the effect of δ_0 on the signal must be taken into account.

Our conclusion also holds for more general setups such as CD spectrometers. Leakage between channels becomes more important towards shorter wavelengths, and can even dominate the measurements when CD and CB differ by more than an order of magnitude.

We have demonstrated the necessity to take PEM non-idealities into account when working with PEMs, especially at shorter wavelengths or when dealing with signals spanning different orders of magnitude. PEM non-idealities, while frequently neglected in experimental setup design and theoretical derivations, are expected to be more complicated and possibly exert a larger influence on obtained results for experimental setups with multiple PEMs.

Chapter 3

Faraday rotation and dispersion in the visible region for saturated organic liquids

Chapter 2 described the experimental setup necessary for Faraday rotations in detail. Using this setup we tried to gain insight into the Faraday rotation of organic materials. Our goal was to identify trends, and using the acquired information to be able to predict Faraday rotation in organic materials. With this information we wanted to enable the rational design of organic materials with large Faraday rotation.

This chapter is an article published in Physical Chemistry Chemical Physics in 2013, adapted to form for this dissertation. The supporting information in appendix B contains tables of the measured and calculated Verdet constants for the liquids considered in the article. For reasons of comparison to other computational results we report our calculations in atomic units; the conversion to SI units is also provided in appendix B.

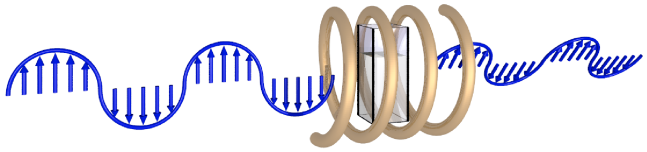

Faraday rotation and its dispersion in the visible region for saturated organic liquids
Physical Chemistry Chemical Physics (2012), 14 (6), 1860–1864
S. Vandendriessche, V. K. Valev and T. Verbiest

3.1 Abstract

Faraday rotation and its dispersion have been measured and calculated in the 400 nm to 800 nm wavelength range for a set of saturated organic liquids. The resulting Verdet constants are fitted and trends are analyzed. Comparisons are made to both the polarizability and diamagnetic susceptibility. The data is applied to a connectivity index model, allowing prediction of Verdet constants of aliphatic organic liquids from 400 nm to 800 nm. The observed correlations and connectivity model improve the understanding of Faraday rotation in diamagnetic materials, allowing for future optimization.

3.2 Introduction

The Faraday effect is a magneto-optical effect in all materials discovered by Michael Faraday.[17] Faraday rotation is the rotation of linearly polarized light in the plane of polarization due to magnetically induced birefringence. It is described by the formula

$$\theta = VBd \tag{3.1}$$

where θ is the polarization rotation, V is the Verdet constant, B is the magnetic field parallel to the propagation direction of light and d is the length of propagation in the dielectricum through the magnetic field. Unlike natural optical rotation, Faraday rotation is non-reciprocal, which means reflections through a sample accumulate rotation and do not cancel out. As such Faraday rotation can be used to design optical switches, modulators, optical isolators[59] and magnetic field sensors.[156]

The Verdet constant V is a wavelength dependent material property. It is important to make the distinction between the molecular Verdet constant and the Verdet constant of the corresponding liquid. Neglecting solvent effects, both Verdet constants are related by the numerical density n of the liquid

$$V_{\text{molecular}} = nV_{\text{liquid}} \tag{3.2}$$

In regions far from absorption it is possible to write the dependence of the Verdet constant as a quadratic function of the wavelength[25]

$$V = A + \frac{B}{\lambda^2} \tag{3.3}$$

where A and B are fitting parameters and λ is the wavelength.

Many calculations of Verdet constants of small organic molecules have been performed with various computational methods,[30–33, 66, 157–159] and measurements have been performed at various wavelengths for certain organic liquids.[66, 160–162] However, to our knowledge no attempt has been made to calculate, measure and model the dispersion of Faraday rotation for a series of organic molecules. As such a total understanding of the Faraday rotation in diamagnetic substances is lacking. We have measured the Faraday rotation and its dispersion for a representative series of branched, unbranched and cyclical alkanes, alcohols and ethers. With the applied connectivity index model it is possible to predict Verdet constants for saturated organic molecules from 400 nm to 800 nm. This predictive ability and the observed correlations will allow further insight into understanding and optimizing magneto-optical phenomena in diamagnetic materials.

3.3 Experimental

Spectral Faraday rotation measurements were performed on a 150 W Xenon lamp followed by a monochromator. After being linearly polarized, the beam passes through a photoelastic modulator (Hinds I/FS50) at 45 degrees respective to the polarization of the light, operating at 50 kHz. Subsequently this beam passes through an optical quartz cuvette with 1 cm path length placed in a DC magnet (HTS-110). Finally the beam passes through an analyzer (45 degrees with respect to the first polarizer). After the beam is detected by a photomultiplier tube, the signal at 100 kHz is analyzed by a lock-in amplifier (SR830). The magnetic field was varied discretely from 0 T to 0.8 T and the signal was measured at each magnetic field. The resulting values were fit linearly to the magnetic field in order to derive the rotation of the sample as a function of the magnetic field.[27] The use of a DC magnetic field avoids the measurement of leakage of the magnetic field into the photomultiplier tube.[25] Dividing the obtained rotation by the path length of the cell resulted in the Verdet constant of the liquid. The molecular Verdet constant was derived from the Verdet constant of the liquid using the numerical density of the liquid calculated from the molar mass and density from the CRC Handbook of Chemistry and Physics.[163]

Molecular polarizabilities were obtained using the Lorentz–Lorenz equation[157] for refractive indices measured on an Atago DR-A1 Refractometer operating at 589 nm.

Verdet constants were calculated using Dalton[164] with 6-31+G** MP2 full-optimized structures obtained from the CCCBDB.[165] A quadratic response

method at the B3LYP/aug-cc-pVDZ approximation was used as described by Botek et al.[66]

3.4 Results and discussion

3.4.1 Trends for alkanes and alcohols

In figs. 3.1 and 3.2 the A and B parameter obtained by fitting the calculated and measured molecular Verdet constants to eq. (3.3) for unbranched alkanes and alcohols is displayed as a function of the number of carbon atoms.

For both A and B, a linear trend is observed as a function of the number of carbon atoms, and for both series of compounds the linear fit values are displayed in table 3.1. The uncertainty on the A values is much larger than the uncertainty on the B values. This is inherent to the dispersion formula (eq. (3.3)), in which the A value is a measure for an extrapolation to $\lambda \to \infty$, where the measured values approach 0.

All the slopes of calculated values are smaller than the slopes of measured values. This corresponds well to the known tendency of quadratic response calculations performed at the B3LYP/aug-cc-pVDZ level to result in lower calculated Verdet constants than measured.[66] For the unbranched alkanes, a 20 % smaller slope is obtained for the calculated B values than for the measured B values. This underestimation is reduced to 15 % for the unbranched alcohols. The slope for the measured B values is very similar for both series. Combined with the observed linear trend as a function of the number of carbon atoms this leads to the postulation of an additive model, where each additional CH_2 moiety contributes equally to the Verdet constant. While this is applicable to linear chain length extension, it is necessary to take into account longer-range interactions and changes in molecular structure in order to predict the Verdet constant for arbitrary molecules. This is further investigated in section 3.4.4. There is a deviation from the linear trend expected for the additive model in the experimental A values of the unbranched alcohols, which is attributed to intermolecular interaction such as hydrogen bonding. This explanation is supported by the observation that the linear trend is present in the calculated A values for the unbranched alcohols, which neglect intermolecular interactions. Additionally no deviation is observed for the experimental A values of the unbranched alkanes, for which intermolecular interactions are expected to be smaller than in the unbranched alcohols.

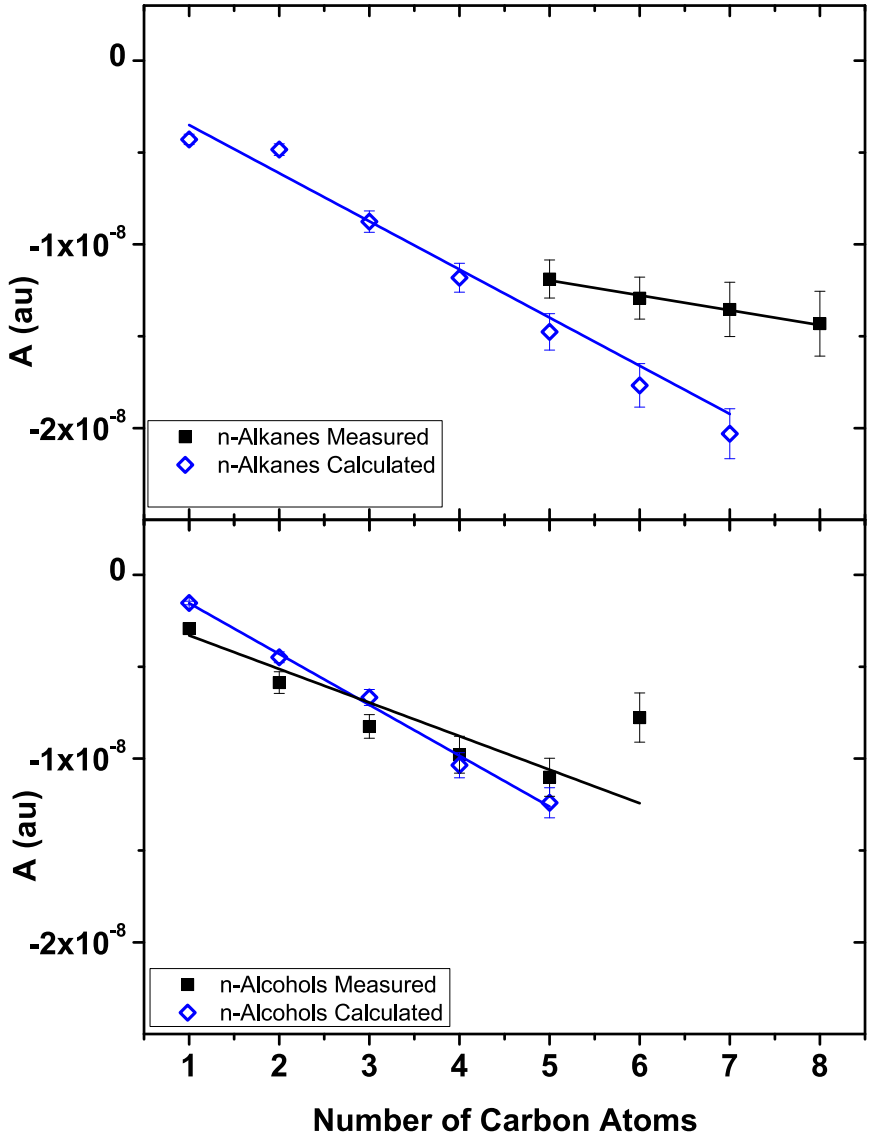

Figure 3.1: The A parameter from eq. (3.3) for the calculated and measured Verdet constant of unbranched alkanes and alcohols as a function of the number of carbon atoms. A linear decrease is seen for both the calculated ($R^2 > 0.97$) and the measured ($R^2 = 0.92$, $R^2 = 0.81$) Verdet constants as a function of the number of carbon atoms.

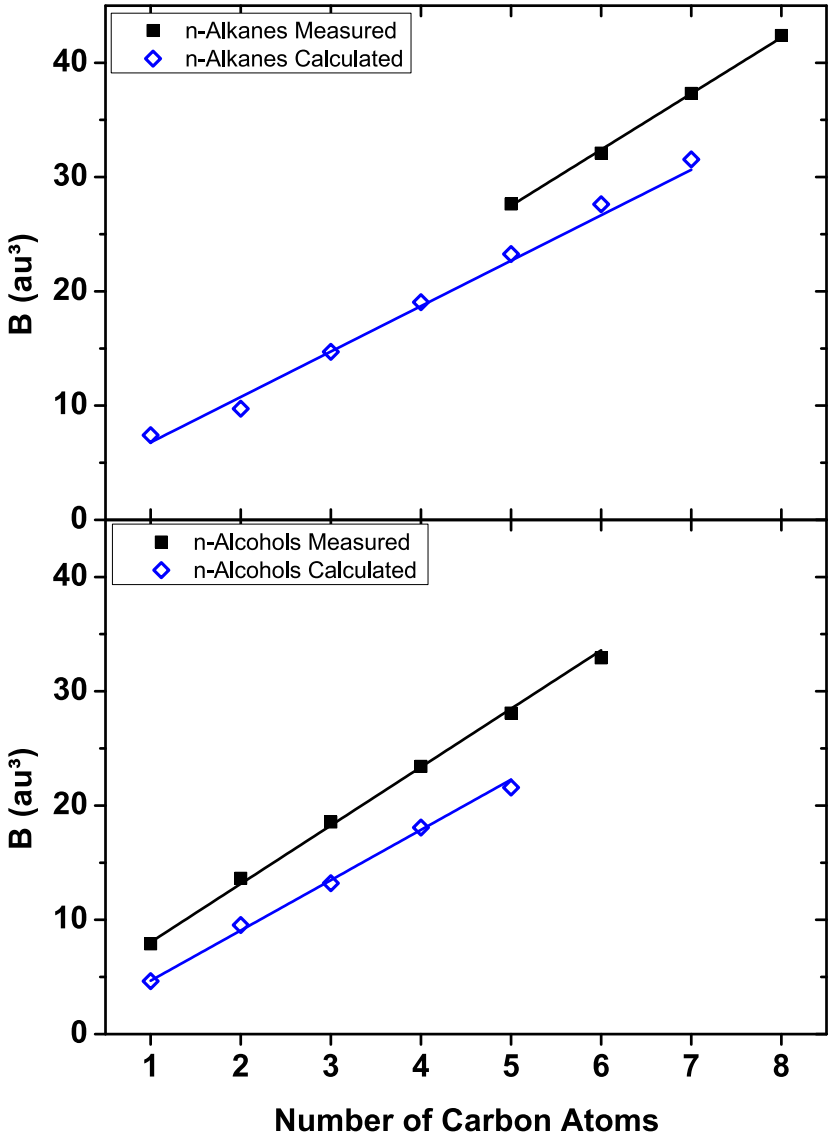

Figure 3.2: The B parameter from eq. (3.3) for the calculated and measured Verdet constant of unbranched alkanes and alcohols as a function of the number of carbon atoms. A linear increase ($R^2 > 0.97$) is seen for both the calculated and the measured Verdet constants as a function of the number of carbon atoms.

Table 3.1: Result of the linear fit of the A and B parameter for calculated and measured unbranched alkanes and alcohols as a function of the number of carbon atoms

	unbranched alkanes	unbranched alcohols
slope of measured A values	-0.81×10^{-9} au	-1.83×10^{-9} au
slope of calculated A values	-2.62×10^{-9} au	-2.77×10^{-9} au
slope of measured B values	$4.91\,\mathrm{au}^3$	$5.11\,\mathrm{au}^3$
slope of calculated B values	$3.98\,\mathrm{au}^3$	$4.40\,\mathrm{au}^3$

3.4.2 Relation to the diamagnetic susceptibility

It is interesting to compare Faraday rotation to diamagnetic susceptibility.[163] While this comparison has already been made for parameters of the macroscopic Verdet constant of the liquid,[162] it is more instructive to compare the diamagnetic susceptibility to fits to the microscopic, molecular Verdet constant. The Verdet constants of a variety of saturated organic liquids, including alkanes, alcohols and ethers were calculated and measured over the 400 nm to 800 nm wavelength region and can be found in supporting information online. The resulting A and B parameters are shown in fig. 3.3.

A linear correlation between both parameters and the diamagnetic susceptibility is observed. However, the correlation is significantly stronger for the B parameter (calculated values: $R^2 = 0.889$, measured values: $R^2 = 0.978$) than for the A parameter (calculated values: $R^2 = 0.793$, measured values: $R^2 = 0.811$). The weaker fit for the A parameter is due to the inherent lower precision on the A parameter, as described in section 3.4.1. Again we observe a smaller slope for the calculated B values (0.444×10^6 mol au^3 cm^{-3}) than for the measured B values (0.393×10^6 mol au^3 cm^{-3}). The weaker correlation for the calculated values can be understood in terms of the chosen basis set for the calculations. When basis sets with a larger number of valence orbitals are chosen, the value of the calculated Verdet constant approaches the measured one at a different rate for calculations with different number of electrons and orbitals. As such at a given level of approximation, the deviation from the infinite orbital limit value of the Verdet constant for this type of calculation differs per molecule, and this weakens the observed correlation. The chosen level of approximation provides sufficient accuracy to reproduce the trends. Higher levels of approximation provide higher accuracy, but due to the slow convergence of magneto-optical calculations with the increase of number of orbitals,[33] the computational time - accuracy trade off favors the employed approximation.

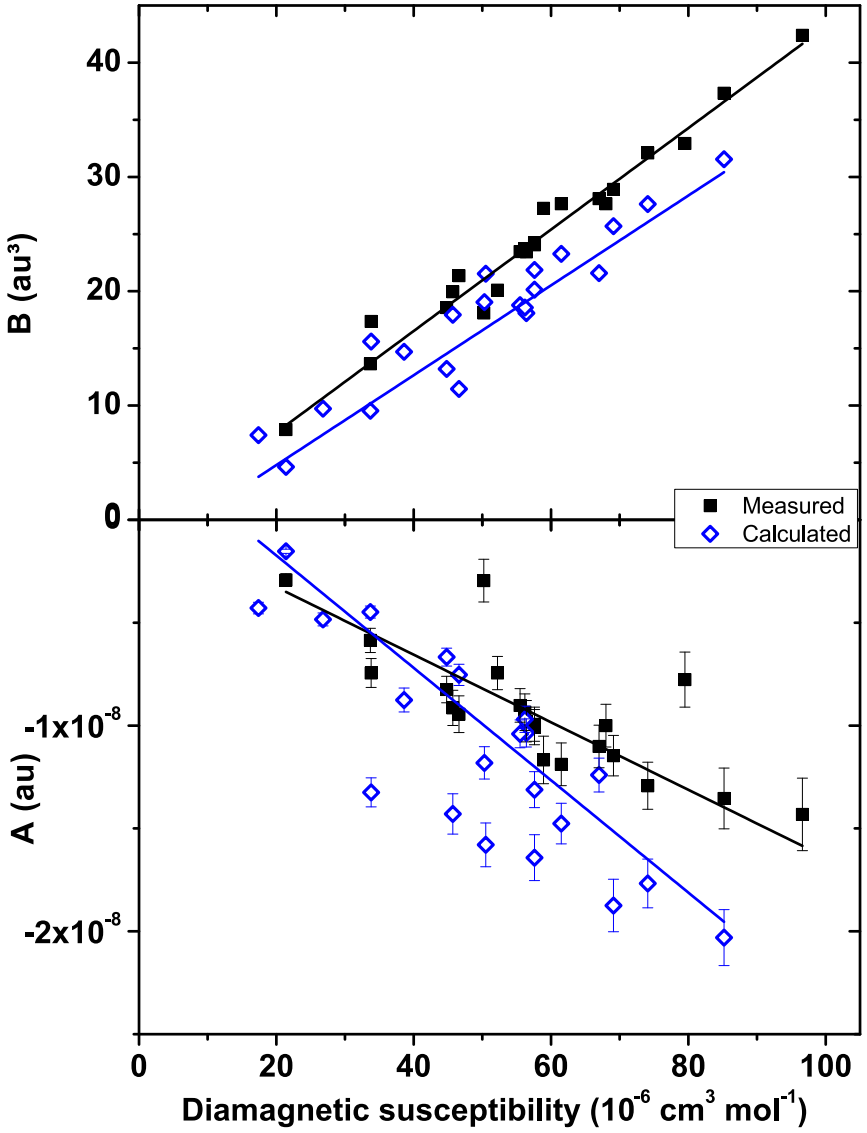

Figure 3.3: The A and B parameter from eq. (3.3) for the calculated and measured Verdet constants of a variety of aliphatic liquids as a function of the diamagnetic susceptibility. A linear relation is seen for both the calculated and the measured Verdet constants, with a stronger correlation seen for the B parameter.

3.4.3 Relation to the molecular polarizability

The Becquerel formula predicts a linear relation between the derivative of the polarizability to the frequency[158] and the Verdet constant at that frequency. Data on the dispersion of refractive indices is however difficult to obtain accurately. The refractive index on the other hand is relatively simple to determine. Despite the fact that the refractive index and molecular polarizability are not used in the calculation of the Faraday rotation from the measured data, we also observe a linear relation between the molecular polarizability and the molecular Verdet constant at the same wavelength, displayed in fig. 3.4.

A larger slope ($291 \times 10^{-11}\,\mathrm{au}^3$ with $R^2 = 0.985$) is obtained for the measured B values than for the calculated B values ($253 \times 10^{-11}\,\mathrm{au}^3$ with $R^2 = 0.911$). This correlation provides a practical method for estimating Verdet constants

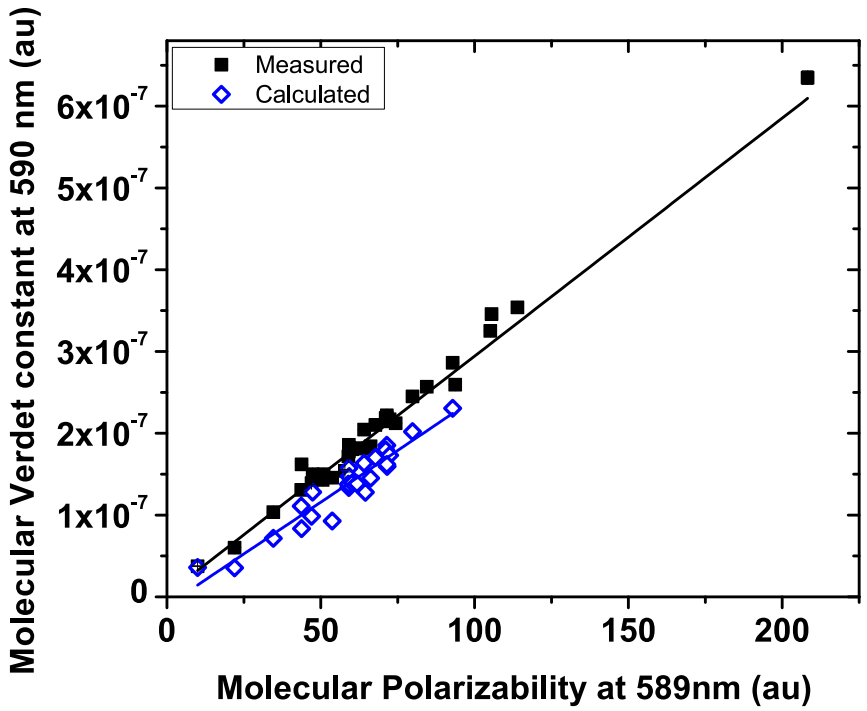

Figure 3.4: The Verdet constant at 590 nm as a function of the molecular polarizability at 589 nm. A linear relation is seen for both the calculated and the measured Verdet constants.

at a specific wavelength, given the ease of measuring the refractive index in a refractometer.

More interestingly, a correlation was also found between the molecular polarizability at 589 nm and the A and B parameters of eq. (3.3) (fig. 3.5). Once more the linear trend is stronger for the B values than for the A values, for the same reasons explained in section 3.4.1.

This relationship allows the prediction of the Verdet constant of a liquid over a wide wavelength range with a single measurement of a refractive index at an arbitrary wavelength.

3.4.4 Modeling the Verdet constant

While the linear relation to the diamagnetic susceptibility and molecular polarizability allows for accurate estimates of the Verdet constant, these variables are not sufficient to fully explain the observed Verdet constant. This is illustrated by 1-butanol and 2-butanol, which both have a molecular polarizability of (59.14 ± 0.34) au, but respective B parameters of $(23.44 \pm 0.14)\,\mathrm{au}^3$ and $(24.26 \pm 0.11)\,\mathrm{au}^3$.

Due to the observed correlation between the diamagnetic susceptibility and the B parameter of the Verdet constant fit, it is most obvious to investigate a modified model for the prediction of the diamagnetic susceptibility. The most straightforward model is to decompose the molecule into fragments and, using Pascal's constants,[166] assign each a contribution to the diamagnetic susceptibility of the molecule. Because this model decomposes 1-butanol and 2-butanol in the same fragments, it also fails to distinguish between these two molecules; as such it is necessary to apply a more complex model.

To account for effects over more than one bond, a molecular connectivity index model is applied. A recent connectivity index, designed for the modeling of diamagnetic susceptibilities,[167] has been chosen. The details on molecular connectivity indices are beyond the scope of this paper and can be found elsewhere.[168] The n-th order molecular connectivity index ${}^{n}\chi_k$ can be written as

$$ {}^{n}\chi_k = \sum_{j=1}^{N_n} \left(\prod_{i=1}^{n+1} \frac{1}{\sqrt{\delta'_i}} \right)_j \tag{3.4} $$

Where n is the order of the molecular connectivity index, k is a contiguous path type of fragment, N_n is the number of relevant paths and δ'_i is the chosen atomic connectivity index. To illustrate the calculation of the molecular connectivity

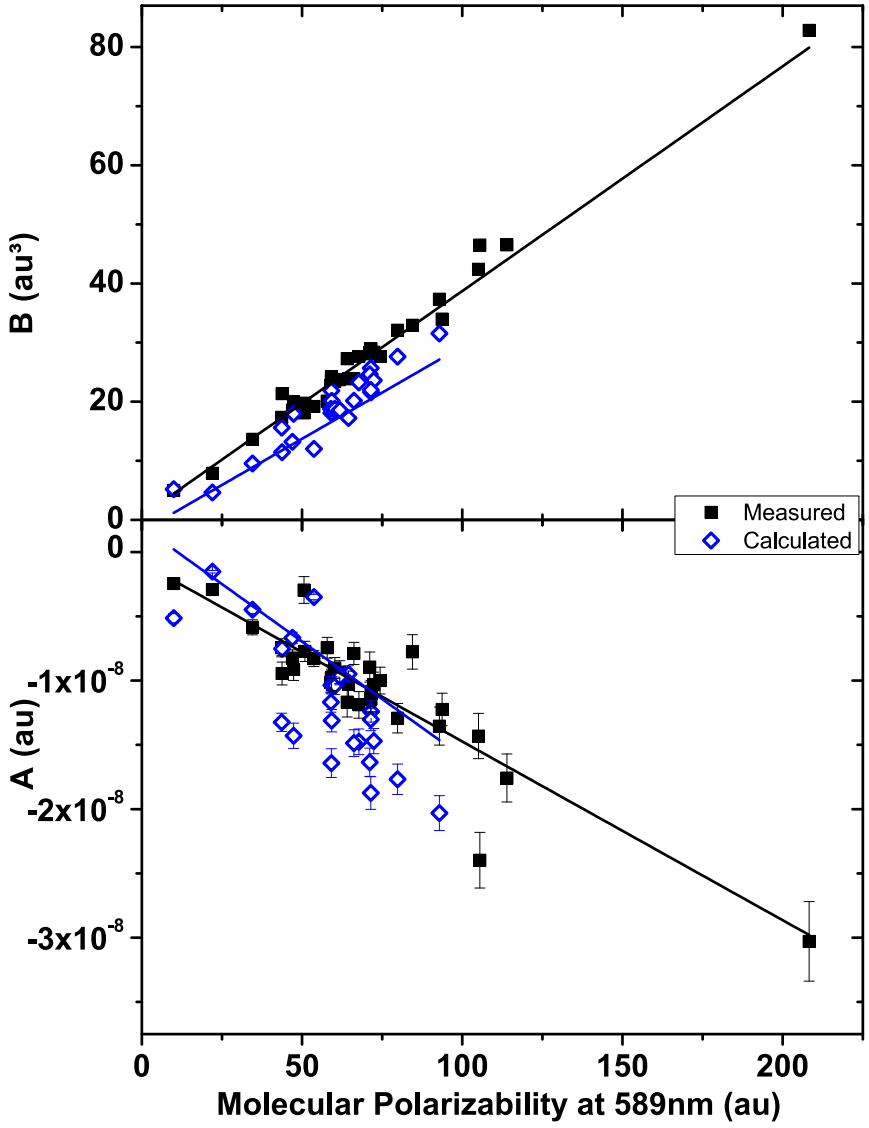

Figure 3.5: The A and B parameters from eq. (3.3) for the calculated and measured Verdet constants as a function of the molecular polarizability at 589 nm. A linear relation is seen for both the calculated and the measured Verdet constants.

indices we take ethanol as an example. The zeroth order molecular connectivity index can be calculated as follows

$$^{0}\chi_k = \frac{1}{\sqrt{\delta'_C}} + \frac{1}{\sqrt{\delta'_C}} + \frac{1}{\sqrt{\delta'_O}} \tag{3.5}$$

essentially adding up the contribution of each non-hydrogen atom. The first order molecular connectivity index is

$$^{1}\chi_k = \frac{1}{\sqrt{\delta'_C\delta'_C}} + \frac{1}{\sqrt{\delta'_C\delta'_O}} \tag{3.6}$$

quantifying the contribution of each bond. The second order molecular connectivity index is

$$^{2}\chi_k = \frac{1}{\sqrt{\delta'_C\delta'_C\delta'_O}} \tag{3.7}$$

which is the contribution of the two-bond fragment C-C-O.

We have chosen an atomic connectivity index δ'_i designed by Mu et al. [167] which takes into account the chemical environment of the atom

$$\delta'_i = \left(\frac{Z_i^v - h_i}{Z_i - Z_i^v - 1}\right)\left(\frac{x_i}{x_{C-sp^3}}\right) \tag{3.8}$$

where Z_i^v and Z_i are respectively the number of valence and total electrons on atom i, h_i is the number of hydrogen atoms connected to atom i, x_i is the orbital electronegativity of atom i and x_{C-sp^3} is the orbital electronegativity of an sp^3 hybridized carbon atom. The orbital electronegativity is defined as

$$x_i = -\frac{\alpha\epsilon_s + (1-\alpha)\epsilon_p}{4.95} \tag{3.9}$$

where α is the composition of the s orbital and ϵ_s and ϵ_p are the energies of respectively the s and p orbital.

Fitting of the chosen connectivity index to the B parameters obtained by fitting of the experimental Faraday rotation data yields

$$B = -0.09531 + 5.13093 \cdot {}^{0}\chi_k + 1.69778 \cdot {}^{1}\chi_k + 0.77308 \cdot {}^{2}\chi_k \tag{3.10}$$

Table 3.2: The B parameter from fits to measurements compared to the predicted B value. A good agreement is seen between the predicted and measured values

	B from measurements (au^3)	Predicted B (au^3)
Methanol	7.893	7.979
Ethane		11.864
Ethanol	13.643	12.828
Dimethylether		13.825
Propane		16.742
Propanol	18.569	17.623
Isopropanol	19.951	18.554
Methoxyethane		18.584
Propylene Glycol	19.756	19.442
1,3-Propanediol	18.102	18.551
Acetone	17.360	17.002
Butane		21.446
Isobutane		22.539
1-Butanol	23.436	22.373
2-Butanol	24.257	23.224
Isobutanol	24.059	23.353
Methoxypropane	22.691	23.385
Diethylether	23.469	23.369
1,2-dimethoxyethane	23.911	25.324
THF	19.180	20.930
1,4 Dioxane	20.100	22.954
Pentane	27.646	26.196
Cyclopentane	23.723	23.656
1-Pentanol	28.094	27.124
2-Pentanol	28.909	27.995
3-Pentanol	28.252	27.932
THP	23.874	25.680
MTBE	28.385	30.329
3-methyl-1-butanol	28.971	28.084
Hexane	32.103	30.946
Hexanol	32.926	31.874
Cyclohexane	27.647	28.407
2-methoxyethylether	33.986	36.848
Heptane	37.328	35.697
Octane	42.399	40.447
Isooctane	46.501	43.731
Dioctylether	82.823	80.474

with $R^2 = 0.987$. The measured and predicted B values are displayed in table 3.2.

A good agreement is seen between the B values from measurements and the predicted values. For the A parameter a much weaker fit is seen, and due to the small influence on the Verdet constant (typically less than 5 % at the measured wavelengths) it is not included in the model. The ${}^2\chi_k{:}{}^1\chi_k$ ratio is 0.46, indicating a significant contribution of two-bond fragments. Despite this the single atom contributions, quantified by ${}^0\chi_k$, remain dominant, in agreement with the observed additivity in section 3.4.1. However, the largest deviation in our model is observed for the ring systems, suggesting that higher order fragments play a non-negligible role in Faraday rotation of diamagnetic substances. As such, future investigations with larger data sets will need to include higher order molecular connectivity indices.

3.5 Conclusions

We have measured the Faraday rotation of various saturated organic liquids between 400 nm and 800 nm, and the resulting values correspond well to previously reported values. From these measurements we have calculated the molecular Verdet constant. By fitting this data to a dispersion formula for Verdet constants sufficiently far from resonance, we are able to quantify the Verdet constant over a broad wavelength region. The Verdet constant shows trends over alkane and alcohol carbon backbone length. Additionally, a linear correlation to both the molecular polarizability and the diamagnetic susceptibility is observed. For further refinement, we apply a molecular connectivity index model based on our measurements in order to predict the Verdet constant for arbitrary aliphatic compounds. With knowledge of the density of the liquid, this allows the prediction of the Faraday rotation of arbitrary aliphatic liquids at a chosen wavelength. The results reveal important contributions of large fragments in the molecules to the Faraday rotation. The ability to predict the Verdet constants and the observed correlations further allow for optimization and a better understanding of magneto-optical phenomena in diamagnetic materials.

Chapter 4

Giant Faraday rotation in mesogenic organic molecules

In our search large Faraday rotation we focused on organic materials due to their advantages over inorganic materials, such as flexibility in processing and synthesis. More specifically, we investigated the Faraday rotation in a class of mesogenic molecules. We showed that these molecules display giant Faraday rotation in a region without spectral features. This chapter is a communication published in Chemistry of Materials in 2013, adapted to form for this dissertation. The supporting information in appendix C contains ^{1}H and ^{13}C NMR spectra of BTB*. S. Van Cleuvenbergen helped with sample preparation. P. Willot, G. Hennrich and G. Koeckelberghs synthesized the necessary organic molecules. Finally M. Srebro and J. Autschbach performed the DFT calculations.

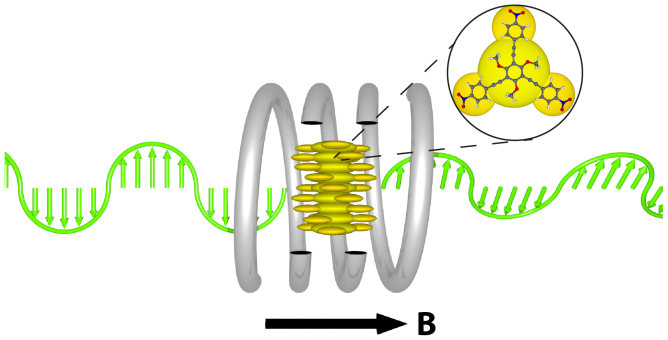

Giant Faraday Rotation in Mesogenic Organic Molecules
Chemistry of Materials (2013), 25 (7), 1139–1143
S. Vandendriessche, S. Van Cleuvenbergen, P. Willot, G. Hennrich, M. Srebro, V. K. Valev, G. Koeckelberghs, K. Clays, J. Autschbach and T. Verbiest

4.1 Abstract

Faraday rotation, the rotation of the polarization of light due to a magnetic field in the direction of propagation of the light, is used in applications ranging from quantum memory to the detection of biomagnetic fields. For these applications large Faraday rotation is necessary, but absorption of light is detrimental. In search of these properties, we have characterized the Verdet constant of a so far unexplored class of mesogenic organic molecules. We report their spectra and provide an interpretation. A Verdet constant of almost $2.5 \times 10^5\,^\circ\,\mathrm{T}^{-1}\,\mathrm{m}^{-1}$ is found around 520 nm. This Verdet constant is 3 orders of magnitude larger than the largest known for organic molecules in a region without spectral features. We attribute this enormous Faraday rotation to resonant enhancement by a triplet excitation that does not appear in the linear absorption spectrum and to near-resonant enhancement by low-energy singlet excitations. Furthermore we are able to switch the Faraday rotation by changing the liquid crystal phase of the compound. These results demonstrate a new class of Faraday rotating materials with great potential to replace current materials and improve existing applications. The inherent flexibility in the synthesis of this class of molecules opens a new field of research in Faraday rotation.

4.2 Introduction

Faraday rotation is the rotation of the plane of polarization of light due to magnetically induced circular birefringence.[17] Discovered almost 2 centuries ago, it is now used in a wide range of applications. Faraday rotation is important for optical isolators,[169] magnetic field sensors,[156] current sensors,[170] displacement sensors,[139] integrated communication optics,[57] detection of biomagnetic fields,[171] quantum memory,[172] and many others. It can be described by

$$\theta = VBd \tag{4.1}$$

where θ is the polarization rotation, V is the Verdet constant, B is the magnetic field parallel to the propagation of light, and d is the length of propagation through the magnetic field.

The Verdet constant is a wavelength dependent material parameter. Typical Verdet constants of materials currently in use, such as iron oxide films[51] or substituted iron garnet films,[173] can reach millions of degrees per tesla per meter in the visible frequency region. However, these paramagnetic materials

suffer from the drawback of magnetic saturation in magnetic fields smaller than 1 T[174] and a large temperature dependence.[175] Organic, diamagnetic materials in contrast saturate at far larger magnetic fields and additionally are relatively insensitive to temperature changes, which is beneficial for sensing applications. An additional advantage of organic materials over inorganic garnets for Faraday rotation is their processability and flexibility.[176] Unfortunately, diamagnetic organic molecules have relatively small Verdet constants in regions far from resonance. Typical Verdet constants are on the order of hundreds of degrees per tesla per meter in the visible wavelength region, displaying a continuous decline toward longer wavelengths.[66, 67, 135, 161, 177] Only for the larger polythiophenes in specific conditions have larger Verdet constants been reported, on the order of $1 \times 10^4 \,^\circ\,\mathrm{T}^{-1}\,\mathrm{m}^{-1}$.[68] However, these large Verdet constants currently lack a conclusive explanation.

In search of large Verdet constants without an associated absorption, we have characterized the Verdet constant of an unexplored class of organic molecules. A band in Faraday rotation is found around 520 nm with a Verdet constant of almost $2.5 \times 10^5 \,^\circ\,\mathrm{T}^{-1}\,\mathrm{m}^{-1}$, 3 orders of magnitude larger than the largest known for an organic molecule in a region without spectral features. We attribute this giant Faraday rotation to resonant enhancement by weakly absorbing triplet states[178–181] that are calculated to be present in this region, as well as near-resonant enhancement due to strongly absorbing singlet states at a wavelength not much shorter than the wavelength window around 520 nm. The lack of a corresponding strong absorption around 520 nm is a great advantage for applications.

We are also able to switch the Faraday rotation by changing the particular phase of the compound. The feature in Faraday rotation is present in the crystalline state under 60 °C but disappears entirely in the isotropic liquid above 130 °C.

These results demonstrate a new class of Faraday rotating materials with great potential to replace current materials and improve existing applications. The inherent flexibility in the synthesis of this class of molecules opens a new field of materials for Faraday rotation.

4.3 Experimental section

1,3,5-tris[(4-nitrophenyl)ethynyl]-2,4,6-tris(*n*-decyloxy)benzene (TTB), 1,3,5-tris[(*S*)-3,7-dimethyloctyloxy]-2,4,6-tris[(4-nitrophenyl)ethynyl]benzene (TTB*) and 1,3-bis[(*S*)-3,7-dimethyloctyloxy)]-5-fluoro-2,4,6-tris[(4-nitrophenyl)ethynyl]-benzene (BTB*) were synthesized as described by Hennrich et al.[182, 183] Thin film samples were created by heating a small amount of material to 120 °C

and allowing this material to spread between two glass plates through capillary action. The resulting transparent samples were of sufficient optical quality for Faraday rotation measurements.

Spectral Faraday rotation measurements were performed using a 150 W xenon lamp followed by a monochromator. After being linearly polarized, the beam passes through a photoelastic modulator (Hinds I/FS50) at 45°, operating at 50 kHz. Subsequently this beam passes through the sample in a DC magnet, where Faraday rotation occurs. Finally the light passes through an analyzer placed at 45° with respect to the first polarizer. The beam then hits a photomultiplier tube, and the resulting signal is analyzed by a lock-in amplifier (SR830) at a detection frequency of 100 kHz. This signal can be correlated to the optical rotation and is measured for a discrete set of magnetic field strengths, with the Verdet constant determined from the slope of these values. We also measured Faraday rotation with a 632.8 nm helium–neon laser and an alternating current magnetic field at 857 Hz as described by Valev et al.[27]

To assist the interpretation of the experimental findings, we performed density functional theory (DFT) computations with the Turbomole package (version 5.7[184, 185]). Taking into account the rather large size of the molecules studied experimentally, the aliphatic tails were replaced by methyl groups to reduce the computational cost. As demonstrated by a comparison between the experimental Faraday rotation spectra of TTB and TTB*, the hydrocarbon chains appear to influence a location of particular bands in the spectrum, but they do not change their general characteristics (vide infra). Accordingly the hydrocarbon chains are unlikely responsible for the characteristic main features observed for the Faraday rotation. Geometry optimizations employed the BP functional[186–188] with a standard Turbomole triple-ζ polarized (TZVP) Gaussian-type basis set.[189] Calculations of the excitation spectra were performed using time-dependent density functional theory (TD-DFT) with the B3LYP functional[190–192] and the triple-ζ polarized (TZVP) basis set. As pointed out by Peach et al., TD-DFT calculations may significantly underestimate triplet excitation energies because of an underlying triplet instability of the ground state.[193] In a Hartree-Fock (HF) calculation, the singlet ground state of the TTB model system is indeed confirmed to have a triplet instability. Peach et al. found that the use of the Tamm-Dancoff approximation (TDA)[194, 195] eliminates much of the problem and provides more accurate triplet excitations. A comparison of the full TD-DFT and TD-DFT/TDA results for our samples shows the expected behavior, namely, a sizable blue shift of the triplet excitations, in particular, when the TDA is applied. The effect is more pronounced with a hybrid functional with a larger fraction of exact exchange (e.g. B3LYP (fig. 4.2) vs. BHLYP (fig. 4.3)).

4.4 Results and discussion

In the experimental Faraday rotation spectrum of TTB a peak with a Verdet constant of almost $2.5 \times 10^5\,^\circ\,\mathrm{T}^{-1}\,\mathrm{m}^{-1}$ is seen centered around 520 nm (fig. 4.1). The feature resembles an anomalous dispersion pattern of a refractive property such as the dipole polarizability around an electronic resonance, with a peak followed by a trough when going from longer to shorter wavelengths, superimposed onto a normal dispersion created by intense absorptions at higher energy (wavelengths shorter than 500 nm). In addition, strong Faraday rotation is observed below 450 nm due to resonant enhancement by absorption at these wavelengths. In the absorption spectrum on the other hand, only one band is observed with a center wavelength shorter than 400 nm, with no peaks past 500 nm.[182]

It is necessary to verify first that the observed feature is indeed caused by Faraday rotation. Faraday rotation is linear as a function of the applied magnetic field (eq. (4.1)). The optical rotation measured in a DC magnetic field is also linear as a function of the magnetic field ($R^2 > 0.99$), with no saturation being visible until at least 1 T. Despite this, it is not possible to exclude the magnetic alignment of crystallites as a source of optical rotation. To support Faraday rotation as the source of the observed magnetic field dependent optical rotation, we also performed Faraday rotation measurements in an alternating current magnetic field. In these measurements, the same Faraday rotation was observed. The high modulation frequency of the magnetic field allows us to exclude a magnetic alignment as the cause of the observed magnetic field dependent optical rotation. We can conclude that the feature in the observed optical activity is indeed Faraday rotation.

The Verdet constant is a molecular property that is defined by three perturbations:[29, 33, 158] two frequency-dependent electric fields and a static magnetic field. Resonant enhancement may occur via strongly or weakly electric-dipole-allowed transition, and potentially also via magnetic-dipole-allowed but electric-dipole-forbidden transitions. A corresponding band is not visible in the linear absorption spectrum of the molecule, indicating the lack of any significant electric-dipole-allowed transition. This excludes the possibility of resonant enhancement by an intermolecular charge-transfer excitation induced by aggregation. Nonetheless, formally electric-dipole-forbidden transitions with weak intensity such as singlet-triplet transitions can also resonantly enhance Faraday rotation.[178–181] Computations and careful experiments on related 3-fold symmetrical molecules indicate the presence of triplet states close to these energies.[196]

We calculated the electronic states of TTB for the propeller geometry adopted

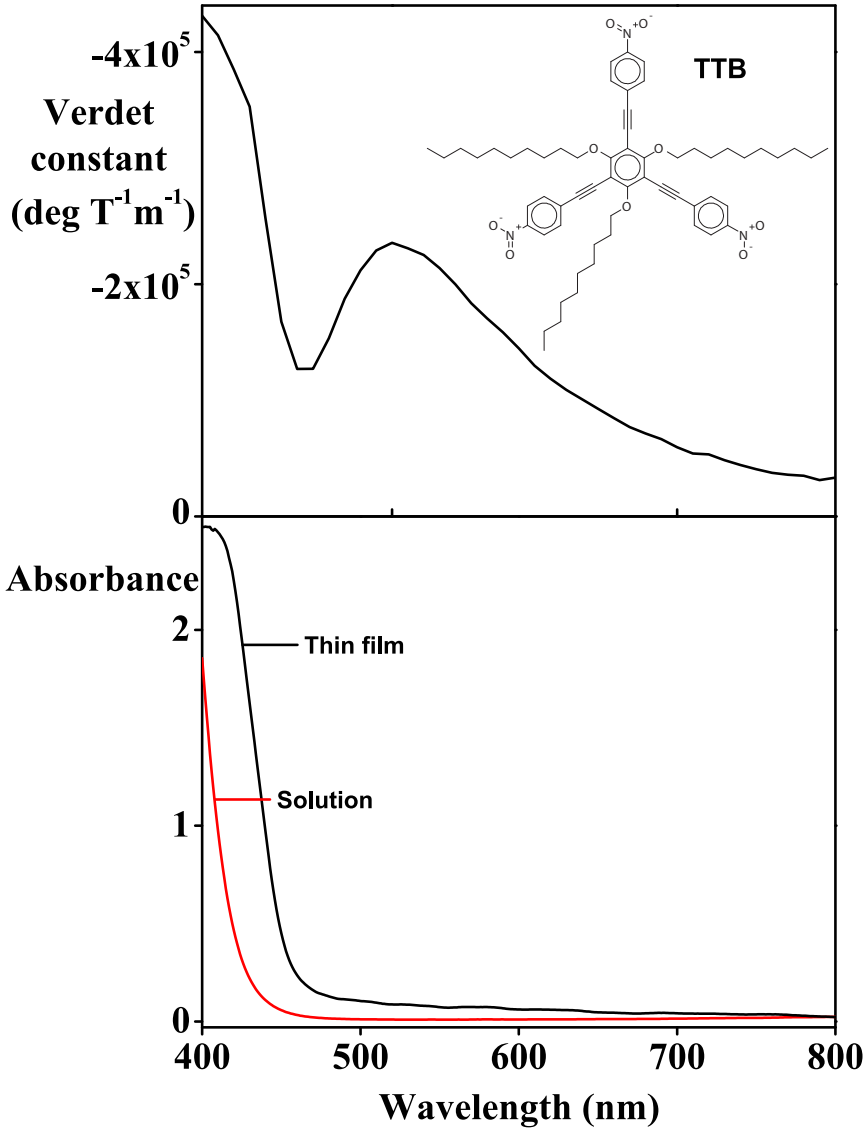

Figure 4.1: In the experimental Faraday rotation spectrum of a 1.8 µm film of TTB (top) a peak is seen at 520 nm, associated with an anomalous dispersion feature attributed to a triplet excited state near this wavelength. The transition to the triplet excited state is not visible in the absorption spectrum in thin film (bottom, black) or solution (bottom, red) because it is formally spin-forbidden.

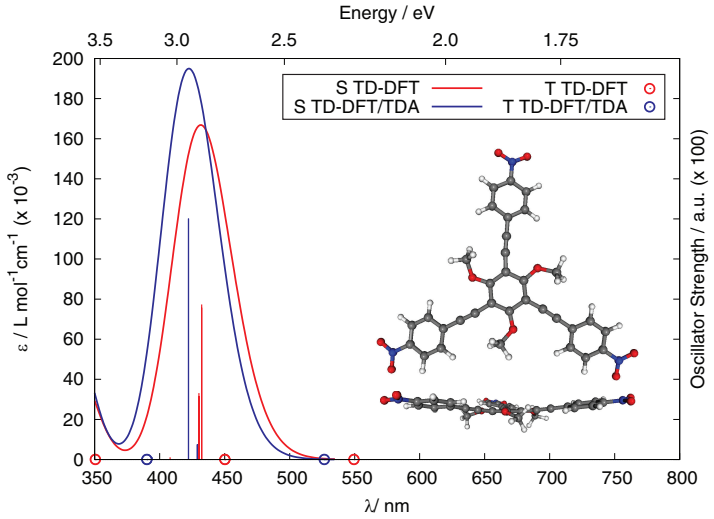

Figure 4.2: TD-DFT B3LYP/TZVP calculations on the optimized model TTB geometry reveal a triplet excitation at 527 nm, corresponding to the region where the Faraday rotation is observed. S/T stands for singlet/triplet excitation energies calculations.

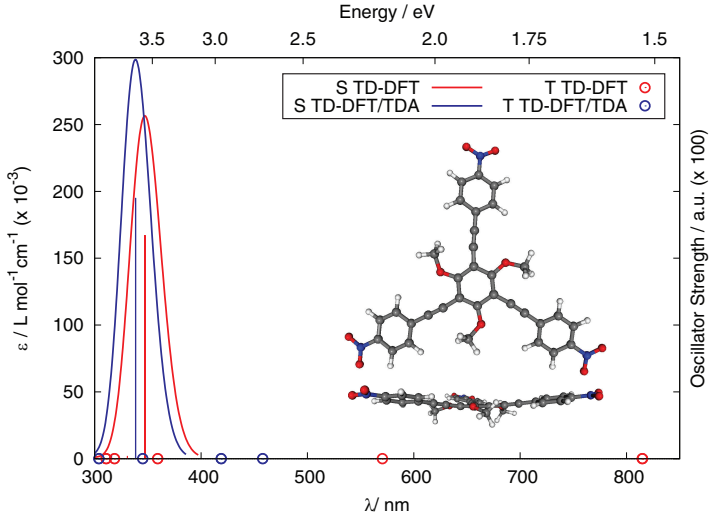

Figure 4.3: Calculated absorption spectrum for TTB model molecule (propellor-like geometry) with indication of triplet excitations. TD-DFT BHLYP/TZVP computations applying RPA (red) or TDA (blue).

Table 4.1: B3LYP/TZVP triplet excitations with a large spin-free component of transition dipole for TTB and BTB* model molecules

RPA				TDA			
#	E /eV	λ /nm	f	#	E /eV	λ /nm	f
TTB propellor-like geometry							
2	2.26	550	2.2379	2	2.35	527	1.9892
3	2.26	549	2.2365	3	2.35	527	1.9884
7	2.75	450	0.4454	7	3.18	390	0.2169
8	2.75	450	0.4266	8	3.18	390	0.2301
9	2.75	450	0.4175	9	3.18	390	0.2390
17	3.54	350	0.3268	17	3.59	345	0.3590
18	3.54	350	0.3270	18	3.59	345	0.3591
BTB*							
2	2.31	537	1.9922	2	2.41	514	1.7586
3	2.34	531	2.4732	3	2.45	506	2.1877
5	2.74	452	0.4274	7	3.17	391	0.2251
6	2.75	452	0.4309	8	3.17	391	0.2278
7	2.75	451	0.4235	9	3.17	391	0.2180
17	3.59	346	0.1904	17	3.64	341	0.1801
18	3.62	342	0.2224	18	3.67	337	0.2352

in crystals[97](fig. 4.2). Triplet excitations with a large spin-free component of the transition dipole are present around 527 nm (see table 4.1), corresponding to the region where the Faraday rotation is observed.

While this excitation is formally spin-forbidden, and as such not visible in the absorption spectrum, it may resonantly enhance the Faraday rotation. No electric-dipole-forbidden but magnetic-dipole-allowed singlet transition was calculated at wavelengths longer than 450 nm which would therefore exclude a mechanism via resonance with electric-dipole or magnetically allowed singlet transition in the wavelength window of interest.

To shed more light on the hypothesis of a resonant enhancement by a weakly absorbing triplet state, we examined two structurally related molecules. TTB* has a blue-shifted and narrower feature in Faraday rotation (fig. 4.4) than TTB (fig. 4.1). The bulkiness of the branched alkyl chains impedes a close packing of molecular units but guarantees for a fixed propeller confirmation on the molecular level and a helical twist in the resulting bulk aggregates. This is reflected in a blue-shifted triplet state and the corresponding feature in Faraday

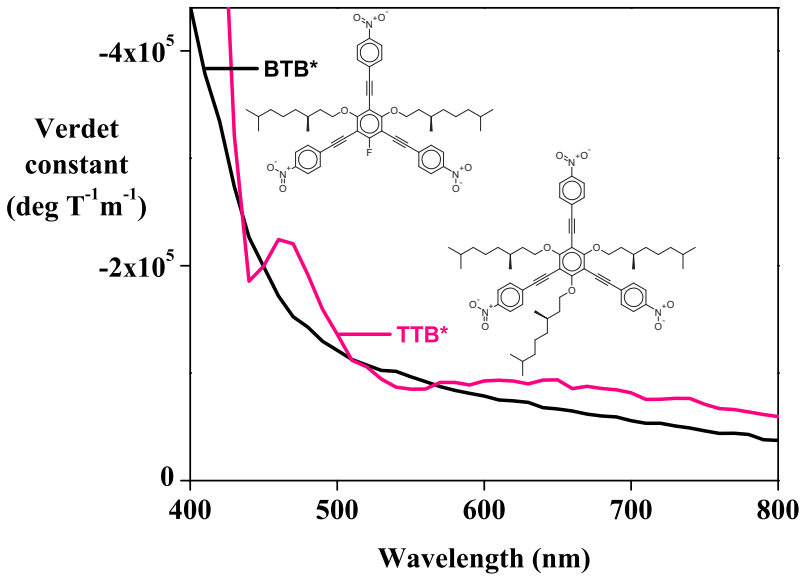

Figure 4.4: The feature in Faraday rotation in thin films of TTB* is blue-shifted and narrower than in thin films of TTB (fig. 4.1) because of the bulkiness of the branched alkyl chains in TTB*. Thin films of BTB*, however, show no separate feature in the Faraday rotation spectrum despite the presence of calculated triplet excitations around 510 nm. The corresponding band is likely hidden in the dispersion because of strongly absorbing singlet states.

rotation.[197] TTB* forms a chiral nematic discotic phase between 66 °C to 99 °C as a consequence of the homochiral nature of the three alkoxy chains. For BTB*, no separate feature in the Faraday rotation spectrum was detected (fig. 4.4). The calculations performed for a model of BTB* (see fig. 4.5) reveal, however, the presence of triplet excitations around 510 nm. Taking into account the spectral blue shift observed in the calculation for BTB* compared to TTB (which is expected to be even more pronounced when considering branched hydrocarbon chains in the molecule, based on the discussion above), it seems possible that in this case the feature in the Faraday rotation spectrum assigned to resonance with a triplet state is simply hidden in the resonant enhancement by strongly absorbing states. Consequently, one broad band in Faraday rotation spectrum is observed here.

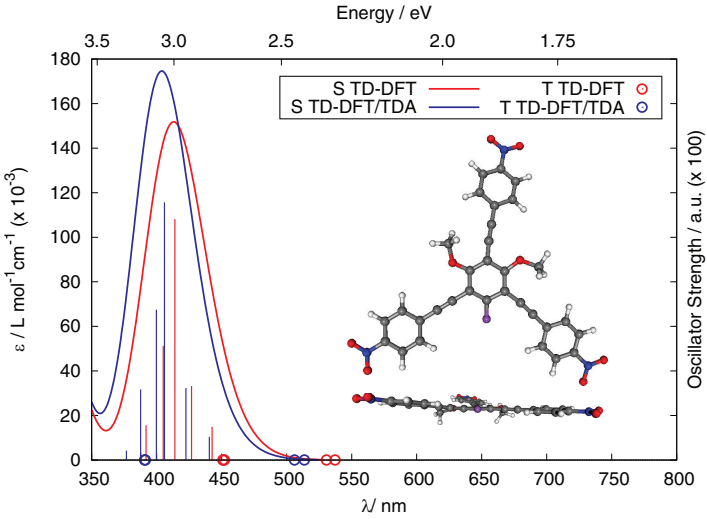

Figure 4.5: Calculated absorption spectrum for BTB* model molecule with indication of triplet excitations. TD-DFT B3LYP/TZVP computations applying RPA (red) or TDA (blue).

The liquid crystal nature of the molecule leads us to investigate the effect of temperature on the Faraday rotation spectrum (fig. 4.6). Under 60 °C TTB is crystalline, and it is columnar hexagonal from 60 °C to 68.5 °C. It displays a discotic nematic mesophase from 68.5 °C to 112 °C, from which temperature on it is present as an isotropic liquid.[182] The feature in Faraday rotation is present for the crystalline phase. In the discotic nematic phase the feature shifts to the blue, and finally the band in Faraday rotation is no longer visible in the isotropic liquid phase. This shift from crystalline to isotropic liquid is accompanied by a change in conformation and conformational freedom. In the crystalline phase the molecule is present in a fairly rigid, propeller geometry.[198] The disappearance of the Faraday rotation band in the isotropic liquid goes along with the complete loss of this conformational refinement for both TTB and TTB*. Consistent with this, a diluted solution in dichloromethane does not display a band in the Faraday rotation.

4.5 Conclusion

Materials with high Verdet constants and low absorption in the spectral region of interest are particularly interesting for a wide variety of applications of

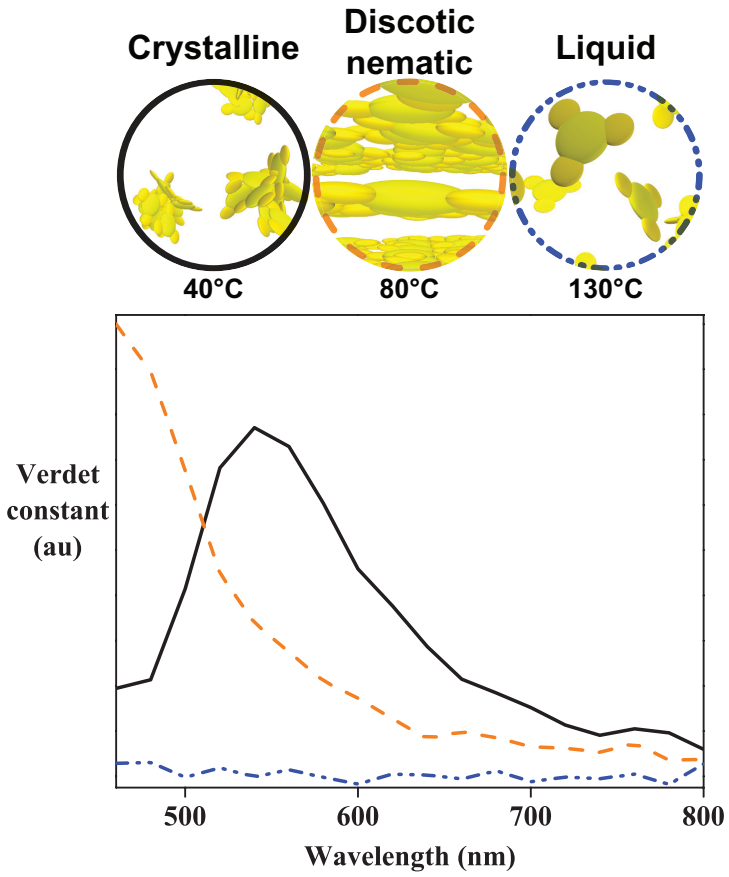

Figure 4.6: The Faraday rotation spectrum of TTB changes upon heating. The phase change from crystalline (full black) over discotic nematic (striped orange) to an isotropic liquid (dotted blue) is accompanied by a change in conformation and conformational flexibility. Correspondingly, the feature in Faraday rotation is no longer visible in the isotropic liquid phase.

Faraday rotation. In search of these properties, we have characterized the Verdet constant of an unexplored class of organic molecules. A Verdet constant of almost $2.5 \times 10^5 \circ \mathrm{T}^{-1}\,\mathrm{m}^{-1}$ is found with no associated absorption, 3 orders of magnitude larger than the largest known for an organic molecule in a region without spectral features. On the basis of the available data, the enormous Faraday rotation is potentially caused by a combination of intense low-energy

singlet excitations close to 520 nm and further resonant enhancement by a triplet excitation that is calculated to be right in the relevant wavelength window. While the transition is formally spin-forbidden, due to some degree of spin-orbit coupling, it may provide a mechanism for enhancing the Faraday rotation. We plan to address the cause of the strong Faraday rotation around 520 nm in more detail in a follow-up study. We are able to switch the Faraday rotation by changing the particular phase of the molecule. These results demonstrate a new class of Faraday rotating materials with great potential to replace current materials and increase the sensitivity in applications. The inherent flexibility in the synthesis, aggregation state and concentration of this class of molecules opens a new field of research in Faraday rotation.

Chapter 5

Magneto-optical harmonic susceptometry of superparamagnetic materials

Despite the promise of organic materials for future magneto-optical applications, there are still many unexplored promising inorganic materials as well. For this reason, we turned the focus of our research on understanding the influence of magnetic fields on light–matter interaction to superparamagnetic materials. These materials show great promise in applications, and we investigated the effect of their nonlinear behavior as a function of the magnetic field on AC Faraday measurements. We developed a technique that allows magnetic identification and characterization of superparamagnetic materials. This chapter is an article published in Applied Physics Letters in 2013, adapted to form for this dissertation. The supporting information can be found in appendix D and contains explicit derivations for the first and third harmonic, further fits of the 9th to 13th harmonic, an example of overfitting, and a VSM curve with Langevin fit of the used nanoparticles. W. Brullot performed the VSM measurements and D. Slavov supplied the laser diode used in the measurements.

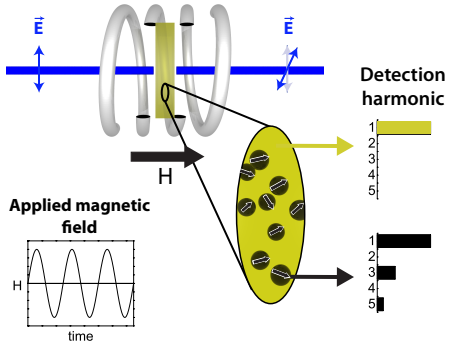

Magneto-optical harmonic susceptometry of superparamagnetic materials
Applied Physics Letters (2013), 102 (16), 161903
S. Vandendriessche, W. Brullot, D. Slavov, V. K. Valev and T. Verbiest

5.1 Abstract

We describe a technique to optically characterize superparamagnetism. Faraday rotation measurements are performed on a superparamagnetic nanocomposite using small alternating current magnetic fields. The superparamagnetism of the iron oxide nanoparticles causes signals at the uneven harmonics of the magnetic field frequency. These signals provide information on the magnetic moment of the superparamagnetic nanoparticles. Dia- and paramagnetism do not cause signals at higher harmonics, resulting in a high sensitivity to superparamagnetism, even in samples with large dia- or paramagnetic contributions. This technique provides a rapid, economical method to characterize superparamagnetism in composite samples not easily accessible by other techniques.

5.2 Introduction

Reducing the size of magnetic particles to the nanometer range causes new effects to occur that do not exist in bulk materials.[42] An important effect is superparamagnetism, which occurs when magnetic nanoparticles are so small that they can only support a single magnetic domain.[43] Under this critical radius, the nanoparticles can be described as having a single giant magnetic spin.[199] The critical radius depends on the type of material and typically ranges from nanometers to hundreds of nanometers. For magnetite nanoparticles it is approximately 20 nm.[200] Under this size, thermal energy is sufficient to relax the magnetization of the nanoparticles in the absence of an externally applied magnetic field on a timescale smaller than that of the experiment.[201] Shape and surface anisotropy present in the nanoparticles generally causes a uniaxial anisotropy, described by a single anisotropy energy density parameter K.[202] In the absence of an externally applied magnetic field, the particle magnetization lays along this anisotropy axis. Application of an external magnetic field initially causes the magnetization to favor one direction along the easy axis, causing a sharp increase in net magnetization of the nanoparticle sample. Higher applied magnetic fields cause the magnetization to rotate away from the anisotropy axis and towards the applied magnetic field direction.[203] This behavior can be described by the Langevin equation, and the size of the anisotropy for magnetic nanoparticles is typically such that magnetic saturation occurs at fields under 1 tesla.

Superparamagnetism has interesting applications in a wide variety of fields, including biomedicine,[202] bio-imaging,[204] hyperthermia,[205] magnetic fluids,[45] magnetic separation,[44] magnetic data storage[206] and many others. Characterization of the magnetic moment m of a superparamagnetic material is

crucial for these applications. This determines amongst others the contrast of the MRI images and the effectiveness of the hyperthermia.[204] It is also important for magnetic data storage purposes,[204] and can be used for nanoparticle size determination.[207]

VSM[208] and SQUID[209] are techniques frequently used to determine hysteresis, magnetic moment, saturation magnetization and blocking temperatures in superparamagnetic materials.[210] Alternatively, magnetization-induced second harmonic generation[76, 110, 211] is powerful for probing magnetic interfaces, and Faraday rotation can also be used to determine magnetic parameters.[135, 212] However, these techniques measure the total magnetic response of the probed region of the sample, and a large dia- or paramagnetic response can make the detection of a small superparamagnetic contribution difficult and time-consuming.

Nanocomposites, composite materials where at least one constituent has a size on the order of nanometers, have become important materials with many current and future applications,[213] such as in batteries,[214] antibacterial materials,[215] biochemistry,[39] magnetic-field controlled electrical devices[216] and many others. Nanocomposite material properties not only depend on the properties of their constituent materials, but also strongly depend on their morphology, dispersion and interfacial characteristics of the constituents.[39, 213–217] The increase in research on nanoscale materials has been driven by the ability to characterize these materials.[218] In order to further advance the field, new characterization techniques are necessary that are accessible to many researchers.

The advantages of superparamagnetic nanoparticles in imaging have previously been demonstrated.[219] In order to improve imaging contrast, it has already been demonstrated that it is possible to perform detection at higher harmonics of the frequency of the applied magnetic field.[220, 221] However, the precise relationship between the superparamagnetism of the material and the observed nonlinearities has not yet been derived.

The underlying principle of our technique (depicted in fig. 5.1) relies on the nonlinear response of a superparamagnetic material to an externally applied sinusoidal magnetic field. The direction and amplitude of an externally applied magnetic field, generated by a solenoid, are modulated by an alternating current. Under the influence of this modulation, light that propagates along the direction of the magnetic field has its direction of polarization rotated, due to the Faraday effect. This rotation of polarization is detected by a lock-in amplifier. At the applied magnetic field strengths, maximally 18 mT, dia- and paramagnetic materials can be considered to have a linear behavior as a function of the applied magnetic field strength. As such, they only cause a signal at the fundamental

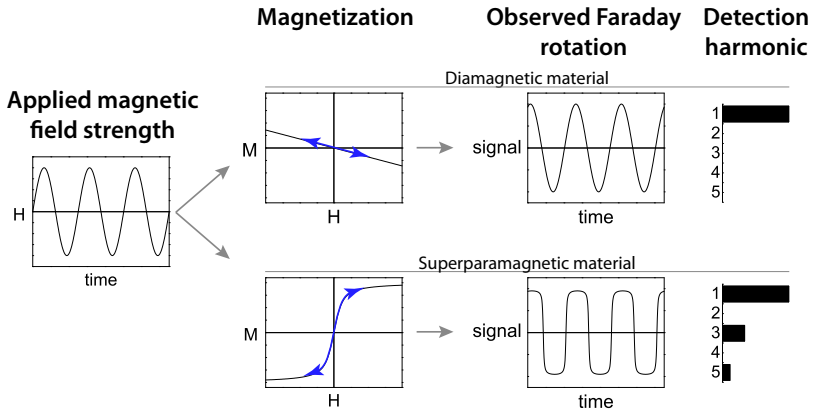

Figure 5.1: The direction and amplitude of an externally applied magnetic field, generated by a solenoid, are modulated sinusoidally. At the applied magnetic field strengths, dia- and paramagnetic materials can be considered to have a linear Faraday rotation as a function of the applied magnetic field strength, while superparamagnetic materials show a Langevin equation-dependence on the applied magnetic field strength. This can be observed in the the uneven higher harmonics, where the signal is solely attributable to superparamagnetism.

frequency of the modulated magnetic field. Over the same applied magnetic field strength range, superparamagnetic materials show clear deviation from linearity due to their Langevin-dependence on the applied magnetic field strength. This deviation can be observed in the uneven higher harmonics of the modulated magnetic field, where the signal is solely attributable to superparamagnetism. This allows analysis of complex samples with very small superparamagnetic contributions. Furthermore, the size and magnetic field strength dependence of the signal at each harmonic can be correlated to the superparamagnetic properties of the material. The proposed technique for the characterization of magnetic moment in superparamagnetic materials is rapid, economical and easily adaptable to many sample types.

5.3 Experimental details

Superperamagnetic iron oxide nanoparticles were synthesized using forced hydrolysis in polyol.[45] Briefly, a round-bottom flask with 37.5 mL of diethylene glycol and 25 mL of octylamine was heated to 150 °C while stirring. Separately, 2.4 g of anhydrous $FeCl_3$ was dissolved in a beaker with 3 mL of water and

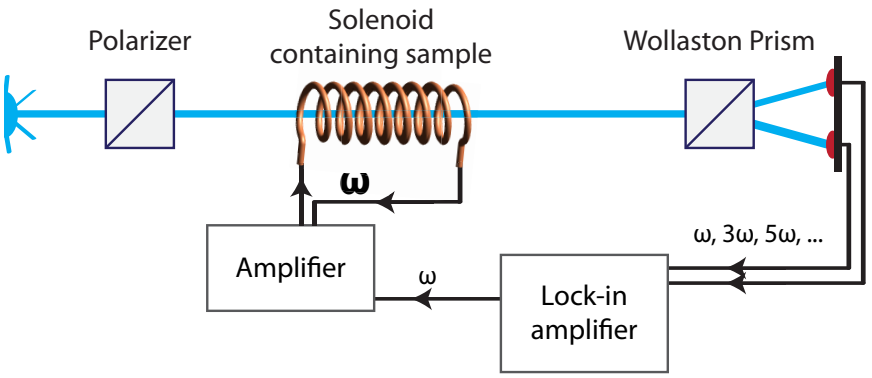

Figure 5.2: In the experimental setup, a 405 nm laser diode beam is linearly polarized and then passes through a solenoid. The beam is then split into orthogonal polarizations by a Wollaston prism at 45 degrees and is detected by photodiodes. A lock-in amplifier powers the solenoid via an amplifier at 857 Hz, producing a magnetic field in the solenoid that varies sinusoidally as a function of time.

10 mL of diethylene glycol. This mixture was added all at once to the round-bottom flask, which was then refluxed at 180 °C for 24 hours. The resulting mixture was magnetically filtered and washed three times with acetone. After drying in a vacuum oven, a black powder of superparamagnetic nanoparticles was obtained. In order to avoid any effects of physical orientation of the superparamagnetic nanoparticles on the measurement,[222] polymer nanocomposites were synthesized with these nanoparticles. The nanoparticles were dispersed in chloroform with PMMA, typically at 10 wt% to 15 wt%, and sonicated for two hours. Subsequently they were spincoated at 2000 rpm for 20 seconds on 1 mm thick BK7 glass slides, resulting in films of 1 µm to 2 µm. The resulting samples were optically isotropic. VSM measurements of a powder of the nanoparticles were performed at 300 K on an unmodified VSM Maglab setup (Oxford Instruments) (fig. D.3).

In the experimental setup used to detect Faraday rotation in transmission (fig. 5.2), a laser diode generates continuous wave 405 nm light, which is then linearly polarized by a GL10 Glan-Laser polarizer. This linearly polarized beam passes through a solenoid containing the sample. At the sample the beam is approximately 1 mm in diameter, at approximately 40 mW. The solenoid containing the sample is driven by a Europower EP2500 amplifier, which receives a reference sine wave at 857 Hz. The resulting sinusoidal magnetic field strength inside the solenoid causes Faraday rotation in the sample. A Wollaston prism

positioned at 45 degrees splits the light coming out of the solenoid into two beams of orthogonal polarization. Two photodiodes detect these two beams, and the resulting electronic signals are processed by a lock-in amplifier (SR830). This lock-in amplifier operates in A-B mode, subtracting the signal from the two photodiodes from each other. Measurements were performed by discretely varying the magnetic field strength and measuring the locked voltage at each harmonic for each magnetic field strength.

5.4 Theoretical derivation

Faraday rotation can be described by

$$\theta = VBd \tag{5.1}$$

where θ is the Faraday rotation, V is the Verdet constant, B is the magnetic field in the direction of the propagation of light and d is the distance traveled through the magnetic field. Rewriting the magnetic field yields (in SI units)

$$\theta = V\mu_0(H + M)d \tag{5.2}$$

with H the magnetic field strength, M the magnetization and μ_0 the magnetic permeability of vacuum. For dia- and paramagnetic materials the magnetization is linear as a function of the magnetic field strength, so we can write

$$\theta = V\mu_0(1 + \chi^{(1),mm})Hd \tag{5.3}$$

with $\chi^{(1),mm}$ the magnetic susceptibility. Using this linear relationship between Faraday rotation in a dia- or paramagnetic material and an applied magnetic field, it is possible to linearly correlate the light intensity on a photodiode to the Faraday rotation.[26]

For superparamagnetic materials, the magnetization is not a linear function of the magnetic field strength, but can be described by a Langevin function[43]

$$M = M_S L(C \cdot H) \tag{5.4}$$

where M_S is the saturation magnetization. We can now write

$$\theta = V\mu_0(H + M_S L(C \cdot H))d \tag{5.5}$$

The Langevin function can be written as a function of the magnetic field strength[43]

$$L(C \cdot H) = \coth(C \cdot H) - \frac{1}{C \cdot H} \tag{5.6}$$

where $C = m/(k_B T)$ with k_B the Boltzmann constant and m the magnetic moment. Because $1/(C \cdot H)$ is undefined at $H = 0$, we can not perform a Taylor expansion around this point. We can however expand $\coth(x)$ in a Laurent series around $x = 0$

$$\coth(x) = \frac{1}{x} + \sum_{n=1}^{\infty} \frac{2^{2n} B_{2n} x^{2n-1}}{(2n)!} \tag{5.7}$$

where B_{2n} is the $2n$th Bernoulli number. Filling this into the Langevin function, eq. (5.6), yields

$$L(C \cdot H) = \sum_{n=1}^{\infty} \frac{2^{2n} B_{2n} (C \cdot H)^{2n-1}}{(2n)!} \tag{5.8}$$

The applied magnetic field strength is sinusoidal in time

$$H = H_0 \sin(A) \tag{5.9}$$

where we write $A = \omega t + \varphi$ to lighten the notation. Filling into eq. (5.8) results in

$$L(C \cdot H) = \sum_{n=1}^{\infty} \frac{2^{2n} B_{2n} (C \cdot H_0)^{2n-1}}{(2n)!} \sin^{2n-1}(A) \tag{5.10}$$

Because $2n - 1$ is odd, we can expand $\sin^{(2n-1)}(A)$ via de Moivre's formula

$$\sin^{(2n-1)}(A) = \frac{1}{2^{2n-2}} \sum_{k=0}^{n-1} (-1)^{n-1-k} \binom{2n-1}{k} \sin((2n-1-2k)A) \tag{5.11}$$

where $\binom{a}{b}$ is the binomial coefficient. Filling eq. (5.11) into eq. (5.10) yields

$$\begin{aligned} L(C \cdot H) = \sum_{n=1}^{\infty} \Big[& \frac{4 * B_{2n} (C \cdot H_0)^{2n-1}}{(2n)!} \\ & \times \sum_{k=0}^{n-1} (-1)^{n-1-k} \binom{2n-1}{k} \sin((2n-1-2k)A) \Big] \end{aligned} \tag{5.12}$$

and finally we fill eq. (5.12) into eq. (5.5)

$$\theta = V\mu_0 \Bigg(H_0 \sin(A) + M_S \sum_{n=1}^{\infty} \Big[\frac{4 * B_{2n} (C \cdot H_0)^{2n-1}}{(2n)!} \times \sum_{k=0}^{n-1} (-1)^{n-1-k} \binom{2n-1}{k} \sin((2n-1-2k)A) \Big] \Bigg) d \tag{5.13}$$

We see that, in contrast to eq. (5.3) for dia- and paramagnetic materials, the observed Faraday rotation θ contains components at higher harmonics of the frequency of the magnetic field. Because $2n-1-2k$ is uneven, we see that there will only be uneven harmonics present. Using eq. (5.13), we can now determine what signal will be present at each harmonic for a given superparamagnetic sample. Explicit derivations for the first and the third harmonic can be found in appendix D. Neglecting nonlinearities at very low fields reduces eq. (5.13) to a linear relation between the signal at the fundamental frequency of the applied magnetic field and the amplitude of the applied magnetic field, allowing determination of the Verdet constant of the material.[25, 45, 135]

5.5 Experimental results

For the measured superparamagnetic nanocomposite, a clear signal was detected on the lock-in amplifier for all uneven harmonics until the 13th harmonic, while no signal was observed for any even harmonic. Purely dia- and paramagnetic samples only produced a measurable signal at the fundamental frequency. The signal for the superparamagnetic nanocomposite divided by the DC voltage on the photodiodes is plotted as a function of the magnetic field in fig. 5.3 for the first to the seventh harmonic.

Fitting the observed signal as a function of the applied magnetic field strength to eq. (5.13) yields a value for C, the constant in the Langevin equation (eq. (5.6)). When performing these fittings, care needs to be taken to avoid overfitting.[223] Using too many terms in the fit attributes too much importance to noise in the data, resulting in incorrect fits (fig. D.2). For our data, it was empirically determined that the optimal number of terms was four. The resulting fits are displayed in fig. 5.3, and the associated values for C are displayed in table 5.1.

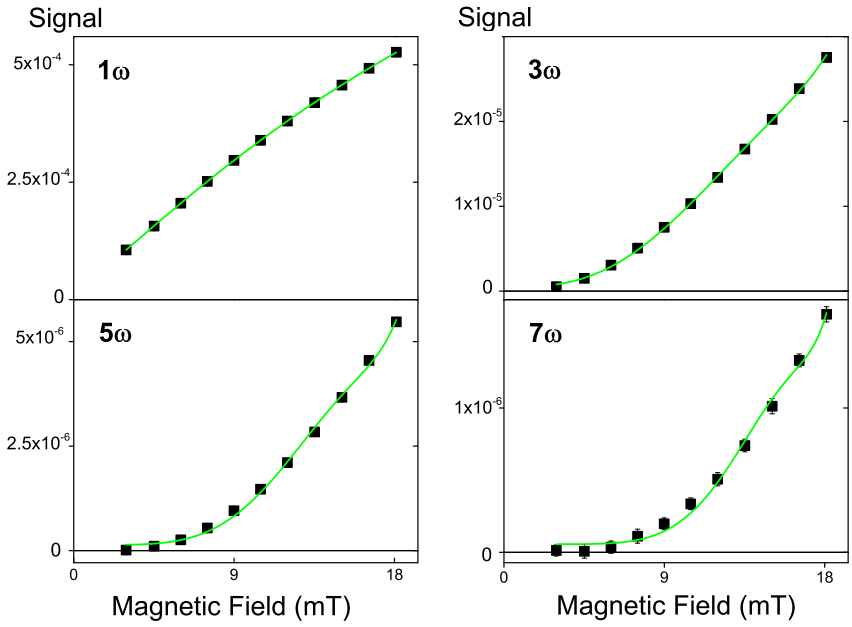

Figure 5.3: A clear non-linear dependence is seen in the signal of the superparamagnetic nanocomposite as a function of the magnetic field, with higher order harmonics displaying higher order nonlinearities in the magnetic field. Fitting is performed to equations derived from eq. (5.13), allowing for four magnetic field strength dependent terms per fit.

Table 5.1: Value of C for fits to eq. (5.13) for each measured harmonic of the superparamagnetic nanocomposite

Measured harmonic	C (T^{-1}) from fitting to eq. (5.13)
3	163.16 ± 13.29
5	153.30 ± 13.52
7	143.13 ± 12.49
9	132.90 ± 11.42
11	127.13 ± 10.73
13	119.18 ± 9.68

5.6 Discussion

These C values can be related to the magnetic properties of the material via $C = \mu/(k_B T)$;[43] this can be interpreted as a ratio of the magnetic moment to the thermal energy. We can now compare the measured C to that derived from VSM measurements performed on a powder of the nanoparticles from $-20\,\mathrm{mT}$ to $20\,\mathrm{mT}$, where $C = 177\,\mathrm{T}^{-1}$. This corresponds quite well to the values obtained from our characterization technique. However, this is larger than the values typically reported in literature for these nanoparticles, which, for this size of iron oxide nanoparticles, range from $25\,\mathrm{T}^{-1}$ to $45\,\mathrm{T}^{-1}$.[207] The reason for this discrepancy lies in the small range of the magnetic field strength measured. When the VSM hysteresis is acquired from $3\,\mathrm{T}$ to $-3\,\mathrm{T}$, we obtain $C = 40\,\mathrm{T}^{-1}$. As the range of magnetic field strength is decreased, the fit value for C increases. This dependence of C on the magnetic field strength range is due to the fact that the particles deviate from ideal Langevin behavior.

Our technique is more applicable to small magnetic field strengths than VSM measurements, which tend to be optimized for measurements at large magnetic field strengths. See fig. D.3 for an example of a VSM curve at a small magnetic field. Our technique on the other hand excels at smaller magnetic field strengths.

An important application of our technique is the observation of non-ideal superparamagnetic behavior. For ideal Langevin behavior, the C values for each harmonic in table 5.1 would be equal. From this single C value the magnetic moment of the nanoparticles can be calculated. However, the value of C differs for each harmonic. The deviations from the ideal values of C can be used to acquire information on the non-idealities present in the sample. Possible causes of non-idealities are the size distribution of the nanoparticles, inter-particle interactions or surface effects.[224] Our technique is well-suited to further analyze these non-idealities.

5.7 Conclusion

Superparamagnetism is an important effect in magnetic nanoparticles. While magnetism in materials can be characterized by a variety of techniques, characterizing superparamagnetism in thin film samples with a large dia- or paramagnetic contribution remains difficult. We have demonstrated an optical magnetization characterization uniquely sensitive to superparamagnetism.

For the investigated superparamagnetic iron oxide polymer nanocomposite, a clear signal was observed for all uneven harmonics until the 13th harmonic, while

no signal was observed for any even harmonic. Solely dia- and paramagnetic samples only produced a measurable signal at the fundamental frequency, with no signal at any higher harmonic. Our characterization technique is rapid and economical, and the resulting values provide information on the superparamagnetism present in the sample.

Chapter 6

Characterization of magnetization-induced second harmonic generation in iron oxide polymer nanocomposites

After focusing on the behavior of superparamagnetic materials in AC Faraday measurements, we turned our attention to their behavior in magnetization-induced second harmonic generation (MSHG) measurements. While MSHG has been used to study magnetism and magnetic interfaces, it had not yet been applied to characterize superparamagnetic nanocomposites. This chapter is an article published in Applied Optics in 2012, adapted to form for this dissertation.

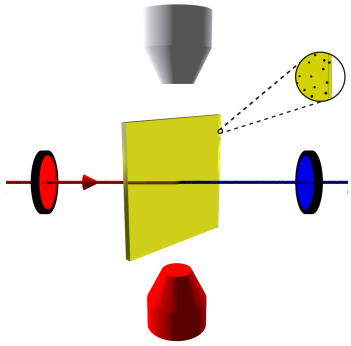

Characterization of magnetization-induced second harmonic generation in iron oxide polymer nanocomposites
Applied Optics (2012), 51 (2), 209–213
S. Vandendriessche, V. K. Valev and T. Verbiest

6.1 Abstract

We have measured the magnetization-induced second harmonic generation (MSHG) of a nanocomposite consisting of iron oxide nanoparticles in a polymer film. The existing theoretical framework is extended to include DC magnetic fields in order to characterize the MSHG signal and analyze the measurements. Additionally, magnetic hysteresis loops are measured for four principle polarizer-analyzer configurations, revealing the P_{IN}-P_{OUT} and S_{IN}-P_{OUT} polarizer-analyzer configurations to be sensitive to the transverse magnetic field. These results demonstrate the use of MSHG and the applied formalism as a tool to study magnetic nanoparticles and their magnetic properties.

6.2 Introduction

Magnetic nanoparticles are the subject of intense investigation in a wide range of disciplines including catalysis, analytical chemistry,[225] data storage,[226] biochemical research[227] and biomedical applications.[205] The magnetic properties of the nanoparticles play a key role in their applications and can be characterized by a variety of techniques such as vibrating sample magnetometer,[208] Mössbauer spectroscopy, and superconducting quantum interference device.[224] These techniques provide precise information on the magnetic properties of the nanoparticles but suffer from drawbacks such as high complexity and cost.

Optical second harmonic generation (SHG) is a nonlinear optical process with a large sensitivity to symmetry breaking and interfaces.[2] Due to this sensitivity and the ability to measure buried interfaces, SHG has been used extensively to study interfaces and nanomaterials of various types[11] such as semiconductors,[75] plasmonic metal nanoparticles[228] and organic materials.[115, 229]

The presence of a magnetic field does not change the symmetry dependency of SHG, but does break time reversal symmetry, allowing for an additional source of SHG: magnetization-induced second harmonic generation (MSHG).[102, 104, 230–232] This magnetic sensitivity allows the characterization of continuous[233] as well as nano-patterned magnetic interfaces and materials.[101]

Besides nano-patterned samples and magnetic films, a variety of magnetic nanoparticle films have been investigated by MSHG.[103, 234] These studies have been performed on samples made by techniques such as electron beam lithography, sputtering and vapor deposition. While these techniques allow

for a high degree of control, they can be expensive, time consuming and are not easily accessible for many researchers. Polymer nanocomposites are more accessible materials which allow for improved processability.[235] A wide variety of magnetic nanocomposites exist and there is currently extensive research on their properties and applications.[47]

Although diffuse and depolarized MSHG has been observed from chemically synthesized nanoparticles deposited on a glass substrate through solvent evaporation,[236] to our knowledge no characterization of the MSHG response of a magnetic polymer nanocomposite has been performed yet. In this paper we report the characterization and analysis of the MSHG response of an iron oxide nanoparticle polymer nanocomposite. These magnetic nanocomposites provide a model system to study the magnetic properties of nanoparticles. In combination with the high sensitivity of MSHG this knowledge offers the prospect of MSHG measurements in more complex samples containing magnetic nanoparticles.

6.3 Experiments

Iron oxide nanoparticles were synthesized by heating a round-bottom flask with 37.5 mL of diethyleneglycol and 25 mL of octylamine to 150 °C while stirring.[237] Separately, 2.4 g of anhydrous $FeCl_3$ was dissolved in a beaker with 10 mL of diethyleneglycol and 3.5 mL of water. This mixture was added to the round-bottom flask, which was subsequently refluxed at 180 °C for 24 hours. The synthesized nanoparticles were filtered on a homemade magnet, washed three times with acetone and dried in a vacuum oven. This resulted in iron oxide nanoparticles with a diameter of (7.63 ± 2.09) nm as determined by transmission electron microscopy.

The nanocomposite was synthesized by sonicating 38 mg of the iron oxide nanoparticles with 226 mg of poly(methyl methacrylate) (PMMA) with a nominal molecular mass of 38 000 g/mol in 2 mL of chloroform for one hour. This solution was spin coated on a glass plate at 1800 rpm for 15 seconds, resulting in a film of approximately 2.1 µm thick.

Second harmonic generation was measured using a Ti:sapphire laser operating at a wavelength of 800 nm, emitting approximately 100 fs pulses with a repetition rate of 82 MHz. The generated beam was polarized by a half-wave plate on a motorized rotation stage followed by a Glan-laser polarizer mounted on a separate motorized rotation stage. Subsequently the beam passed through a quarter-wave plate which was also mounted on a motorized rotation stage. After being filtered by a RG 650 filter to exclude 400 nm light, the beam of

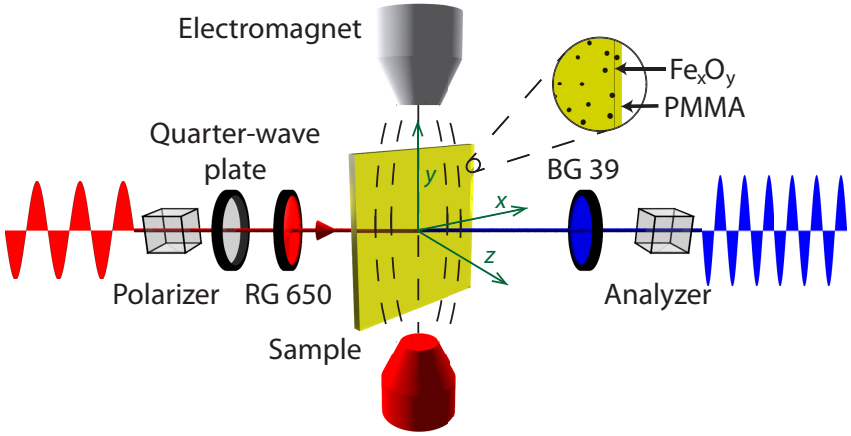

Figure 6.1: Experimental setup for magnetization-induced second harmonic generation (MSHG) measurements of an iron oxide nanocomposite. A transverse magnetic field is applied and the sample is measured at 45 degrees in transmission.

approximately 100 mW intensity was focused (focal length 10 cm) on the sample at an incidence angle of 45 degrees. The sample was mounted in a GMW 3470 dipole electromagnet with the magnetic field in a transverse configuration. The transmitted beam was filtered by two BG 39 filters to exclude 800 nm light, allowing the SH light to pass through an analyzer mounted on a motorized rotation stage. A photomultiplier tube cooled to −20 °C collected the second harmonic light, and after pre-amplification an SR400 gated photon counter was used to process signal.

6.4 Results and discussion

Within the electric dipole approximation, the optical polarization induced at the second harmonic frequency can be written as[2]

$$P_i(2\omega) = \sum_{j,k} \chi_{ijk}^{(2),eee} E_j(\omega) E_k(\omega) \tag{6.1}$$

Where i, j and k are the cartesian axes, E_i is the electric field of the incident light and $\chi^{(2),eee}$ is the second order susceptibility, a material-specific second rank tensor consisting of 27 components. The presence of a magnetic field allows

for additional sources of SHG[231]

$$P_i(2\omega) = \sum_{j,k} \chi_{ijk}^{(2),eee} E_j(\omega) E_k(\omega) + \sum_{j,k,l} \chi_{ijkl}^{(3),eeem} E_j(\omega) E_k(\omega) M_l \tag{6.2}$$

where M_l is the magnetization in the l direction and $\chi^{(3),eeem}$ is the third order magnetic susceptibility, a material-specific third rank tensor consisting of 81 components.

The MSHG from a 14.4 wt% iron oxide nanoparticle PMMA nanocomposite of approximately 2.1 µm thick was measured in transmission at an incidence angle of 45 degrees in a transverse magnetic field, as depicted in fig. 6.1.

We analyzed the dependence of the MSHG on the polarization of the incident light and on the sign of the magnetic field (fig. 6.2).

A clear influence of the sign of the transverse magnetic field on the intensity of the SHG signal is seen in all four principle polarizer-analyzer configurations. Regardless of symmetry and experimental geometry, it is always possible to describe the intensity of the (M)SHG with eq. (6.3)[2]

$$I(2\omega)_{s,p} \sim [f_{s,p} E_p^2(\omega) + g_{s,p} E_s^2(\omega) + h_{s,p} E_p(\omega) E_s(\omega)]^2 \tag{6.3}$$

Where E_s, E_p are respectively the s- and p-component of the electric field of the incident light and $I(2\omega)_{s,p}$ is the intensity of respectively the s- and p-component of the SHG.

Based on symmetry considerations within the electric dipole approximation for an isotropic sample with interfaces with C_v^∞ symmetry, the theoretical expressions for the f, g and h parameters of an in-plane isotropic sample in transmission at 45 degrees can be derived to be[2]

$$f_s = 0 \tag{6.4}$$

$$g_s = 0 \tag{6.5}$$

$$h_s = \sqrt{2}(\chi_{yyz}^{(2),eee} + \chi_{yxyy}^{(3),eeem} M_y) \tag{6.6}$$

$$f_p = \frac{(\chi_{zxx}^{(2),eee} + \chi_{zzz}^{(2),eee} + 2\chi_{xxz}^{(2),eee} + (\chi_{xxxy}^{(3),eeem} + \chi_{xzzy}^{(3),eeem} + 2\chi_{zxzy}^{(3),eeem}) M_y)}{(\sqrt{2})^3} \tag{6.7}$$

$$g_p = \frac{(\chi_{zxx}^{(2),eee} + \chi_{xyyy}^{(3),eeem} M_y)}{\sqrt{2}} \tag{6.8}$$

$$h_p = 0 \tag{6.9}$$

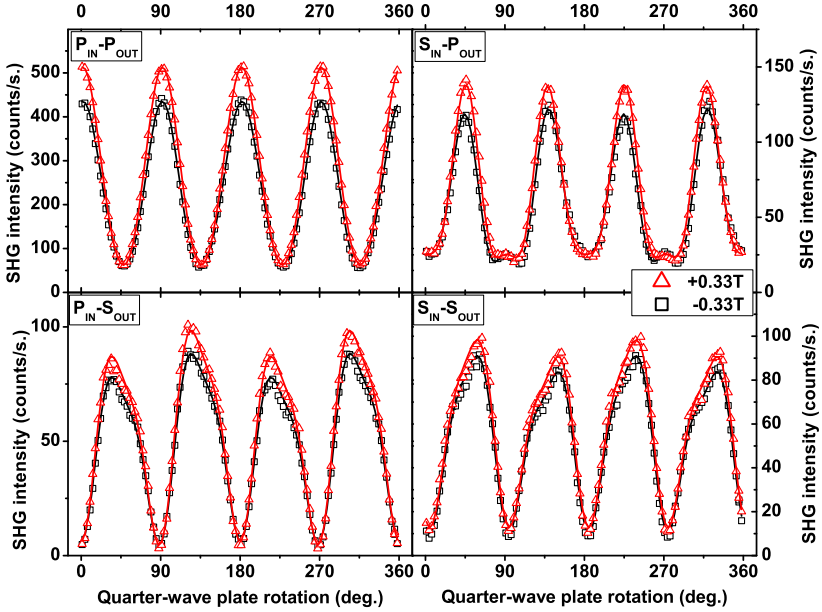

Figure 6.2: Magnetic contrast of the SHG intensity for four principle polarizer-analyzer configurations. Measurements performed as a function of the input polarization by rotating a quarter-wave plate placed before the sample. Solid lines are the fits according to eq. (6.3) and the fitting parameters are displayed in table 6.1. A clear influence of the sign of the magnetic field on the intensity of the SHG signal is seen in all four principle polarizer-analyzer configurations.

Note that we have omitted the linear optical coefficients for simplicity, though these can be included in a straightforward fashion.[238] Equation (6.3) can be adapted to allow for a rotating wave plate in front of the sample.[239] Our experimental data was fitted to this equation. The fitting parameters for the fit in fig. 6.2 are displayed in table 6.1. Within experimental precision the fitting parameters f_p, g_p and h_s are significantly influenced by the transverse magnetic field, which corresponds well to the theoretical predications from eqs. (6.4) to (6.9). The largest magnetic contribution originates from the $(\chi^{(3),eeem}_{xxxy} + \chi^{(3),eeem}_{xzzy} + 2\chi^{(3),eeem}_{zxzy})$ components of the second order magneto-susceptibility.

The small deviation of the components from those predicted by the model is attributable either to bulk contributions not included in the model, or to

Table 6.1: Fitting components of the fit of eq. (6.3) to the data in fig. 6.2. Within experimental precision h_s, f_p and g_p are significantly influenced by the transverse magnetic field, corresponding well to theoretical expressions eqs. (6.4) to (6.9)

	$+0.33\,\mathrm{T}$	$-0.33\,\mathrm{T}$
f_s	$13.22 + 4.20i \pm (0.37 + 0.27i)$	$11.99 + 3.92i \pm (0.36 + 0.26i)$
g_s	$14.00 - 0.30i \pm (0.39 + 0.37i)$	$12.56 - 0.54i \pm (0.36 + 0.35i)$
h_s	140.77 ± 0.50	132.90 ± 0.48
f_p	$-6.82 + 186.59i \pm (2.25 + 0.43i)$	$-6.46 + 170.27i \pm (2.80 + 0.49i)$
g_p	$-7.68 + 22.94i \pm (0.29 + 1.62i)$	$-13.38 + 22.66i \pm (0.37 + 1.99i)$
h_p	0.38 ± 0.18	-1.19 ± 0.23

anisotropy induced by sample preparation.[237] In the case of samples with a known anisotropy it is possible to derive eqs. (6.4) to (6.9) for the appropriate symmetry, yielding the tensor component values for the directional (magnetic) anisotropy present in these samples. Here the possible sample preparation induced anisotropy is assumed to be small, thus the deviation from 0 for the f_s and g_s components is primarily attributable to bulk contributions.

Subsequently the polarization of the MSHG signal was verified by rotating the analyzer for both *p*- and *s*-polarized incident light (P_{IN} and S_{IN}) (fig. 6.3). For the P_{IN} configuration, the rotation of the analyzer results in a transition of the measurement of the parameter f_p to the parameter f_s. A large magnetic contrast in intensity but no clear polarization rotation is observed, in agreement with the large magnetic contrast for the f_p parameter and a smaller magnetic contrast and absolute value of the f_s parameter. For the S_{IN} configuration, the analyzer rotation results in a transition of the measurement of the parameter g_p to the parameter g_s. A smaller magnetic contrast in intensity is observed and there is a small rotation of polarization due to the magnetic field. This corresponds to a small interference between the bulk g_s component and the magnetic g_p component, and the small size of the rotation illustrates the significance of the magnetic contribution.

MSHG hysteresis loops were measured for four principle polarizer-analyzer configurations (fig. 6.4). These loops can accurately represent the magnetization reversal process for systems where the magnetic contrast is small in comparison with the overall SHG response, as is the case here (fig. 6.2).[240] In the P_{IN}-P_{OUT} and S_{IN}-P_{OUT} configurations the magnetic contrast of respectively the f_p and the g_p parameter is measured. The resulting magnetic contrast corresponds well with the obtained fitting parameters, showing the largest contribution to

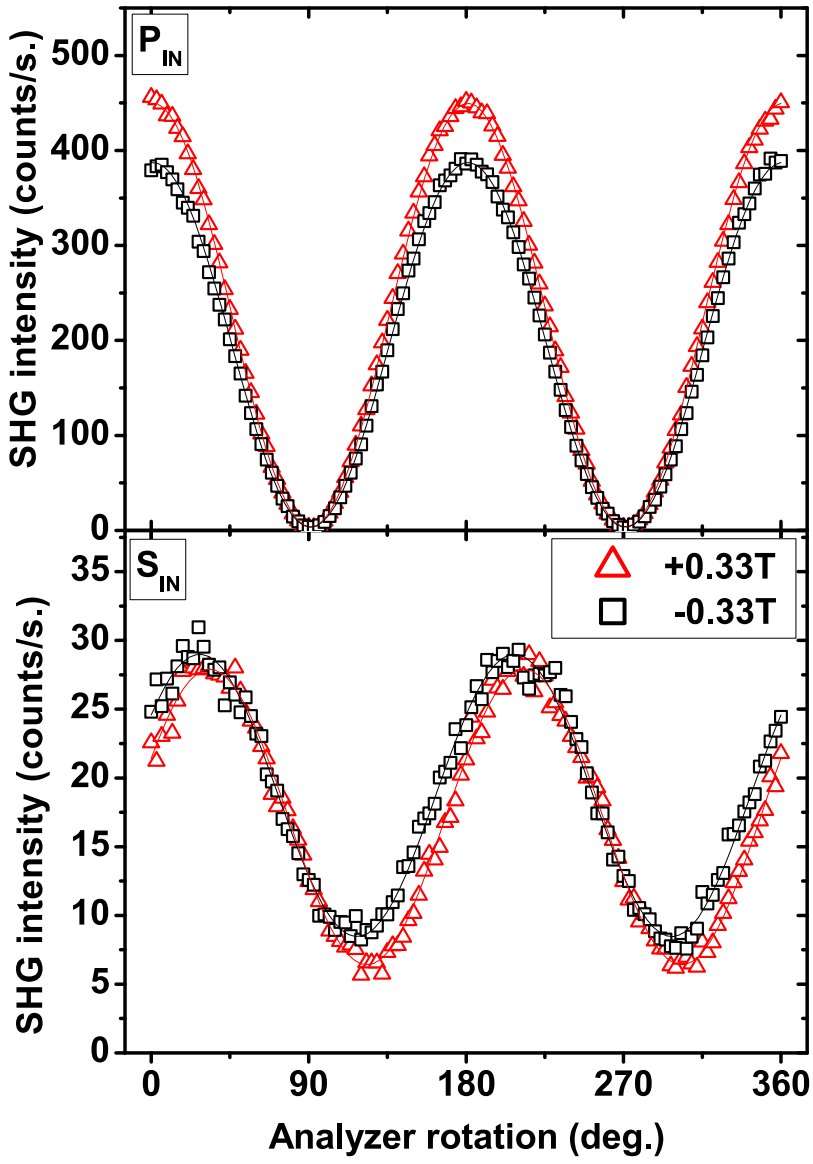

Figure 6.3: Polarization of the MSHG, measured by rotation of the analyzer, where 0 degrees analyzer rotation corresponds to P_{OUT}. The SHG generated by P_{IN} polarized light mainly varies in amplitude upon reversal of the sign of the magnetic field, while the SHG generated by S_{IN} polarized light slightly rotates polarization upon reversal of the magnetic field.

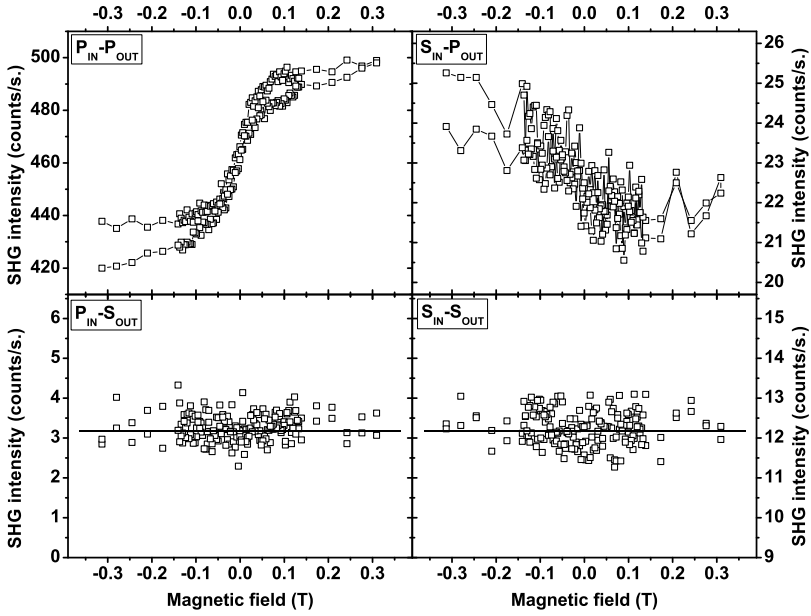

Figure 6.4: MSHG hysteresis loops for four principle polarizer-analyzer configurations. P_{IN}-P_{OUT} and S_{IN}-P_{OUT} SHG is sensitive to the transverse magnetic field, with relative changes in SHG of more than 10 %. P_{IN}-S_{OUT} and S_{IN}-S_{OUT} show no magnetic contrast.

the magnetic susceptibility to be from the $(\chi^{(3),eeem}_{xxxy} + \chi^{(3),eeem}_{xzzy} + 2\chi^{(3),eeem}_{zxzy})$ term. In the P_{IN}-S_{OUT} and S_{IN}-S_{OUT} configurations the magnetic contrast of respectively the f_s and the g_s term is measured. The lack of magnetic contrast indicates that, consistent with the fitting parameters, the f_s and g_s term are not influenced by a magnetic field within experimental precision.

6.5 Conclusions

The MSHG measurements are consistent with each other and the theoretical model provides a good framework to analyze the MSHG of nanocomposites. The obtained fitting parameters yield more insight into the nonlinear susceptibilities of the nanocomposite and its nanoparticles than the magnetic contrast which is represented by a single number. Additionally, the theoretical parameters can

be derived for an arbitrary symmetry, making it possible to identify directional (magnetic) anisotropy in more complex samples. To determine the components of the (magnetic) nonlinear susceptibilities, only a single measurement at one incidence angle in either transmission or reflection is required. A further advantage is that characterization is possible with a wave plate of any retardation besides a half-wave plate, not only a quarter-wave plate.[239]

These data show magnetic nanocomposites to be promising materials for MSHG investigation. Further nanocomposite MSHG measurements will allow a better understanding of the influence of magnetic nanoparticle parameters, e.g. size, on their nonlinear susceptibilities. This knowledge can support future applications for magnetic nanoparticles such as allowing the identification of magnetic nanoparticles in SHG microscopy images.

In conclusion, we have measured and characterized the MSHG response of an iron oxide nanoparticle polymer nanocomposite. Experimental data show a large magnetic contrast of SHG in a transverse magnetic field. Coupling this data to a theoretical framework allows the measurements to be correlated to the nonlinear (magnetic) polarizabilities of the nanocomposite. This theoretical understanding demonstrates the usefulness of MSHG to characterize the magnetic properties of nanoparticles.

Chapter 7

Conclusions and perspectives

Despite over a century of magneto-optical research, much of the influence of magnetic fields on light–matter interaction remains to be investigated. We sought to contribute to this understanding from the viewpoint of nonlinear optics. We first introduced the framework necessary to describe the influence of magnetic fields on light–matter interactions in chapter 1.

In chapter 2 we presented an experimental setup to measure magneto-optical activity. By combining a PEM with the correct sequence of polarizer and analyzer, we can simultaneously detect CB and CD. A DC magnet in the setup allows us to discretely vary the applied magnetic field strength, and measure Faraday rotation and MCD. The design of the system is deceptively simple, but the experimental implementation is less straightforward than it might appear. Despite the existence of similar experimental setups, a thorough analysis of the effect of using a real PEM as opposed to an idealized PEM had not been performed. This analysis is necessary in order to correctly interpret the values measured in the setup, and for this reason we used Mueller calculus to analyze what happens to light in the setup. We showed that it is not possible to measure CB and CD completely separately. The mixing of these two signals in the setup derives from static strain present in the PEM, which is too large in our setup to be approximated to be zero. Using such a setup is a trade-off compared to specialized CB or CD measurement setups. Simple AC Faraday measurement systems using AC magnetic fields measure CB and are not influenced by the presence of CD, but for this reason also do not provide information on the CD in the sample. CD measurement systems on the other hand use a very similar sequence of components to our setup, but omit the last analyzer. This renders the measured CD signal insensitive to CB, but provides no information

on the CB in the signal. We proved that we can take the mixing that does occur in our experimental setup into account through calibration and correct data interpretation. The slight loss in sensitivity and precision is sufficiently compensated by the wealth of extra data.

Future work should focus on incorporating a second PEM in the setup; if correctly configured and interpreted, a double-PEM setup provides more complete information on the Mueller matrix of the sample under study.

Equipped with this magneto-optical setup, we focused on Faraday rotation in organic materials in chapter 3. Organic materials show many advantages over inorganic materials in terms of applications, such as their high processability and great flexibility in synthesis. Replacing the existing inorganic materials with organic materials would be both economically and fundamentally interesting. The Verdet constants of current organic materials are too low to be useful, so it is necessary to search for better materials. In order to help direct this research, we measured the Faraday rotation of a series of saturated organic liquids in the visible wavelength region. We also calculated the corresponding Verdet constants. Measurement and calculation corresponded well, and both were fit to a dispersion formula for Verdet constants off-resonance, allowing us to quantify the Verdet constant over a broad wavelength region. We observed trends over alkane and alcohol carbon backbone length, and a linear correlation to both the molecular polarizability and the diamagnetic susceptibility. With the aim of generalizing these results, we applied a molecular connectivity index model based on our measurements in order to predict the Verdet constant for arbitrary aliphatic compounds. Combined with the density of the liquid, it allows the prediction of the Faraday rotation of arbitrary aliphatic liquids at a chosen wavelength. The connectivity index reveals that large fragments in the molecules yield important contributions to the Faraday rotation which cannot be predicted based solely on the number of constituent atoms.

Future work can focus on alleviating the limitation in our calculations that the calculations break down near resonance. This can be done by incorporating damping in the response functions used for the calculations. This is currently feasible but requires modifications to the computational code that are not yet implemented.

Large Faraday rotation has previously been reported in conjugated organic molecules, albeit with reproducibility issues. This lead us to turn our attention to the Faraday rotation in a certain class of conjugated molecules in chapter 4. These molecules have the advantage of being liquid crystalline, providing flexibility in the choice of phase by varying the temperature. It is well known that Faraday rotation is enhanced due to resonances; Faraday rotation increases in many absorption bands. Off resonance, Faraday rotation typically follows

the λ^{-2} dependence in the visible wavelength region, observed in the aliphatic liquids analyzed in chapter 3. To our surprise, we found a feature in the Faraday rotation of these liquid crystals. More strikingly, the Faraday rotation was very large ($2.5 \times 10^5 \circ \mathrm{T}^{-1}\,\mathrm{m}^{-1}$ around 520 nm) and occurred in a region with almost no absorbance.
Our search for an explanation led us to the hypothesis that the cause of the feature was indeed resonance enhancement, but not by a singlet transition. A triplet transition is formally spin-forbidden, meaning it does not appear in the absorbance spectrum, but it could nonetheless resonantly enhance the Faraday rotation. This hypothesis was strengthened by the presence of triplet transitions in this wavelength region in similar molecules. To confirm that these triplet transitions were also present in our molecule, we invoked the computational expertise of Monika Srebro and Jochen Autschbach. Their TD-DFT calculations confirmed the presence of these triplet transitions near the feature in Faraday rotation. The position of the triplet transitions is strongly dependent on the molecular conformation. This is consistent with the Faraday rotation we measured in different liquid crystalline phases by varying the temperature. Finally, we also showed that the feature is absent in solution, and is present but blue-shifted in a similar chiral molecule with slightly different stacking.
While our hypothesis is consistent with current observations, we can not exclude certain other explanations. Intermolecular stacking and interactions are an important alternative explanation, and more research is necessary in order to test both of these hypotheses.

These results pave the way for two important future research lines. Firstly, it would be interesting to calculate the influence of triplets on the Verdet constant. While it has been theoretically shown how triplet states can influence the Verdet constant, this has not yet been implemented in computational code. This modification is far more profound than simply introducing damping for instance. Implementing the many different paths and terms through which triplets can influence the Verdet constant is a very promising research subject in itself, which could later be complemented by comparison to our experiments.
Alternatively, further research could investigate the effect of confirmation on this feature in Faraday rotation. Among the multitude of ways to tackle this, the most straightforward path would be to fix the conformation by synthesizing analogues. Despite the apparent ease in designing these analogues there are a myriad of factors that complicate this research. Crucially, the phase transition temperatures, and by extension the phase present at room temperature, change upon each variation in molecular structure, impeding direct conformation–conformation comparison of different analogues measured at the same temperature.

Organic materials are promising materials for future magneto-optical applications; however many promising inorganic materials remain unexplored. An important class of these materials which has gained popularity in recent years are superparamagnetic nanoparticles. The availability of easy synthesis methods such as co-precipitation or thermal decomposition partially explain this popularity surge. These methods yield particles of magnetic materials so small that they can only support one magnetic domain. They behave as one giant spin or magnetization, and because the energy required to flip this spin is smaller than the thermal energy, they display superparamagnetic behavior. This behavior has been well studied by techniques such as VSM or SQUID. However much research remains to be done on their magneto-optical characteristics. The magneto-optical spectra of Fe_3O_4 nanoparticles have been experimentally measured and theoretically predicted. These spectra are typically measured at low DC or AC fields, where the superparamagnetic response of the magnetism is approximated as linear behavior. We showed that even at these low fields there is a clear, though small, deviation from linearity. As such, the magneto-optical response will not only be visible at the applied magnetic field strength frequency in AC magnetic fields, but also at uneven harmonics. In chapter 5 we developed a theoretical framework to analyze this effect.

This framework opens up new perspectives, and two main applications can be envisaged in the future for this framework. The first lies in the characterization of superparamagnetic materials: by applying this framework one can determine the magnetic moment of the nanoparticles, an important material parameter among which is, among others, related to the nanoparticle size. It would be of interest to confirm the applicability of our initial findings, which focused on iron oxide nanoparticles, to other materials. Future research could also focus on characterizing deviations from ideal behavior, for instance by taking into account possible nanoparticle interactions or size distributions present in the material. The second application for this framework lies in the detection and recognition of superparamagnetic nanoparticles. Magnetic nanoparticles show promise in biomedical applications, and the ability to detect them *in situ* or in biological samples is important for diagnostics and for research towards their applications. The strengths of this technique reside in the ability to easily distinguish these nanoparticles from the rest of the sample by visualizing them at higher harmonics of the frequency of magnetic field while simultaneously acquiring information on their aggregation state and possible bio-degradation.

Finally, in chapter 6, we investigated the response of these superparamagnetic nanoparticles in nonlinear magneto-optics. Nonlinear optical techniques provide a wealth of information, such as orientation and information on the molecular environment, which is not apparent when applying linear optical techniques. For SHG these techniques are becoming established, but MSHG techniques have

not yet reached this level. For this reason we performed MSHG measurements on a PMMA/iron oxide nanoparticle nanocomposite, extending an existing theoretical framework in order to analyze our results. The obtained parameters yield insight into the nonlinear susceptibilities of the nanocomposite and its nanoparticles.

The framework can be applied to arbitrary symmetries; consequently, future research can use this to identify directional (magnetic) anisotropy in more complex samples than our isotropic nanocomposite. Additional nanocomposite MSHG measurements will provide a better understanding of the influence of magnetic nanoparticle parameters – such as size and shape – on their nonlinear susceptibilities. This knowledge would benefit applications such as identification of magnetic nanoparticles in MSHG microscopy images and could even be combined with detection at higher harmonics of the frequency of the magnetic field.

This dissertation has contributed to the understanding of the influence of magnetic fields on light–matter interaction. Progress has been made in understanding the optical response of both organic materials and superparamagnetic materials in a magnetic field. Both materials show promise for further fundamental research as well as practical applications, and future research will be able to build on our results in order to achieve a better understanding of their behavior in a magnetic field.

Appendix A

Tensors

Basic concepts

Tensors are mathematical objects that are used for certain complex mathematical calculations such as those necessary in Einstein's special and general relativity. A detailed analysis of tensor calculus is beyond the scope of this thesis (and was even hard for Einstein)[241] and can be found elsewhere.[242–244] In this appendix we will briefly explain the basic concepts of tensors and the necessary math in order to understand how they are applicable to optics.

Tensors can be viewed as multi-dimensional arrays of numbers. The dimension of the array is called the *rank* of a tensor. The lowest ranks of tensors are frequently used even in fields that do not require intense mathematics.

- Rank 0 – A "number" is also known as a scalar and is actually a rank 0 tensor
- Rank 1 – Vectors are rank 1 tensors; they require one dimension, either one column or one row, to be displayed
- Rank 2 – Matrices are rank 2 tensors; they require two dimensions to be displayed
- Rank 3 – The blocks of a Rubik's Cube can be viewed as a rank 3 tensor; a Rubik's Cube is three-dimensional and consists of three elements in each dimension

Higher order tensors are more difficult to visualize but can be considered an extension of the lower rank tensors.

Basic math

In order to apply tensors in nonlinear optics, basic knowledge is necessary on their mathematical transformations. To understand this dissertation, it is only necessary to understand two basic operations. Addition between two tensors of the same rank is as simple as adding the respective elements of both tensors, and yields a tensor of the same rank. An example for adding two rank 1 tensors A and B, both in compact and in full notation is as follows

$$A_i + B_i = C_i \tag{A.1}$$

$$\begin{bmatrix} A_x \\ A_y \\ A_z \end{bmatrix} + \begin{bmatrix} B_x \\ B_y \\ B_z \end{bmatrix} = \begin{bmatrix} A_x + B_x \\ A_y + B_y \\ A_z + B_z \end{bmatrix} = \begin{bmatrix} C_x \\ C_y \\ C_z \end{bmatrix} \tag{A.2}$$

Multiplication is slightly more complicated. Tensors can be multiplied like scalars can, with a few key differences. Tensor multiplication is not commutative, so

$$AB \neq BA \tag{A.3}$$

It is however distributive

$$A(B + C) \equiv AB + AC \tag{A.4}$$

For multiplication in nonlinear optics, we use the inner product. The result of the inner product of a tensor of rank n with a tensor of rank m is a tensor of rank $n + m - 2$. This is most easily seen in the inner product r of a matrix M with a vector v

$$r = M \cdot v = \begin{bmatrix} M_{11} & M_{12} & M_{13} \\ M_{21} & M_{22} & M_{23} \\ M_{31} & M_{32} & M_{33} \end{bmatrix} \cdot \begin{bmatrix} v_1 \\ v_2 \\ v_3 \end{bmatrix} = \begin{bmatrix} M_{11}v_1 + M_{12}v_2 + M_{13}v_3 \\ M_{21}v_1 + M_{22}v_2 + M_{23}v_3 \\ M_{31}v_1 + M_{32}v_2 + M_{33}v_3 \end{bmatrix} \tag{A.5}$$

$$r_i = \sum_j M_{ij} v_i \tag{A.6}$$

or in the Einstein summation convention

$$r_i = M_{ij} v_i \tag{A.7}$$

More generally, we can write the inner product C of a tensor A of rank n with a tensor B of rank m as

$$C_{i_1,i_2,\cdots,i_{n+m-2}} = A_{i_1,i_2,\cdots,i_n} B_{i_1,i_2,\cdots,i_m} \tag{A.8}$$

Pseudotensors

Finally we need to make a distinction between a true or polar tensor and a pseudo- or axial tensor. Many common vectors in basic science, such as speed and electric field, are true vectors. Two important, well-known pseudovectors are the magnetic field and angular momentum. The important difference between a true and a pseudovector for our purposes can be best described by comparing the effect of inversion on speed and angular momentum. The effect of an inversion center on the speed and angular momentum of a capybara are depicted in fig. A.1.

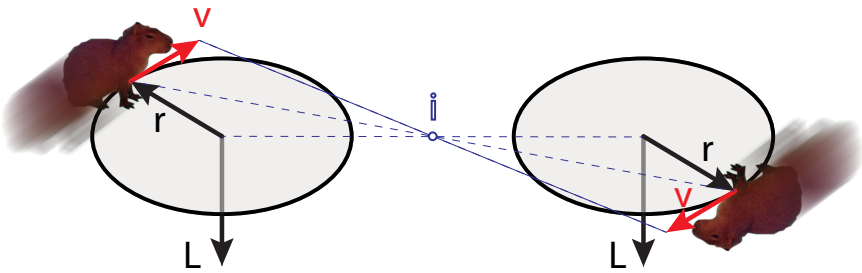

Figure A.1: When the speed of a moving capybara $\vec{v}$, a true tensor, is inverted by a center of inversion i, it changes direction. The angular momentum $\vec{L}$ of a moving capybara is a pseudotensor, and it does not change direction upon inversion.

Speed $\vec{v}$ is a true vector, obtained by deriving the position with respect to time

$$\vec{v} = \frac{\mathrm{d}\vec{x}}{\mathrm{d}t} \tag{A.9}$$

When we invert the entire situation, the following transformation happens

$$x \to -x \tag{A.10}$$

$$y \to -y \tag{A.11}$$

$$z \to -z \tag{A.12}$$

Speed is also inverted, and so it obtains a change in sign

$$\vec{v}_{inverted} = \frac{\mathrm{d}\vec{x}_{inverted}}{\mathrm{d}t} = \frac{\mathrm{d}(-\vec{x})}{\mathrm{d}t} = -\frac{\mathrm{d}\vec{x}}{\mathrm{d}t} = -\vec{v} \tag{A.13}$$

Angular momentum $\vec{L}$ is a pseudovector, obtained by the cross product of position $\vec{r}$ and mass times speed $m\vec{v}$

$$\vec{L} = \vec{r} \times m\vec{v} \tag{A.14}$$

An interesting thing happens when we invert the entire situation. Speed and location are true vectors, and so they acquire a change in sign. But this yields for the angular momentum

$$\vec{L}_{inverted} = \vec{r}_{inverted} \times m\vec{v}_{inverted} = -\vec{r} \times m(-\vec{v}) = \vec{r} \times m\vec{v} = \vec{L} \tag{A.15}$$

We see that $\vec{L}$ does not change sign when it is inverted. To be rigorous, we say that pseudotensors acquire an additional sign flip under improper transformations. Mirror planes or centers of inversion are improper transformations. The presence or precisely the lack of mirror planes and inversion centers in a sample is of crucial importance for SHG and MSHG. For MSHG the distinction between true and pseudotensors is extremely important as the magnetic induction $\vec{B}$ is a pseudovector. Inner products of pseudovectors also behave in a peculiar way

- vector · vector = pseudovector
- pseudovector · vector = vector
- vector · pseudovector = vector
- pseudovector · pseudovector = pseudovector

which is important when considering the symmetry of magneto-optical effects, e.g. $\vec{P} \sim \chi^{(3),eeem} \cdot \vec{E} \cdot \vec{E} \cdot \vec{B}$

Appendix B

Faraday rotation and dispersion in the visible region for saturated organic liquids: supporting information

B.1 Units

Table B.1: Conversion between SI units and atomic units

Atomic unit	SI value	
energy	$4.360 \times 10^{-18}\,\mathrm{J}$	
length	$5.292 \times 10^{-11}\,\mathrm{m}$	$27.211\,\mathrm{eV}$
magnetic field	$2.35 \times 10^{5}\,\mathrm{T}$	$2.35 \times 10^{9}\,\mathrm{G}$
time	$2.419 \times 10^{-17}\,\mathrm{s}$	
electric polarizability	$1.649 \times 10^{-41}\,\mathrm{C^2m^2/J}$	
Verdet constant	$8.040 \times 10^{4}\,\mathrm{rad\,T^{-1}\,m^{-1}}$	$4.606 \times 10^{6}\,^\circ\,\mathrm{T^{-1}\,m^{-1}}$

B.2 Measured and calculated Verdet constants of liquids

Table B.2: Measured Verdet constants of liquids ($^\circ\,\mathrm{T}^{-1}\,\mathrm{m}^{-1}$)

Wavelength (nm)	Pentane	±	Hexane	±	Heptane	±	Octane	±	Isooctane	±	Cyclopentane	±	Cyclohexane	±	Methanol	±	Ethanol	±
400	404.58	1.27	423.07	1.42	430.01	1.30	439.72	1.08	472.03	1.42	432.24	1.18	430.32	1.34	328.31	1.64	394.14	2.01
410	396.83	1.57	410.19	1.09	425.07	1.51	432.76	1.21	467.86	1.35	420.61	1.67	423.74	1.22	326.46	1.18	388.59	1.18
420	382.26	0.83	394.46	2.89	408.48	0.81	418.53	1.43	449.47	0.90	406.55	1.02	409.54	1.52	312.85	0.93	381.31	1.13
430	367.18	0.89	382.56	1.14	392.28	1.30	401.83	1.30	430.31	1.75	389.95	1.36	395.12	1.18	303.78	1.81	361.62	1.97
440	350.33	1.22	363.93	1.22	373.63	1.38	387.43	1.36	410.48	2.06	370.28	1.32	375.21	1.15	289.91	1.87	342.83	1.43
450	336.89	0.63	345.94	0.81	358.44	1.70	366.00	0.62	390.01	0.88	355.25	1.31	355.71	0.81	276.66	1.45	329.57	1.96
460	320.29	0.92	329.70	0.95	338.51	1.00	347.65	0.59	369.78	0.71	337.99	1.26	338.60	0.79	263.35	1.03	313.54	1.60
470	307.07	1.02	313.62	1.17	325.51	1.45	331.94	0.70	356.38	0.95	323.84	1.23	325.80	1.25	249.95	1.15	298.64	1.12
480	295.06	1.01	303.53	1.45	313.44	1.03	323.17	1.35	342.60	1.42	311.51	0.98	312.92	0.86	240.82	1.16	287.53	1.09
490	279.69	0.83	289.86	1.06	298.94	1.42	305.85	0.98	325.27	0.85	297.44	0.76	298.55	1.04	229.99	1.18	273.28	1.73
500	269.32	0.86	276.07	0.74	285.65	0.59	294.06	0.96	311.70	0.70	284.26	1.06	288.00	0.65	220.76	1.43	262.17	1.20
510	255.87	1.03	263.89	1.12	271.55	0.58	282.23	1.22	298.09	0.93	270.92	1.27	273.48	0.90	211.69	1.08	248.66	1.38
520	245.41	0.68	251.85	0.73	260.99	0.65	268.07	1.15	283.24	0.84	259.10	0.95	260.99	0.51	200.03	1.15	238.07	0.84
530	234.52	1.21	241.41	0.51	250.07	0.65	256.82	0.87	270.51	1.06	249.39	1.31	250.32	1.14	192.50	1.15	229.00	1.22
540	225.87	0.78	233.40	1.06	241.63	0.73	246.83	0.72	262.92	1.03	238.46	0.56	242.52	0.74	183.87	0.72	219.25	0.88
550	218.98	0.92	224.34	0.68	232.22	0.90	239.39	0.86	253.99	1.23	231.90	0.96	233.60	1.14	178.48	1.01	213.28	0.99
560	211.65	0.79	215.74	0.70	224.53	1.09	230.69	0.95	243.34	0.72	224.37	1.31	226.12	0.91	173.44	1.37	205.55	0.99
570	204.30	0.75	209.16	0.98	215.45	1.13	221.69	0.69	233.75	1.01	215.38	0.96	217.74	0.75	165.35	0.92	198.33	0.73
580	195.69	1.04	200.20	0.61	208.07	0.94	213.12	1.02	224.48	0.58	205.09	0.70	209.22	1.01	159.44	0.74	190.17	1.06
590	188.24	0.75	193.86	0.62	200.30	0.44	205.24	0.47	214.83	0.88	199.53	0.65	201.36	0.83	153.54	0.57	183.32	0.69
600	181.22	0.48	186.13	0.76	193.36	0.96	198.06	0.73	207.20	0.66	190.31	0.75	193.26	0.63	147.41	0.69	175.21	0.66
610	172.50	0.54	176.46	0.81	183.22	0.52	188.64	0.66	197.64	0.29	181.27	0.52	184.34	0.83	140.60	0.69	166.34	0.47
620	167.16	0.35	171.53	0.34	178.28	0.39	183.28	0.33	192.09	0.77	176.18	0.45	179.93	0.39	136.99	0.50	163.37	0.53
630	163.81	0.97	168.90	0.95	174.32	0.69	178.74	0.74	187.43	0.63	173.20	0.61	174.29	0.90	133.59	0.62	159.71	0.60
640	159.91	1.01	163.66	0.68	169.09	0.57	174.61	0.69	182.02	0.47	168.17	0.72	169.97	0.54	130.45	0.44	154.35	0.32
650	153.27	0.50	157.87	0.44	163.72	0.67	167.46	1.01	176.05	0.74	163.34	1.10	164.41	0.55	126.40	0.64	149.91	0.77
660	148.81	0.98	152.95	0.58	157.48	0.62	161.99	0.90	171.70	1.02	156.56	0.59	158.47	0.64	121.13	1.00	144.51	0.45
670	142.90	0.31	146.95	0.23	151.94	0.40	156.40	0.66	165.09	0.76	151.25	0.25	153.13	0.71	117.02	0.51	139.66	0.69
680	138.06	0.50	142.63	0.48	146.63	0.54	151.10	0.52	159.45	0.83	146.00	0.51	148.50	0.62	113.55	0.61	134.56	0.66
690	133.66	0.52	138.24	0.76	143.65	0.49	146.90	0.50	153.91	0.62	142.11	0.26	143.50	0.26	110.63	0.45	129.71	0.83
700	128.82	0.56	135.12	0.54	139.72	0.54	143.85	0.49	149.73	0.35	138.26	0.77	139.95	0.44	107.47	0.75	127.68	0.62
710	126.32	0.23	130.83	0.27	135.75	0.57	138.32	0.64	145.56	0.34	135.08	0.61	134.76	0.77	104.34	0.69	123.81	0.67
720	122.30	0.49	126.84	0.58	131.09	0.71	134.78	0.64	140.89	0.37	129.60	0.47	131.67	0.54	100.72	0.55	119.90	0.46
730	119.82	0.41	124.02	0.46	127.72	0.66	131.96	0.66	137.78	0.64	127.08	0.49	129.77	0.41	99.28	0.46	116.41	0.61
740	116.28	0.38	119.87	0.71	124.54	0.60	127.63	0.36	134.41	0.54	123.87	0.63	125.64	0.56	95.28	0.34	113.83	0.40
750	113.46	0.46	116.80	0.73	120.72	0.67	124.00	0.54	130.50	0.48	119.98	0.46	121.34	0.64	93.10	0.45	110.15	0.68
760	109.43	0.44	112.65	0.48	116.77	0.55	120.22	0.60	125.60	0.40	115.91	0.28	117.22	0.46	90.07	0.28	106.59	0.37
770	107.80	0.56	110.96	0.30	114.15	0.57	117.73	0.31	123.70	0.49	114.44	0.66	116.42	0.59	88.39	0.51	105.11	0.71
780	106.78	0.53	108.90	0.55	114.48	0.96	117.89	0.61	122.38	0.74	111.77	1.09	114.32	0.98	87.02	0.49	103.04	0.56
790	102.73	0.41	106.70	0.41	111.40	0.52	113.78	0.43	119.77	0.48	109.47	0.35	110.58	0.61	83.89	0.84	101.83	0.84
800	99.28	0.40	101.70	0.34	106.30	0.30	109.10	0.34	114.69	0.69	104.73	0.41	107.10	0.43	81.52	0.67	96.61	0.47

Table B.3: Measured Verdet constants of liquids ($^\circ\,\mathrm{T}^{-1}\,\mathrm{m}^{-1}$)

Wavelength (nm)	1-Propanol	±	2-Propanol	±	1-Butanol	±	2-Butanol	±	Isobutanol	±	1-Pentanol	±	2-Pentanol	±	3-Pentanol	±	3-Methyl-1-Butanol	±
400			435.27	1.83	427.98	1.93	445.27	1.39	438.55	1.52	443.28	1.16	453.21	2.08	445.17	1.21	456.25	1.11
410	414.61	1.05	430.39	1.72	421.60	2.24	440.30	1.60	434.20	1.11	436.56	1.63	442.28	1.53	440.23	1.18	447.26	1.45
420	397.01	1.33	417.60	1.28	412.43	0.96	421.73	0.89	418.17	0.76	419.37	1.16	428.57	1.53	425.87	1.33	431.21	1.53
430	382.13	1.52	402.97	1.98	397.79	1.23	403.28	0.63	401.03	0.84	403.53	1.13	409.56	1.94	408.73	2.27	411.65	1.15
440	362.43	1.23	378.75	2.07	375.28	0.80	384.63	1.25	381.13	1.30	381.24	1.44	390.13	2.00	391.52	1.73	393.07	1.23
450	344.92	0.82	364.32	1.52	356.34	1.72	369.82	1.49	365.09	0.89	364.39	1.80	373.58	0.75	374.19	1.27	373.44	1.21
460	327.94	0.91	344.28	0.93	344.12	1.92	349.52	0.61	346.97	0.86	345.42	1.00	353.05	1.39	354.52	0.87	353.29	1.23
470	311.45	1.62	330.78	2.13	327.86	1.47	337.29	1.85	330.52	1.04	332.92	1.42	339.48	1.77	340.30	0.86	341.56	0.89
480	304.58	1.77	317.24	0.68	313.28	1.64	323.53	0.69	321.22	1.41	321.19	0.95	328.06	0.78	326.77	0.96	329.61	1.00
490	286.76	2.04	302.20	1.37	300.09	1.65	310.62	1.08	305.33	1.36	305.68	0.92	312.00	0.97	313.64	1.64	313.13	1.55
500	276.00	1.22	290.22	1.12	287.68	1.00	297.84	0.76	291.31	1.19	293.29	0.63	298.00	1.13	300.08	1.63	299.89	0.77
510	265.28	1.18	280.56	1.54	274.60	1.61	282.43	1.56	277.56	1.16	276.84	0.78	284.74	0.61	286.79	1.00	285.40	1.88
520	249.86	0.88	264.47	0.85	259.36	1.06	270.65	0.80	264.97	0.78	265.86	0.84	272.46	1.09	271.55	0.68	273.20	0.79
530	241.09	1.12	255.53	1.34	250.95	0.95	257.96	0.78	255.62	0.47	256.80	1.05	260.98	1.00	259.50	0.92	262.55	0.93
540	231.05	0.65	241.95	1.27	241.44	0.72	250.43	0.91	245.57	0.61	245.94	0.76	250.60	0.71	251.89	1.07	252.43	1.30
550	223.42	1.28	235.21	0.92	234.19	1.26	241.24	0.89	237.00	1.49	239.02	1.25	241.11	0.79	243.95	0.54	244.40	0.84
560	215.56	1.32	225.42	1.41	226.02	1.93	231.85	1.83	229.90	1.24	227.51	0.70	232.02	0.97	236.02	1.44	235.08	0.62
570	207.06	0.65	219.01	0.90	216.88	1.22	222.81	0.77	221.22	0.84	220.82	0.82	225.27	0.78	223.77	1.05	226.61	0.71
580	200.87	0.99	211.72	1.47	209.59	0.87	216.12	0.78	210.02	1.27	211.94	0.83	216.45	0.72	216.80	1.02	215.78	0.67
590	190.98	0.74	201.20	0.74	200.53	0.85	208.67	0.81	203.32	0.68	204.62	0.56	207.78	0.48	209.96	0.84	210.53	0.77
600	184.07	0.59	193.44	0.62	191.51	0.68	200.50	0.82	195.90	0.50	196.54	0.75	199.42	0.69	200.88	0.73	200.92	0.72
610	176.72	0.49	185.85	0.46	183.04	0.52	190.42	0.51	187.31	0.77	186.88	0.54	192.06	0.95	192.14	0.62	191.81	0.59
620	172.04	0.59	179.24	0.80	178.06	0.53	183.49	0.70	181.03	0.40	182.12	0.48	185.76	0.39	187.07	0.48	187.01	0.56
630	168.45	1.18	173.18	1.13	175.31	0.76	180.69	0.71	177.27	0.66	177.47	0.74	180.54	0.86	182.42	0.41	181.05	0.82
640	163.27	0.55	169.30	0.91	171.45	0.46	175.25	0.70	172.09	0.82	172.52	0.66	175.35	0.87	176.60	0.70	177.60	0.72
650	157.98	0.46	164.35	0.52	163.81	0.62	170.47	1.00	166.73	0.46	166.14	0.51	169.24	0.56	171.55	0.66	171.34	0.92
660	152.15	0.70	157.15	0.96	156.73	0.66	163.21	0.67	160.96	0.46	161.30	0.49	165.09	0.83	165.71	0.76	164.99	0.56
670	146.29	0.47	152.65	0.35	152.97	0.33	156.21	1.00	154.30	0.63	155.43	0.26	158.11	0.33	159.84	0.40	158.66	0.36
680	142.09	0.62	147.44	0.51	147.52	0.43	152.21	0.46	150.30	0.62	150.05	0.49	153.61	0.48	153.58	0.53	153.99	0.45
690	137.90	0.26	145.00	0.52	143.38	0.76	147.46	0.35	146.73	0.43	146.44	0.35	149.99	0.43	151.14	0.76	150.44	0.28
700	134.49	0.63	140.69	0.52	139.57	0.41	144.68	0.75	142.21	0.55	143.55	0.68	144.55	0.49	146.28	0.52	145.04	0.77
710	129.78	0.72	135.29	0.69	134.99	0.64	140.09	0.41	137.64	0.37	137.33	0.30	141.34	0.61	142.59	0.69	142.35	0.47
720	126.46	0.44	131.57	0.57	131.09	0.56	135.86	0.36	133.86	0.55	133.61	0.56	136.19	0.58	137.30	0.46	136.47	0.59
730	123.40	0.62	129.83	0.55	127.50	0.52	133.10	0.45	129.86	0.63	130.35	0.45	133.73	0.36	134.36	0.53	133.85	0.35
740	119.86	0.40	125.77	0.68	123.86	0.40	128.06	0.65	127.49	0.74	127.53	0.65	129.54	0.35	130.16	0.48	130.23	0.31
750	117.31	0.38	122.17	0.43	121.20	0.47	125.26	0.59	122.54	0.50	123.31	0.68	126.79	0.51	126.74	0.62	126.20	0.54
760	112.74	0.41	118.53	0.26	117.68	0.38	121.16	0.46	118.48	0.50	119.23	0.43	121.37	0.32	121.73	0.32	122.29	0.51
770	110.05	0.57	115.68	0.85	115.07	0.70	118.39	0.49	116.42	0.43	116.79	0.32	120.02	0.48	120.29	0.45	119.75	0.46
780	110.35	0.63	113.31	0.74	113.79	0.51	116.68	0.70	115.47	0.67	115.34	0.72	118.18	0.64	118.57	0.57	117.43	0.61
790	105.62	0.68	111.54	0.63	110.60	0.58	113.62	0.65	112.44	0.44	112.17	0.38	114.96	0.35	115.86	0.58	115.91	0.46
800	101.66	0.44	106.33	0.87	106.45	0.45	108.86	0.74	107.16	0.33	108.23	0.30	109.84	0.26	111.10	0.34	110.50	0.34

Table B.4: Measured Verdet constants of liquids ($^\circ\,\mathrm{T}^{-1}\,\mathrm{m}^{-1}$)

Wavelength (nm)	Hexanol	±	DiethylEther	±	MethylPropylEther	±	MTBE	±	1,2-Dimethoxyethane	±	Dioctylether	±	2-MethoxyEthylether	±	Propylene Glycol	±	1,3-PropaneDiol	±
400	446.39	0.99	383.51	1.69	381.86	1.91	404.95	0.97	389.35	0.78	461.37	2.28	409.45	1.04	451.64	2.89	424.23	1.19
410	442.71	1.22	377.53	1.88	374.67	1.21	395.75	1.25	380.95	0.86	455.75	1.59	399.07	1.04	447.16	1.62	420.83	1.51
420	428.71	1.66	364.52	0.72	358.72	1.89	382.38	1.48	367.39	1.49	442.23	1.28	386.92	0.95	431.41	1.48	406.24	1.30
430	411.71	1.22	348.70	1.01	345.97	1.00	368.66	1.17	353.33	1.68	424.91	1.37	370.61	0.70	416.00	1.44	394.61	1.71
440	390.50	1.42	334.31	1.78	330.52	1.41	349.92	1.15	335.68	0.94	406.16	1.40	351.90	1.63	394.35	0.94	374.01	1.72
450	373.31	1.29	320.68	1.56	315.58	1.35	333.39	0.68	320.77	0.39	388.65	0.98	339.72	1.45	375.30	1.14	360.09	1.78
460	356.55	1.12	302.34	0.95	296.85	1.09	315.08	0.82	303.20	0.96	368.68	1.21	319.39	0.63	359.05	1.27	339.73	1.32
470	339.82	1.37	289.90	0.64	288.63	1.11	304.74	0.92	292.25	0.91	353.47	1.20	307.62	1.11	345.07	1.75	329.44	0.71
480	325.93	1.46	273.74	1.03	275.39	1.33	291.14	0.95	282.03	0.75	341.78	0.99	297.53	1.00	333.60	1.01	316.61	1.17
490	315.87	1.44	263.09	1.28	263.67	0.98	278.41	1.20	269.73	1.43	324.59	1.19	280.82	1.06	318.54	1.36	304.05	1.52
500	303.82	0.96	251.89	0.98	253.29	0.46	267.21	0.81	258.15	0.57	311.05	0.83	270.34	1.10	303.09	0.74	289.23	1.07
510	286.85	0.92	239.36	0.90	241.44	0.69	255.05	0.92	246.00	0.87	296.81	0.71	256.46	0.92	289.87	1.23	277.08	0.91
520	274.92	0.77	229.94	0.64	229.14	0.51	243.38	1.00	235.49	0.72	282.93	0.49	246.09	0.71	277.32	0.48	263.50	0.73
530	263.92	0.66	219.34	0.64	220.41	0.54	233.96	0.56	227.32	0.89	270.82	0.50	234.91	0.83	265.09	1.28	254.48	0.75
540	253.71	0.82	213.00	0.62	212.73	0.73	223.78	0.73	217.30	0.49	261.42	0.72	227.22	0.50	255.41	0.91	243.65	0.72
550	245.59	0.83	206.85	0.85	204.05	0.81	217.62	0.60	210.83	0.99	253.90	1.31	220.15	0.43	247.12	0.80	237.53	0.87
560	237.38	1.00	199.13	0.58	196.99	1.04	209.62	0.53	203.87	0.85	242.60	1.17	209.73	0.96	238.74	0.94	228.41	0.80
570	228.01	0.81	189.93	0.83	189.52	0.56	201.71	0.96	194.30	0.80	232.93	0.94	203.90	0.90	229.25	0.89	219.92	1.14
580	218.33	0.87	187.65	0.98	182.70	0.60	193.45	0.87	187.00	0.49	227.17	0.95	194.51	0.88	218.42	0.36	210.66	0.62
590	211.18	0.68	179.39	0.43	175.85	0.78	186.89	0.55	179.28	0.35	217.86	0.95	188.29	0.71	210.66	0.36	204.45	0.42
600	204.23	1.22	172.58	0.68	169.76	0.92	180.31	0.59	171.29	0.51	208.99	0.69	180.42	0.73	202.34	0.43	195.83	0.56
610	194.83	0.84	164.92	0.49	160.89	0.58	172.98	0.91	164.46	0.65	199.86	0.69	172.07	0.45	194.40	0.60	188.11	0.78
620	188.73	0.67	159.87	0.65	156.05	0.24	166.04	0.63	159.44	0.33	193.49	0.59	169.02	0.54	188.17	0.67	182.56	0.75
630	183.72	0.51	155.49	0.76	153.24	0.33	162.50	0.47	155.07	0.44	188.62	0.78	164.03	0.52	183.64	0.57	179.26	0.72
640	179.43	0.55	151.39	0.61	149.08	0.73	157.59	0.49	150.08	0.33	184.10	0.37	159.35	0.29	179.46	0.90	172.29	0.72
650	173.47	0.71	146.98	0.63	144.66	0.49	152.94	0.55	146.88	0.55	178.74	0.62	153.69	0.65	174.83	1.03	168.39	0.61
660	167.88	0.72	141.06	0.65	139.25	0.45	147.89	0.58	140.95	0.69	171.73	0.74	149.39	0.63	167.28	0.87	162.51	0.52
670	161.44	0.59	135.17	0.44	134.27	0.38	143.17	0.71	135.65	0.33	166.36	0.52	143.51	0.44	161.29	0.47	156.61	0.60
680	155.97	0.58	130.57	0.78	130.04	0.51	137.66	0.61	132.06	0.45	160.71	0.33	139.57	0.51	155.71	0.61	150.65	0.53
690	152.04	0.53	127.53	0.64	126.18	0.50	134.09	0.52	127.81	0.30	155.39	0.41	135.04	0.54	150.55	0.55	147.38	0.48
700	147.62	0.34	123.70	0.47	122.76	0.30	131.32	0.52	124.97	0.30	151.60	0.62	131.47	0.42	147.06	0.76	143.29	0.32
710	142.87	0.41	120.39	0.42	119.19	0.40	125.62	0.33	121.18	0.36	147.37	0.54	127.68	0.33	143.16	0.39	139.54	0.24
720	139.08	0.47	116.82	0.52	114.62	0.60	122.49	0.60	117.21	0.58	142.64	0.54	123.22	0.45	138.34	1.00	134.40	0.53
730	135.70	0.41	112.96	0.38	111.07	0.42	119.34	0.56	114.46	0.69	139.51	0.81	121.15	0.46	135.59	0.35	131.09	0.56
740	131.54	0.42	110.08	0.48	108.03	0.76	115.85	0.56	111.39	0.41	135.90	0.53	117.95	0.41	132.44	0.97	128.38	0.52
750	128.74	0.50	107.83	0.59	105.71	0.67	113.32	0.44	107.99	0.58	131.17	0.45	113.98	0.44	127.52	0.51		
760	123.67	0.57	103.67	0.42	101.90	0.41	109.33	0.68	104.31	0.30	127.05	0.54	110.23	0.52	123.17	0.36		
770	120.72	0.69	102.08	0.43	99.92	0.23	107.50	0.46	102.91	0.32	124.87	0.58	108.40	0.37	120.66	0.98		
780	118.47	0.66	101.25	0.76	98.41	0.51	106.10	0.76	101.73	0.56	124.24	0.72	107.09	0.34	119.65	0.53		
790	117.25	0.68	97.36	0.38	95.66	0.32	102.57	0.50	99.22	0.40	120.17	0.51	104.05	0.57	118.70	0.57		
800	112.43	0.22	94.18	0.48	92.22	0.50	98.50	0.25	94.33	0.46	115.80	0.47	100.00	0.28	112.99	0.37		

Table B.5: Measured Verdet constants of liquids ($^\circ\,\mathrm{T}^{-1}\,\mathrm{m}^{-1}$)

Wavelength (nm)	n-ButylAmine	±	n-Octylamine	±	Acetone	±	DCM	±	THF	±	Tetrahydropyrane	±	1,4 Dioxane	±	H_2O	±
400	470.28	1.64	471.41	1.64	394.33	1.70	565.07	1.87	395.09	1.78	415.27	1.47	401.02	1.36	468.85	1.70
410	462.34	1.67	466.95	1.08	390.06	1.10	555.12	3.10	389.14	1.31	406.53	1.23	394.76	1.71	459.23	2.22
420	448.24	1.35	450.10	1.08	379.14	1.24	539.32	1.75	376.00	0.62	394.68	2.12	380.72	0.99	443.83	1.15
430	429.61	1.68	433.46	1.13	363.40	1.57	516.82	2.29	359.24	2.15	379.47	1.52	366.42	1.33	425.90	1.82
440	411.26	1.95	413.26	1.64	346.24	1.12	494.71	2.09	346.73	0.86	362.50	2.15	347.82	1.78	406.51	1.64
450	389.70	1.52	396.89	1.20	330.40	0.89	473.48	1.84	328.12	1.59	346.79	1.67	331.40	1.02	386.67	1.13
460	370.85	1.45	375.19	0.76	312.91	1.54	446.25	1.37	315.13	1.04	327.04	0.98	312.85	1.31	366.84	1.52
470	355.49	1.87	361.40	0.71	298.65	1.76	428.77	1.66	300.02	1.58	314.13	1.15	303.82	1.02	350.29	0.94
480	338.84	1.19	348.01	0.72	286.66	1.57	410.76	1.12	288.09	1.28	302.64	0.62	293.05	1.05	336.84	1.16
490	322.69	1.41	332.63	1.41	274.81	1.36	389.96	2.58	274.43	1.44	291.96	1.43	278.99	0.78	321.11	2.17
500	311.56	1.26	313.06	0.82	263.43	0.86	376.69	2.08	263.32	2.02	277.12	0.91	266.04	0.77	307.83	1.92
510	294.91	1.55	302.12	1.25	252.63	1.64	357.67	1.77	251.07	2.25	263.48	0.97	253.85	1.40	294.26	1.43
520	281.01	1.26	290.63	0.97	240.06	0.91	340.82	0.90	239.15	0.80	252.06	1.04	244.53	1.07	280.23	1.12
530	269.96	0.88	277.64	0.99	229.06	1.24	325.93	1.25	230.43	0.97	242.98	0.78	231.53	0.86	270.38	1.56
540	260.54	1.32	268.76	0.82	219.45	0.80	315.53	1.37	221.29	1.06	233.61	0.95	223.25	0.78	257.88	1.35
550	250.15	1.37	258.81	0.73	211.69	1.50	303.02	1.06	215.13	1.25	226.48	0.85	216.06	0.72	249.04	0.99
560	240.54	1.13	249.41	0.93	206.22	0.83	292.53	0.98	207.97	1.17	216.23	0.86	209.72	1.07	241.12	0.93
570	231.18	1.02	240.56	0.98	198.06	0.90	280.64	1.36	197.21	0.66	207.55	0.79	200.06	0.61	231.64	1.37
580	224.98	1.40	229.41	1.16	191.13	1.01	270.49	1.24	191.14	0.98	200.89	0.62	194.24	0.78	222.06	0.89
590	213.90	0.83	221.18	0.61	182.19	0.93	261.03	0.94	184.29	0.57	194.36	0.37	186.65	0.57	214.05	0.94
600	206.97	0.91	213.86	0.83	174.84	0.95	251.12	1.25	175.99	0.45	186.22	0.84	178.56	0.63	205.20	1.12
610	197.76	0.59	204.12	1.03	168.41	0.59	238.33	0.72	168.46	0.85	178.34	0.78	170.73	0.72	195.84	0.45
620	193.10	0.51	196.83	0.67	161.02	0.65	230.30	0.53	164.61	0.86	172.51	0.60	164.89	0.32	190.99	0.39
630	188.57	0.45	194.70	0.80	157.83	0.93	225.95	0.79	158.85	0.66	169.35	0.53	161.95	0.68	186.00	0.47
640	181.35	1.12	188.22	0.59	153.64	0.77	220.21	1.20	154.64	0.45	163.64	0.73	156.77	1.11	181.92	1.06
650	176.73	0.79	181.93	0.68	150.13	0.56	212.48	0.79	149.32	0.41	159.41	0.59	152.06	0.58	174.03	0.59
660	170.95	0.80	174.62	0.53	143.52	0.69	205.55	0.63	144.84	0.80	152.60	0.47	147.39	0.56	168.63	0.70
670	163.96	0.46	169.09	0.59	139.07	0.50	197.41	0.73	139.99	0.45	148.18	0.62	141.25	0.40	162.90	0.51
680	158.84	0.55	163.04	0.77	134.46	0.45	191.48	0.64	135.94	0.61	142.37	0.61	138.05	0.67	156.91	0.55
690	154.58	0.83	158.05	0.50	132.04	0.55	185.92	0.90	130.98	0.41	138.22	0.81	133.24	0.47	153.66	0.71
700	150.32	1.01	156.01	0.43	126.95	0.84	181.23	0.37	127.74	0.48	134.65	0.73	129.26	0.45	149.93	0.94
710	146.28	0.55	150.61	0.60	122.99	0.39	174.30	0.75	124.16	0.69	130.95	0.32	125.15	0.58	144.64	0.55
720	141.71	0.47	145.13	0.58	119.58	0.40	169.98	0.46	120.06	0.30	126.75	0.73	122.45	0.44	139.14	0.45
730	139.09	0.61	141.90	0.60	116.83	0.33	166.08	0.51	117.04	0.56	123.82	0.30	119.13	0.39	136.56	0.58
740	134.75	0.54	138.10	0.71	113.87	0.40	160.91	0.52	114.40	0.52	120.98	0.37	116.17	0.34	132.22	0.49
750	130.65	0.47	133.93	0.68	110.06	0.31	157.17	0.43	111.35	0.44	117.75	0.48	112.40	0.70	129.34	0.40
760	125.74	0.38	130.07	0.63	106.19	0.47	151.04	0.32	107.53	0.39	112.94	0.34	108.77	0.38	124.76	0.43
770	123.62	0.62	126.53	0.84	105.08	0.37	148.62	0.56	104.46	0.33	110.58	0.43	106.33	0.30	122.01	0.56
780	121.85	0.45	126.97	1.22	103.43	0.28	146.71	0.45	103.44	0.42	109.45	0.66	106.49	1.13	120.19	0.53
790	118.45	0.58	121.06	0.56	100.40	0.80	142.85	0.50	100.80	0.64	107.18	0.30	102.85	0.32	116.90	0.71
800	113.49	0.80	117.25	0.48	96.62	0.63	136.67	0.67	95.81	0.51	102.70	0.48	98.33	0.51	112.06	0.53

Table B.6: Calculated Verdet constants of liquids ($^\circ\,\mathrm{T}^{-1}\,\mathrm{m}^{-1}$)

Wavelength (nm)	Pentane	Hexane	Heptane	Cyclopentane	Methanol	Ethanol	1-Propanol	2-Propanol	1-Butanol	2-Butanol	Isobutanol	1-Pentanol	2-Pentanol
400	357.70	375.01	378.83	350.80	204.52	290.82	312.37	411.23	350.36	420.08	385.62	353.71	416.92
410	337.96	354.30	357.89	331.92	193.93	275.35	295.62	387.69	331.30	396.29	364.30	334.46	393.41
420	320.31	335.78	339.17	315.00	184.39	261.45	280.59	366.74	314.23	375.08	345.23	317.21	372.45
430	303.94	318.61	321.80	299.25	175.49	248.51	266.61	347.38	298.36	355.46	327.54	301.19	353.04
440	288.75	302.68	305.70	284.61	167.18	236.47	253.61	329.49	283.63	337.32	311.14	286.31	335.09
450	274.68	287.91	290.78	271.01	159.44	225.27	241.52	312.96	269.96	320.54	295.94	272.51	318.48
460	261.64	274.24	276.96	258.39	152.24	214.87	230.30	297.70	257.28	305.03	281.86	259.70	303.12
470	249.01	260.99	263.57	246.14	145.22	204.76	219.41	282.96	244.98	290.03	268.22	247.29	288.27
480	237.87	249.31	251.77	235.31	139.01	195.82	209.78	269.99	234.13	276.83	256.20	236.32	275.19
490	227.58	238.52	240.87	225.30	133.25	187.55	200.88	258.04	224.10	264.66	245.09	226.19	263.13
500	217.58	228.03	230.27	215.54	127.62	179.49	192.20	246.45	214.33	252.84	234.30	216.33	251.41
510	208.36	218.36	220.50	206.54	122.42	172.04	184.19	235.78	205.32	241.97	224.35	207.24	240.63
520	199.88	209.47	211.52	198.25	117.62	165.18	176.81	225.99	197.03	231.98	215.20	198.87	230.72
530	192.09	201.30	203.27	190.63	113.20	158.87	170.03	217.01	189.41	222.81	206.80	191.17	221.63
540	184.49	193.33	195.22	183.18	108.87	152.70	163.40	208.27	181.97	213.88	198.60	183.66	212.77
550	177.07	185.56	187.36	175.91	104.64	146.67	156.92	199.75	174.71	205.18	190.60	176.33	204.13
560	170.73	178.91	180.65	169.68	101.01	141.50	151.38	192.48	168.49	197.74	183.76	170.05	196.75
570	164.09	171.95	173.62	163.16	97.20	136.09	145.57	184.87	161.98	189.96	176.61	163.48	189.02
580	158.46	166.05	167.66	157.62	93.96	131.49	140.64	178.43	156.46	183.37	170.54	157.91	182.48
590	152.53	159.83	161.37	151.78	90.54	126.64	135.44	171.65	150.63	176.43	164.14	152.03	175.59
600	147.14	154.18	155.67	146.47	87.43	122.23	130.70	165.50	145.34	170.13	158.33	146.68	169.33
610	142.29	149.07	150.50	141.66	84.60	118.24	126.41	159.93	140.53	164.44	153.07	141.84	163.68
620	137.51	144.06	145.44	136.94	81.83	114.32	122.21	154.49	135.83	158.86	147.92	137.09	158.14
630	132.82	139.14	140.48	132.32	79.11	110.47	118.09	149.15	131.22	153.39	142.87	132.44	152.71
640	128.61	134.73	136.02	128.15	76.66	107.01	114.38	144.36	127.08	148.48	138.33	128.26	147.83
650	124.47	130.39	131.64	124.07	74.25	103.61	110.73	139.66	123.01	143.67	133.88	124.15	143.04
660	120.41	126.14	127.35	120.05	71.88	100.27	107.15	135.05	119.01	138.94	129.50	120.12	138.34
670	116.78	122.34	123.51	116.46	69.76	97.29	103.96	130.94	115.45	134.72	125.60	116.52	134.15
680	113.22	118.61	119.74	112.94	67.68	94.35	100.81	126.90	111.94	130.58	121.76	112.98	130.03
690	109.72	114.94	116.04	109.47	65.63	91.47	97.72	122.94	108.50	126.52	117.99	109.50	125.99
700	106.62	111.69	112.76	106.40	63.81	88.91	94.99	119.43	105.45	122.92	114.66	106.42	122.41
710	103.58	108.50	109.54	103.38	62.02	86.40	92.30	115.99	102.44	119.38	111.38	103.39	118.89
720	100.58	105.36	106.37	100.41	60.26	83.92	89.64	112.60	99.49	115.90	108.15	100.41	115.43
730	97.63	102.27	103.24	97.49	58.53	81.48	87.04	109.27	96.58	112.48	104.97	97.48	112.03
740	95.05	99.56	100.51	94.93	57.01	79.35	84.75	106.35	94.04	109.49	102.20	94.91	109.05
750	92.51	96.90	97.83	92.40	55.51	77.24	82.50	103.48	91.53	106.54	99.46	92.38	106.12
760	90.00	94.28	95.18	89.92	54.03	75.17	80.28	100.66	89.06	103.64	96.76	89.89	103.23
770	87.54	91.69	92.57	87.47	52.57	73.13	78.10	97.88	86.63	100.78	94.11	87.43	100.39
780	85.11	89.15	90.00	85.05	51.14	71.12	75.95	95.14	84.23	97.97	91.50	85.01	97.59
790	83.01	86.95	87.78	82.97	49.90	69.38	74.09	92.78	82.17	95.55	89.24	82.93	95.18
800	80.95	84.79	85.60	80.92	48.67	67.67	72.26	90.45	80.13	93.16	87.02	80.87	92.80

Table B.7: Calculated Verdet constants of liquids ($^\circ\,\mathrm{T}^{-1}\,\mathrm{m}^{-1}$)

Wavelength (nm)	3-Pentanol	3-Methyl-1-Butanol	DiethylEther	MethylPropylEther	MTBE	1,2-Dimethoxyethane	n-ButylAmine	Acetone	DCM	THF	Tetrahydropyrane	H_2O
400	405.99	358.09	320.88	330.48	348.71	293.38	408.19	369.39	316.73	263.09	364.67	503.72
410	383.44	338.51	303.53	312.29	329.53	277.48	384.86	348.39	299.11	249.67	343.93	473.69
420	363.29	320.99	287.98	296.02	312.37	263.23	364.12	329.67	283.38	237.56	325.48	447.07
430	344.61	304.72	273.51	280.92	296.45	249.99	344.95	312.36	268.80	226.22	308.42	422.58
440	327.30	289.61	260.07	266.92	281.67	237.69	327.25	296.35	255.29	215.63	292.66	400.04
450	311.26	275.60	247.58	253.94	267.98	226.27	310.89	281.54	242.78	205.74	278.09	379.28
460	296.42	262.61	236.00	241.91	255.28	215.68	295.79	267.87	231.20	196.51	264.64	360.18
470	282.04	250.01	224.75	230.25	242.98	205.40	281.20	254.65	220.00	187.52	251.64	341.79
480	269.37	238.90	214.82	219.97	232.13	196.33	268.36	243.01	210.12	179.55	240.20	325.65
490	257.68	228.63	205.64	210.48	222.11	187.94	256.54	232.29	201.00	172.16	229.65	310.83
500	246.31	218.64	196.70	201.25	212.37	179.78	245.06	221.88	192.14	164.93	219.42	296.48
510	235.83	209.43	188.46	192.73	203.38	172.24	234.50	212.31	183.97	158.24	210.00	283.32
520	226.20	200.94	180.86	184.90	195.12	165.30	224.80	203.51	176.46	152.06	201.35	271.25
530	217.35	193.16	173.88	177.71	187.52	158.93	215.91	195.44	169.57	146.37	193.41	260.22
540	208.73	185.55	167.06	170.69	180.12	152.70	207.24	187.58	162.85	140.79	185.68	249.49
550	200.31	178.13	160.40	163.84	172.88	146.62	198.80	179.92	156.29	135.33	178.14	239.06
560	193.12	171.78	154.70	157.98	166.70	141.42	191.59	173.39	150.68	130.65	171.70	230.17
570	185.59	165.12	148.73	151.85	160.23	135.97	184.05	166.54	144.81	125.74	164.96	220.88
580	179.20	159.48	143.67	146.65	154.74	131.34	177.66	160.75	139.84	121.56	159.25	213.03
590	172.48	153.53	138.33	141.17	148.95	126.46	170.93	154.65	134.60	117.15	153.24	204.78
600	166.37	148.13	133.47	136.18	143.69	122.03	164.83	149.11	129.83	113.13	147.78	197.30
610	160.85	143.24	129.08	131.68	138.93	118.01	159.31	144.11	125.52	109.48	142.85	190.55
620	155.44	138.44	124.77	127.26	134.27	114.08	153.91	139.21	121.30	105.90	138.02	183.95
630	150.13	133.74	120.54	122.92	129.69	110.22	148.61	134.41	117.16	102.38	133.28	177.49
640	145.35	129.51	116.73	119.03	125.58	106.74	143.85	130.09	113.44	99.21	129.03	171.69
650	140.67	125.36	113.00	115.20	121.55	103.33	139.19	125.86	109.79	96.10	124.85	166.02
660	136.07	121.28	109.33	111.45	117.58	99.98	134.61	121.71	106.20	93.04	120.76	160.46
670	131.97	117.64	106.06	108.10	114.05	96.99	130.52	118.01	103.00	90.30	117.10	155.50
680	127.93	114.06	102.84	104.81	110.57	94.05	126.51	114.38	99.86	87.61	113.51	150.64
690	123.97	110.55	99.68	101.57	107.16	91.16	122.57	110.81	96.77	84.95	109.98	145.86
700	120.47	107.43	96.88	98.71	104.13	88.60	119.09	107.65	94.04	82.61	106.86	141.65
710	117.02	104.37	94.12	95.89	101.16	86.08	115.66	104.54	91.35	80.29	103.80	137.51
720	113.62	101.36	91.41	93.12	98.23	83.60	112.29	101.72	88.70	78.01	100.78	133.44
730	110.29	98.39	88.74	90.39	95.35	81.17	108.98	95.85	86.10	75.77	97.81	129.44
740	107.37	95.80	86.40	88.00	92.84	79.03	106.08	93.29	83.82	73.80	95.21	125.95
750	104.49	93.24	84.10	85.65	90.35	76.93	103.22	90.77	81.58	71.86	92.66	122.51
760	101.66	90.72	81.83	83.33	87.91	74.85	100.41	88.29	79.37	69.95	90.14	119.12
770	98.87	88.24	79.60	81.05	85.50	72.81	97.64	85.84	77.19	68.06	87.66	115.80
780	96.12	85.80	77.40	78.80	83.13	70.80	94.92	83.44	75.05	66.21	85.22	112.52
790	93.75	83.69	75.50	76.87	81.09	69.07	92.57	81.37	73.20	64.60	83.12	109.70
800	91.42	81.61	73.63	74.96	79.07	67.36	90.26	79.32	71.38	63.02	81.04	106.92

Appendix C

Giant Faraday rotation in mesogenic organic molecules: supporting information

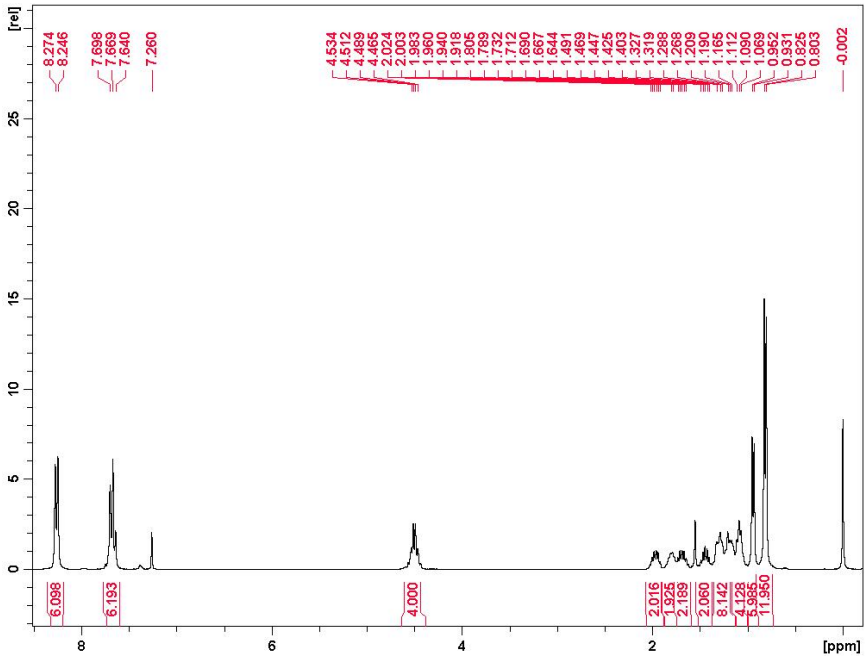

Figure C.1: ^{1}H NMR Spectrum of 1,3-bis[(*S*)-3,7-dimethyloctyloxy)]-5-fluoro-2,4,6-tris[(4-nitrophenyl)ethynyl]-benzene (BTB*).

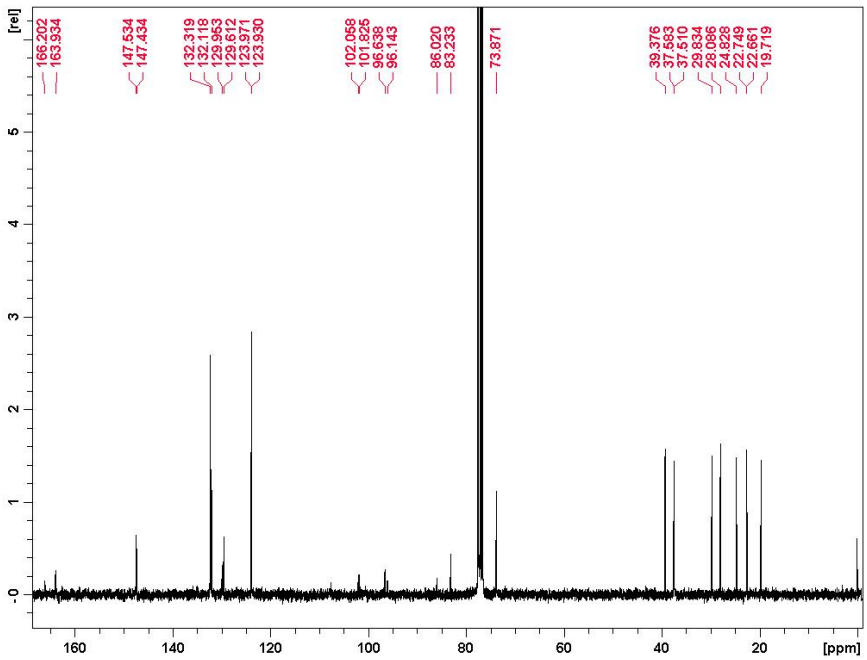

Figure C.2: ^{13}C NMR Spectrum of 1,3-bis[(*S*)-3,7-dimethyloctyloxy)]-5-fluoro-2,4,6-tris[(4-nitrophenyl)ethynyl]-benzene (BTB*).

Appendix D

Magneto-optical harmonic susceptometry of superparamagnetic materials: supporting information

Starting from the general derived eq. (5.13)

$$\theta = V\mu_0 \Bigg(H_0 \sin(A) + M_S \sum_{n=1}^{\infty} \Bigg[\frac{4 * B_{2n}(CH_0)^{2n-1}}{(2n)!} \sum_{k=0}^{n-1} (-1)^{n-1-k} \binom{2n-1}{k} \sin((2n-1-2k)A) \Bigg] \Bigg) d \tag{D.1}$$

and using Jones calculus to correlate the intensity on the photodiodes[26] eq. (D.2)

$$\theta = -\frac{V_{AC}}{4V_{DC,A}} \tag{D.2}$$

we can determine the signal at each harmonic.

D.1 First harmonic

The first harmonic in eq. (5.13) consists of the terms for which

$$2n - 1 - 2k = \pm 1 \tag{D.3}$$

$$k = n - 1 \text{ or } n = k \tag{D.4}$$

In eq. (5.13), k is summed from 0 to $n-1$ and so per definition $k < n$, leaving only $k = n - 1$ to be considered. Combining eqs. (5.13), (D.2) and (D.4) yields

$$\begin{aligned}\frac{V_{AC,1\omega}}{4V_{DC,A}} &= V\mu_0 d\Bigg(H_0 \sin(A) \\ &\quad + M_S \sum_{n=1}^{\infty} \frac{4 * B_{2n}(CH_0)^{2n-1}}{(2n)!}(-1)^{n-1-(n-1)} \\ &\quad * \binom{2n-1}{n-1} \sin((2n-1-2(n-1))A)\Bigg) \end{aligned} \tag{D.5}$$

$$= V\mu_0 d\Big(H_0 + M_S \sum_{n=1}^{\infty} \frac{4 * B_{2n}(CH_0)^{2n-1}}{(2n)!}\binom{2n-1}{n-1}\Big) \sin(A) \tag{D.6}$$

$$\begin{aligned}&= V\mu_0 d\Big(H_0 \\ &\quad + M_S(\frac{CH_0}{3} - \frac{(CH_0)^3}{60} + \frac{(CH_0)^5}{756} - \frac{(CH_0)^7}{8640} + \dots)\Big) \sin(A)\end{aligned} \tag{D.7}$$

In contrast to dia- and paramagnetic materials, the Faraday rotation detected at the fundamental frequency of the applied magnetic field in a superparamagnetic material is not linear as a function of the applied magnetic field strength. While this provides the ability to distinguish between magnetic characteristics of materials, it is instructive to calculate the expected signal at higher harmonics.

D.2 Third harmonic

The third harmonic in eq. (5.13) consists of the terms for which

$$2n - 1 - 2k = \pm 3 \tag{D.8}$$

$$k = n - 2 \text{ or } k = n + 1 \tag{D.9}$$

Again the second solution is impossible, and furthermore the first solution is only valid for $n \geq 2$. The signal at the third harmonic will be

$$\begin{aligned} \frac{V_{AC,3\omega}}{4V_{DC,A}} &= V\mu_0 dM_S \sum_{n=2}^{\infty} \frac{4 * B_{2n}(CH_0)^{2n-1}}{(2n)!}(-1)^{n-1-(n-2)} \\ &\quad * \binom{2n-1}{n-2} \sin\left((2n - 1 - 2(n-2))A\right) \end{aligned} \tag{D.10}$$

$$= -V\mu_0 dM_S \sum_{n=2}^{\infty} \frac{4 * B_{2n}(CH_0)^{2n-1}}{(2n)!} \binom{2n-1}{n-2} \sin(3A) \tag{D.11}$$

$$\begin{aligned} &= -V\mu_0 dM_S \Big(-\frac{(CH_0)^3}{180} + \frac{(CH_0)^5}{1512} \\ &\quad - \frac{(CH_0)^7}{14400} + \frac{(CH_0)^9}{142560} + \dots \Big) \sin(3A) \end{aligned} \tag{D.12}$$

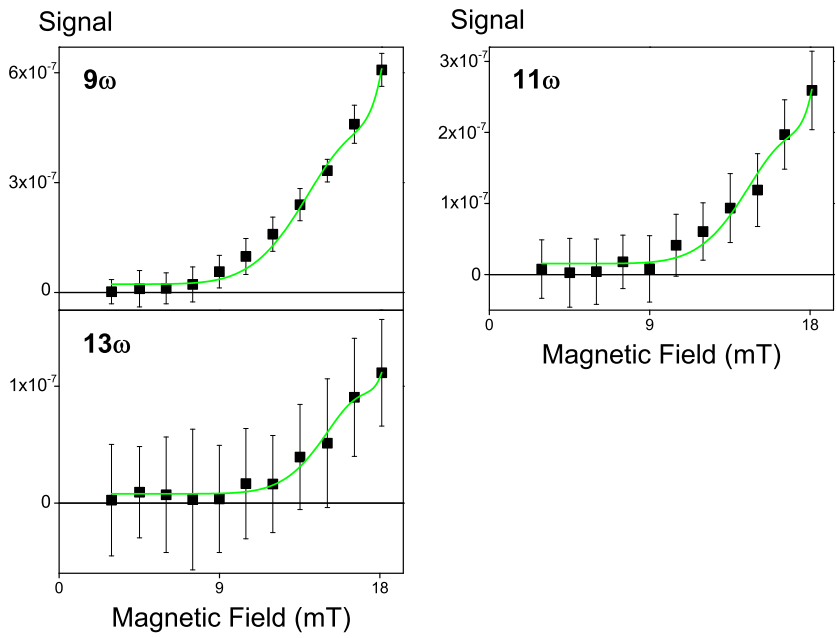

Figure D.1: A clear non-linear dependence is seen for the AC signal of the superparamagnetic nanocomposite divided by DC photodiode voltage as a function of the magnetic field, with higher order harmonics displaying higher order nonlinearities in the magnetic field. Fitting is performed to equations derived from eq. (5.13) (such as eqs. (D.7) and (D.12)), allowing for four magnetic field strength dependent terms per fit.

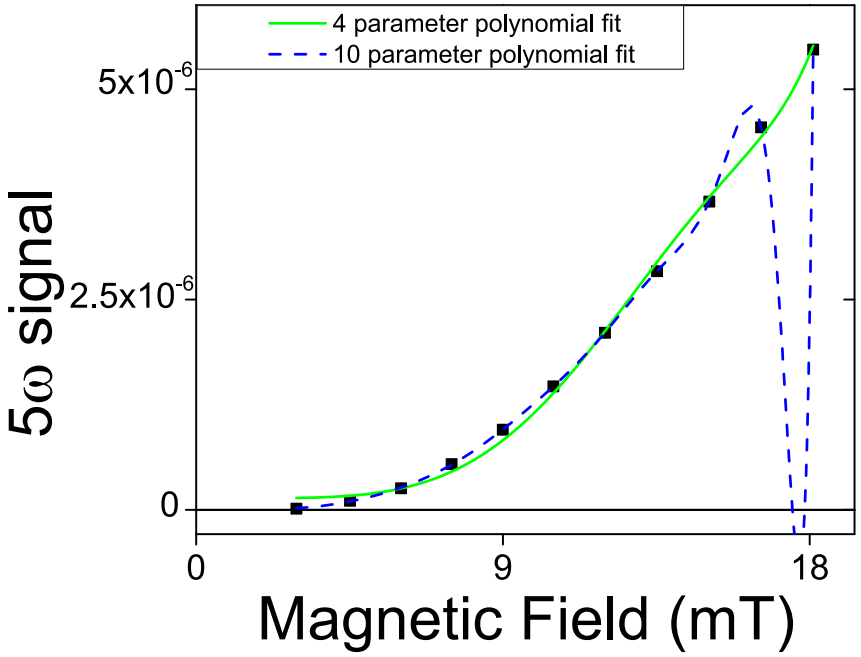

Figure D.2: Using too many terms in the fit to eq. (5.13) attributes too much importance to noise in the data, resulting in incorrect fits.

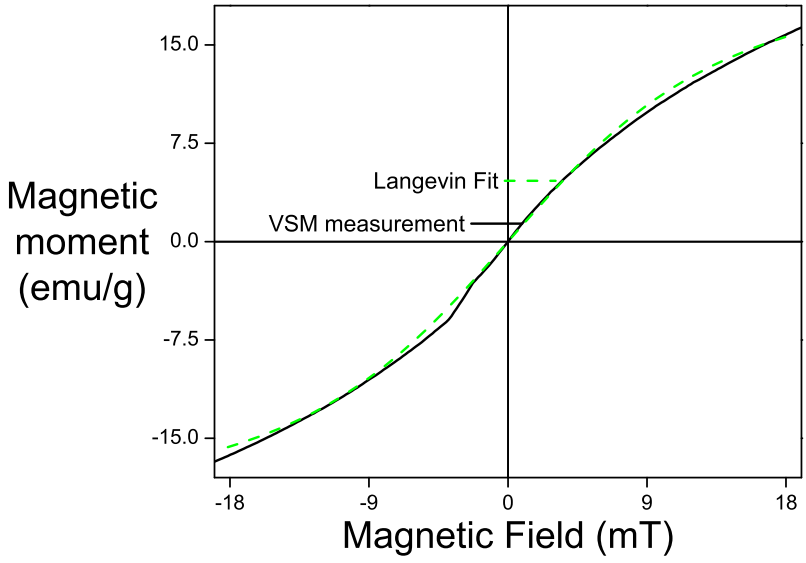

Figure D.3: Superparamagnetic behavior is displayed in the VSM measurement at 300 K of a powder of the iron oxide nanoparticles used in the nanocomposite. A fit to the Langevin equation is shown in green, describing the superparamagnetism well, with minor deviations from the experimental data visible.

Bibliography

[1] R. Fitzpatrick. *Maxwell's Equations and the Principles of Electromagnetism*. Infinity Science Press, 2008. ISBN 9781934015209.

[2] T. Verbiest, K. Clays, and V. Rodriguez. *Second-order Nonlinear Optical Characterization Techniques: An Introduction*. CRC Press, 2009.

[3] P. N. Prasad and D. J. Williams. *Introduction to nonlinear optical effects in molecules and polymers*. Wiley, 1991.

[4] V. A. Margulis, E. E. Muryumin, and E. A. Gaiduk. Large nonlinear optical rectification in atomic hexagonal layers with broken space inversion symmetry. *J. Opt.*, 15(10):105204, 2013.

[5] M. Vanbel, S. Vandendriessche, M. A. van der Veen, D. Slavov, P. Heister, R. Paesen, V. K. Valev, M. Ameloot, and T. Verbiest. Second-harmonic generation from complex chiral samples. In T. N. Dreischuh and A. T. Daskalova, editors, *Proc. SPIE 8770, 17th International School on Quantum Electronics: Laser Physics and Applications, 87701F*, volume 8770, pages 87701F–1–87701F–7. SPIE, 2013.

[6] V. K. Valev, A. V. Silhanek, N. Verellen, W. Gillijns, P. Van Dorpe, O. A. Aktsipetrov, G. A. E. Vandenbosch, V. V. Moshchalkov, and T. Verbiest. Asymmetric Optical Second-Harmonic Generation from Chiral G-Shaped Gold Nanostructures. *Phys. Rev. Lett.*, 104(12):127401, 2010.

[7] L. Zhu and Y. Cui. Influence of microscopic parameters of chiral molecules on the first-order hyperpolarizability. *Opt. Commun.*, 281(1):170–174, 2008.

[8] P. Fischer and F. Hache. Nonlinear optical spectroscopy of chiral molecules. *Chirality*, 17(8):421–437, 2005.

[9] M. K. Vanbel, V. K. Valev, B. Vincent, V. V. Afanas'ev, J.-P. Locquet, S. V. Elshocht, M. Caymax, and T. Verbiest. Second-harmonic generation reveals the oxidation steps in semiconductor processing. *J. Appl. Phys.*,

111(6):064504, 2012.

[10] C. Rotella, S. Napolitano, S. Vandendriessche, V. K. Valev, T. Verbiest, M. Larkowska, S. Kucharski, and M. Wübbenhorst. Adsorption Kinetics of Ultrathin Polymer Films in the Melt Probed by Dielectric Spectroscopy and Second-Harmonic Generation. *Langmuir*, 27(22):13533–13538, 2011.

[11] Y. R. Shen. Surface properties probed by second-harmonic and sum-frequency generation. *Nature*, 337(6207):519–525, 1989.

[12] J. Squier, M. Müller, G. J. Brakenhoff, and K. R. Wilson. Third harmonic generation microscopy. *Opt. Express*, 3(9):315–324, 1998.

[13] D. Débarre, W. Supatto, A.-M. Pena, A. Fabre, T. Tordjmann, L. Combettes, M.-C. Schanne-Klein, and E. Beaurepaire. Imaging lipid bodies in cells and tissues using third-harmonic generation microscopy. *Nat. Methods*, 3(1):47–53, 2006.

[14] Y. Barad, H. Eisenberg, M. Horowitz, and Y. Silberberg. Nonlinear scanning laser microscopy by third harmonic generation. *Appl. Phys. Lett.*, 70(8):922–924, 1997.

[15] D. Nodop, C. Jauregui, D. Schimpf, J. Limpert, and A. Tünnermann. Efficient high-power generation of visible and mid-infrared light by degenerate four-wave-mixing in a large-mode-area photonic-crystal fiber. *Opt. Lett.*, 34(22):3499–3501, 2009.

[16] C. Li, H. Zheng, Y. Zhang, Z. Nie, J. Song, and M. Xiao. Observation of enhancement and suppression in four-wave mixing processes. *Appl. Phys. Lett.*, 95(4):041103, 2009.

[17] M. Faraday. *Experimental Researches in Electricity*, volume III. R. Taylor & W. Francis: London, 1839–1855.

[18] H. Becquerel. Sur une interprétation applicable au phénomène de Faraday et au phénomène de Zeeman. *Comptes rendus*, 125:679–685, 1897.

[19] F. A. Jenkins and H. E. White. *Fundamentals of Optics*. McGraw–Hill, 1976. ISBN 9780070323308.

[20] P. J. Stephens. Dispersion of the Faraday Effect in $CoCl_4^{2-}$. *J. Chem. Phys.*, 43(12):4444–4446, 1965.

[21] A. D. Buckingham and P. J. Stephens. Magnetic Optical Activity. *Annu. Rev. Phys. Chem.*, 17(1):399–432, 1966.

[22] S. Vandendriessche. Design of nanoparticle doped polymer films for giant Faraday rotation. Master's thesis, KU Leuven, 2009–2010.

[23] J. C. Kemp. Piezo-Optical Birefringence Modulators: New Use for a Long-Known Effect. *J. Opt. Soc. Am.*, 59(8):950–953, 1969.

[24] S. Vandendriessche and T. Verbiest. Photoelastic modulator non-idealities in magneto-optical polarization measurements. In J. A. Shaw and D. A. LeMaster, editors, *Proc. SPIE 8873, Polarization Science and Remote Sensing VI, 88730Z*, volume 8873, pages 88730Z–1–88730Z–11. SPIE, 2013.

[25] A. Jain, J. Kumar, F. Zhou, and L. Li. A simple experiment for determining Verdet constants using alternating current magnetic fields. *Am. J. Phys.*, 67 (8):714–717, 1999.

[26] V. K. Valev, J. Wouters, and T. Verbiest. Differential detection for measurements of Faraday rotation by means of ac magnetic fields. *Eur. J. Phys.*, 29(5):1099, 2008.

[27] V. K. Valev, J. Wouters, and T. Verbiest. Precise measurements of Faraday rotation using ac magnetic fields. *Am. J. Phys.*, 76(7):626–629, 2008.

[28] K. B. Wiberg. Basis set effects on calculated geometries: 6-311++G** vs. aug-cc-pVDZ. *J. Comput. Chem.*, 25(11):1342–1346, 2004.

[29] A. Banerjee, J. Autschbach, and T. Ziegler. A gauge-origin independent expression for the Verdet constant within the time-dependent density functional theory. *Int. J. Quantum Chem.*, 101(5):572–578, 2005.

[30] D. M. Bishop and S. M. Cybulski. Magnetic optical rotation in H_2 and D_2. *J. Chem. Phys.*, 93(1):590–599, 1990.

[31] W. A. Parkinson, S. P. A. Sauer, J. Oddershede, and D. M. Bishop. Calculation of the Verdet constants for H_2, N_2, CO, and FH. *J. Chem. Phys.*, 98(1):487–495, 1993.

[32] S. Coriani, P. Jørgensen, O. Christiansen, and J. Gauss. Triple excitation effects in coupled cluster calculations of Verdet constants. *Chem. Phys. Lett.*, 330(3–4):463–470, 2000.

[33] M. Krykunov, A. Banerjee, T. Ziegler, and J. Autschbach. Calculation of Verdet constants with time-dependent density functional theory: Implementation and results for small molecules. *J. Chem. Phys.*, 122(7): 074105, 2005.

[34] J. Olsen and P. Jørgensen. Linear and nonlinear response functions for an exact state and for an MCSCF state. *J. Chem. Phys.*, 82(7), 1985.

[35] K. Aidas, C. Angeli, K. L. Bak, V. Bakken, R. Bast, L. Boman, O. Christiansen, R. Cimiraglia, S. Coriani, P. Dahle, E. K. Dalskov, U. Ekström, T. Enevoldsen, J. J. Eriksen, P. Ettenhuber, B. Fernández, L. Ferrighi, H. Fliegl, L. Frediani, K. Hald, A. Halkier, C. Hättig, H. Heiberg, T. Helgaker, A. C. Hennum, H. Hettema, E. Hjertenæs,

S. Høst, I.-M. Høyvik, M. F. Iozzi, B. Jansík, H. J. A. Jensen, D. Jonsson, P. Jørgensen, J. Kauczor, S. Kirpekar, T. Kjærgaard, W. Klopper, S. Knecht, R. Kobayashi, H. Koch, J. Kongsted, A. Krapp, K. Kristensen, A. Ligabue, O. B. Lutnæs, J. I. Melo, K. V. Mikkelsen, R. H. Myhre, C. Neiss, C. B. Nielsen, P. Norman, J. Olsen, J. M. H. Olsen, A. Osted, M. J. Packer, F. Pawlowski, T. B. Pedersen, P. F. Provasi, S. Reine, Z. Rinkevicius, T. A. Ruden, K. Ruud, V. V. Rybkin, P. Sałek, C. C. M. Samson, A. S. de Merás, T. Saue, S. P. A. Sauer, B. Schimmelpfennig, K. Sneskov, A. H. Steindal, K. O. Sylvester-Hvid, P. R. Taylor, A. M. Teale, E. I. Tellgren, D. P. Tew, A. J. Thorvaldsen, L. Thøgersen, O. Vahtras, M. A. Watson, D. J. D. Wilson, M. Ziolkowski, and H. Ågren. The Dalton quantum chemistry program system. *Wiley Interdiscip. Rev.: Comput. Mol. Sci.*, 2013.

[36] E. M. Cohn and M. Mentser. The cgs Units of Magnetic Susceptibility and Specific Magnetization. *Am. J. Phys.*, 21(9):681–682, 1953.

[37] Y. Liu, D. J. Sellmyer, and D. Shindo. *Handbook of Advanced Magnetic Materials*. Springer, 2006. ISBN 9781402079832.

[38] Y. Zhu. *Modern Techniques for Characterizing Magnetic Materials*. Springer, 2005. ISBN 9781402080074.

[39] J. W. Thompson, H. A. Stretz, P. E. Arce, H. Gao, H. J. Ploehn, and J. He. Effect of magnetization on the gel structure and protein electrophoresis in polyacrylamide hydrogel nanocomposites. *J. Appl. Polym. Sci.*, 126(5): 1600–1612, 2012.

[40] L. Husáriková, Z. Repická, D. Valigura, M. Valko, and M. Mazúr. 3-Pyridylmethanol vs. *N*,*N*'-diethylnicotinamide in copper(II) complex formation – A comparative EPR study. *J. Mol. Struct.*, 1049:41–47, 2013.

[41] J. Ma, J. Hu, Z. Li, and C.-W. Nan. Recent Progress in Multiferroic Magnetoelectric Composites: from Bulk to Thin Films. *Adv. Mater.*, 23 (9):1062–1087, 2011.

[42] S. Bedanta and W. Kleemann. Supermagnetism. *J. Phys. D: Appl. Phys.*, 42(1):013001, 2009.

[43] M. Knobel, W. C. Nunes, L. M. Socolovsky, E. De Biasi, J. M. Vargas, and J. C. Denardin. Superparamagnetism and Other Magnetic Features in Granular Materials: A Review on Ideal and Real Systems. *J. Nanosci. Nanotechno.*, 8(6):2836–2857, 2008.

[44] U. Jeong, X. Teng, Y. Wang, H. Yang, and Y. Xia. Superparamagnetic Colloids: Controlled Synthesis and Niche Applications. *Adv. Mater.*, 19 (1):33–60, 2007.

[45] W. Brullot, N. K. Reddy, J. Wouters, V. K. Valev, B. Goderis, J. Vermant, and T. Verbiest. Versatile ferrofluids based on polyethylene glycol coated iron oxide nanoparticles. *J. Magn. Magn. Mater.*, 324(11):1919–1925, 2012.

[46] M. Bloemen, W. Brullot, T. Luong, N. Geukens, A. Gils, and T. Verbiest. Improved functionalization of oleic acid-coated iron oxide nanoparticles for biomedical applications. *J. Nanopart. Res.*, 14(9):1–10, 2012.

[47] S. Behrens. Preparation of functional magnetic nanocomposites and hybrid materials: recent progress and future directions. *Nanoscale*, 3(3): 877–892, 2011.

[48] X.-X. Zhang, J. Schoenes, W. Reim, and P. Wachter. Evidence for $3d^n$ to $3d^{n-1}4s$ transitions in magnetite and in lithium and magnesium ferrites. *J. Phys. C: Solid State*, 16(31):6055–6072, 1983.

[49] Y. A. Barnakov, B. L. Scott, V. Golub, L. Kelly, V. Reddy, and K. L. Stokes. Spectral dependence of Faraday rotation in magnetite–polymer nanocomposites. *J. Phys. Chem. Solids*, 65(5):1005–1010, 2004.

[50] W. F. J. Fontijn, P. J. van der Zaag, M. A. C. Devillers, V. A. M. Brabers, and R. Metselaar. Optical and magneto-optical polar Kerr spectra of Fe_3O_4 and Mg^{2+}- or Al^{3+}-substituted Fe_3O_4. *Phys. Rev. B*, 56(9):5432–5442, 1997.

[51] T. Tepper, F. Ilievski, C. A. Ross, T. R. Zaman, R. J. Ram, S. Y. Sung, and B. J. H. Stadler. Magneto-optical properties of iron oxide films. *J. Appl. Phys.*, 93(10):6948–6950, 2003.

[52] S. W. Hawking, G. W. Gibbons, E. P. S. Shellard, and S. J. Rankin. *The Future of Theoretical Physics and Cosmology: Celebrating Stephen Hawking's Contributions to Physics*. Cambridge University Press, 2003. ISBN 9780521820813.

[53] M. Xiong, J. A. Davies, X. Feng, M. J. Owens, R. A. Harrison, C. J. Davis, and Y. D. Liu. Using Coordinated Observations in Polarized White Light and Faraday Rotation to Probe the Spatial Position and Magnetic Field of an Interplanetary Sheath. *Astrophys J.*, 777(1):32, 2013.

[54] N. Behbood, F. Martin Ciurana, G. Colangelo, M. Napolitano, M. W. Mitchell, and R. J. Sewell. Real-time vector field tracking with a cold-atom magnetometer. *Appl. Phys. Lett.*, 102(17):173504, 2013.

[55] C. Johnson, P. D. D. Schwindt, and M. Weisend. Magnetoencephalography with a two-color pump-probe, fiber-coupled atomic magnetometer. *Appl. Phys. Lett.*, 97(24):243703, 2010.

[56] L. Sun, S. Jiang, and J. R. Marciante. Compact all-fiber optical Faraday

components using 65-wt%-terbium-doped fiber with a record Verdet constant of −32rad/(Tm). *Opt. Express*, 18(12):12191–12196, 2010.

[57] H. Dötsch, N. Bahlmann, O. Zhuromskyy, M. Hammer, L. Wilkens, R. Gerhardt, P. Hertel, and A. F. Popkov. Applications of magneto-optical waveguides in integrated optics: review. *J. Opt. Soc. Am. B*, 22 (1):240–253, 2005.

[58] E. Khazanov, N. F. Andreev, A. Mal'shakov, O. Palashov, A. K. Poteomkin, A. Sergeev, A. A. Shaykin, V. Zelenogorsky, I. A. Ivanov, R. Amin, G. Mueller, D. B. Tanner, and D. H. Reitze. Compensation of thermally induced modal distortions in Faraday isolators. *IEEE J. Quantum Elect.*, 40(10):1500–1510, 2004.

[59] G. W. Day, D. N. Payne, A. J. Barlow, and J. J. Ramskov-Hansen. Faraday rotation in coiled, monomode optical fibers: isolators, filters, and magnetic sensors. *Opt. Lett.*, 7(5):238–240, 1982.

[60] The Virgo Collaboration. In-vacuum Faraday isolation remote tuning. *Appl. Opt.*, 49(25):4780–4790, 2010.

[61] E. A. Mironov, I. L. Snetkov, A. V. Voitovich, and O. V. Palashov. Permanent-magnet Faraday isolator with the field intensity of 25kOe. *Quantum Electron.*, 43(8):740, 2013.

[62] W. A. Crossley, R. W. Cooper, J. L. Page, and R. P. van Stapele. Faraday Rotation in Rare-Earth Iron Garnets. *Phys. Rev.*, 181(2), 1969.

[63] I. Edelman and J. Kliava. Oxide glasses with magnetic nanoparticles: transparent magnets (Faraday rotation and electron magnetic resonance studies). *Phys. Status Solidi B*, 246(10):2216–2231, 2009.

[64] G. T. Petrovskii, I. S. Edelman, T. V. Zarubina, A. V. Malakhovskii, V. N. Zabluda, and M. Y. Ivanov. Faraday effect and spectral properties of high-concentrated rare earth oxide glasses in visible and near UV region. *J. Non-Cryst. Solids*, 130(1):35–40, 1991.

[65] H. Akamatsu, K. Fujita, S. Murai, and K. Tanaka. Magneto-optical properties of transparent divalent iron phosphate glasses. *Appl. Phys. Lett.*, 92(25):251908, 2008.

[66] E. Botek, B. Champagne, T. Verbiest, P. Gangopadhyay, and A. Persoons. A Joint Theoretical–Experimental Investigation of the Faraday Effect in Benzene, Toluene, and *p*-Xylene. *ChemPhysChem*, 7(8):1654–1656, 2006.

[67] M. Suwa, K. Miyamoto, and H. Watarai. Faraday Rotation Dispersion Measurements of Diamagnetic Organic Liquids and Simultaneous Determination of Natural Optical Rotatory Dispersion Using a Pulsed Magnetic Field. *Anal. Sci.*, 29(1):113–119, 2013.

[68] P. Gangopadhyay, R. Voorakaranam, A. Lopez-Santiago, S. Foerier, J. Thomas, R. A. Norwood, A. Persoons, and N. Peyghambarian. Faraday Rotation Measurements on Thin Films of Regioregular Alkyl-Substituted Polythiophene Derivatives. *J. Phys. Chem. C*, 112(21):8032–8037, 2008.

[69] I. Crassee, J. Levallois, A. L. Walter, M. Ostler, A. Bostwick, E. Rotenberg, T. Seyller, D. van der Marel, and A. B. Kuzmenko. Giant Faraday rotation in single- and multilayer graphene. *Nat. Phys.*, 7(1):48–51, 2011.

[70] M. Tymchenko, A. Y. Nikitin, and L. Martín-Moreno. Faraday Rotation Due to Excitation of Magnetoplasmons in Graphene Microribbons. *ACS Nano*, 7(11):9780–9787, 2013.

[71] N. Bloembergen and P. S. Pershan. Light Waves at the Boundary of Nonlinear Media. *Phys. Rev.*, 128:606–622, 1962.

[72] V. Rodriguez, G. Koeckelberghs, and T. Verbiest. Second-harmonic generation-circular dichroism in thin films of a chiral poly(3-alkyl)thiophene. *Chem. Phys. Lett.*, 450(1-3):76–79, 2007.

[73] S. Sioncke, T. Verbiest, and A. Persoons. Second-order nonlinear optical properties of chiral materials. *Mat. Sci. Eng. R–Rep.*, 42(5–6):115–155, 2003.

[74] D. S. Jordan, C. J. Hull, J. M. Troiano, S. C. Riha, A. B. F. Martinson, K. M. Rosso, and F. M. Geiger. Second Harmonic Generation Studies of Fe(II) Interactions with Hematite (α-Fe_2O_3). *J. Phys. Chem. C*, 117(8): 4040–4047, 2013.

[75] V. K. Valev, M. K. Vanbel, B. Vincent, V. V. Moshchalkov, M. Caymax, and T. Verbiest. Second Harmonic Generation Indicates a Better Si/Ge Interface Quality for Higher Temperature and With N_2 Rather Than With H_2 as the Carrier Gas. *IEEE Electr. Devic. L.*, 32(1):12–14, 2011.

[76] S. Vandendriessche, V. K. Valev, and T. Verbiest. Characterization of magnetization-induced second harmonic generation in iron oxide polymer nanocomposites. *Appl. Opt.*, 51(2):209–213, 2012.

[77] P. A. Franken, A. E. Hill, C. W. Peters, and G. Weinreich. Generation of Optical Harmonics. *Phys. Rev. Lett.*, 7(4):118–119, 1961.

[78] J. Jerphagnon and S. K. Kurtz. Optical Nonlinear Susceptibilities: Accurate Relative Values for Quartz, Ammonium Dihydrogen Phosphate, and Potassium Dihydrogen Phosphate. *Phys. Rev. B*, 1(4):1739–1744, 1970.

[79] R. A. Myers, N. Mukherjee, and S. R. J. Brueck. Large second-order nonlinearity in poled fused silica. *Opt. Lett.*, 16(22):1732–1734, 1991.

[80] D. M. Burland, R. D. Miller, and C. A. Walsh. Second-order nonlinearity in poled-polymer systems. *Chem. Rev.*, 94(1):31–75, 1994.

[81] G. Pawlik, I. Rau, F. Kajzar, and A. C. Mitus. Second-harmonic generation in poled polymers: pre-poling history paradigm. *Opt. Express*, 18(18): 18793–18804, 2010.

[82] M. Y. Song, B. Jeon, H. J. Kim, and J.-Y. Lee. The design, synthesis, and nonlinear optical properties of novel X-type polyurethane containing dicyanovinylnitroresorcinoxy group with enhanced shg thermal stability. *J. Polym. Sci. A1*, 51(2):275–281, 2013.

[83] M. Y. Song, M. S. Kim, B. Jeon, and J.-Y. Lee. Synthesis and Properties of Novel Nonlinear Optical Polyurethane Containing Nitrophenylazocatecholic Group. *Mol. Cryst. Liq. Cryst.*, 568(1):98–104, 2012.

[84] Y. Zhang, J. Ortega, U. Baumeister, C. L. Folcia, G. Sanz-Enguita, C. Walker, S. Rodriguez-Conde, J. Etxebarria, M. J. O'Callaghan, and K. More. An Azo-Bridged Ferroelectric Liquid Crystal with Highly Enhanced Second and Third Harmonic Generation. *J. Am. Chem. Soc.*, 134(39):16298–16306, 2012.

[85] M. S. Kim, M. Y. Song, B. Jeon, and J.-Y. Lee. Synthesis and electro-optic properties of novel polyurethane containing the nitrophenylazoresorcinoxy group. *Polym. Int.*, 61(12):1739–1744, 2012.

[86] Z. Li, W. Wu, C. Ye, J. Qin, and Z. Li. New main-chain hyperbranched polymers: Facile synthesis, structural control, and second-order nonlinear optical properties. *Polymer*, 53(1):153–160, 2012.

[87] M. J. Huttunen, O. Herranen, A. Johansson, H. Jiang, P. R. Mudimela, P. Myllyperkiö, G. Bautista, A. G. Nasibulin, E. I. Kauppinen, M. Ahlskog, M. Kauranen, and M. Pettersson. Measurement of optical second-harmonic generation from an individual single-walled carbon nanotube. *New J. Phys.*, 15(8):083043, 2013.

[88] P. C. Ray. Size and Shape Dependent Second Order Nonlinear Optical Properties of Nanomaterials and Their Application in Biological and Chemical Sensing. *Chem. Rev.*, 110(9):5332–5365, 2010.

[89] M. M. Villa, L. Wang, J. Huang, D. W. Rowe, and M. Wei. Visualizing Osteogenesis *In Vivo* Within a Cell–Scaffold Construct for Bone Tissue Engineering Using Two-Photon Microscopy. *Tissue Eng. Pt. C-Meth.*, 19 (11):839–849, 2013.

[90] J. E. Reeve, A. D. Corbett, I. Boczarow, W. Kaluza, W. Barford, H. Bayley, T. Wilson, and H. L. Anderson. Porphyrins for Probing Electrical Potential

Across Lipid Bilayer Membranes by Second Harmonic Generation. *Angew. Chem. Int. Ed.*, 52(34):9044–9048, 2013.

[91] V. K. Valev, B. De Clercq, C. G. Biris, X. Zheng, S. Vandendriessche, M. Hojeij, D. Denkova, Y. Jeyaram, N. C. Panoiu, Y. Ekinci, A. V. Silhanek, V. Volskiy, G. A. E. Vandenbosch, M. Ameloot, V. V. Moshchalkov, and T. Verbiest. Distributing the Optical Near-Field for Efficient Field-Enhancements in Nanostructures. *Adv. Opt. Mater.*, 24 (35):OP208–OP215, 2012.

[92] T. Schneider. *Nonlinear Optics in Telecommunications*. Advanced Texts in Physics. Springer, 2004. ISBN 9783540201953.

[93] X. Wei, Y. Peng, W. Wang, X. Chen, and D. Li. High-efficiency mid-infrared laser from synchronous optical parametric oscillation and amplification based on a single MgO:PPLN crystal. *Appl. Phys. B-Lasers O.*, 104(3):597–601, 2011.

[94] M. Kauranen, T. Verbiest, S. Van Elshocht, and A. Persoons. Chirality in surface nonlinear optics. *Opt. Mater.*, 9(1–4):286–294, 1998.

[95] M. A. van der Veen, F. Vermoortele, D. E. De Vos, and T. Verbiest. Point Group Symmetry Determination via Observables Revealed by Polarized Second-Harmonic Generation Microscopy: (1) Theory. *Anal. Chem.*, 84 (15):6378–6385, 2012.

[96] V. Ostroverkhov, O. Ostroverkhova, R. G. Petschek, K. D. Singer, L. Sukhomlinova, and R. J. Twieg. Prospects for chiral nonlinear optical media. *IEEE J. Sel. Top. Quant.*, 7(5):781–792, 2001.

[97] S. Van Cleuvenbergen, G. Hennrich, P. Willot, G. Koeckelberghs, K. Clays, T. Verbiest, and M. A. van der Veen. All Optical Determination of Microscopic and Macroscopic Structure of Chiral, Polar Microcrystals from Achiral, Nonpolar Molecules. *J. Phys. Chem. C*, 116(22):12219–12225, 2012.

[98] M. Fiebig, V. V. Pavlov, and R. V. Pisarev. Second-harmonic generation as a tool for studying electronic and magnetic structures of crystals: review. *J. Opt. Soc. Am. B*, 22(1):96–118, 2005.

[99] J. D. Morris, T. L. Atallah, H. Park, Z. Ooi, A. Dodabalapur, and X.-Y. Zhu. Quantifying space charge accumulation in organic bulk heterojunctions by nonlinear optical microscopy. *Org. Electron.*, 14(11): 3014–3018, 2013.

[100] J. Lin, S. Pan, W. Zheng, and Z. Huang. Polarization-resolved second-harmonic generation imaging for liver fibrosis assessment without labeling. *Appl. Phys. Lett.*, 103(17):173701, 2013.

[101] V. K. Valev, A. V. Silhanek, W. Gillijns, Y. Jeyaram, H. Paddubrouskaya, A. Volodin, C. G. Biris, N. C. Panoiu, B. De Clercq, M. Ameloot, O. A. Aktsipetrov, V. V. Moshchalkov, and T. Verbiest. Plasmons Reveal the Direction of Magnetization in Nickel Nanostructures. *ACS Nano*, 5(1): 91–96, 2010.

[102] J. F. McGilp, L. Carroll, K. Fleischer, J. P. Cunniffe, and S. Ryan. Magnetic second-harmonic generation from interfaces and nanostructures. *J. Magn. Magn. Mater.*, 322(9–12):1488–1493, 2010.

[103] Y. F. Chiang, Y. J. Hsu, T. M. Liu, H. W. Chu, J. G. Lin, C. H. Chen, and Y.-M. Chang. Magnetization reversal process of ferromagnetic granular thin films probed by magnetization-induced second harmonic generation. *Appl. Phys. Lett.*, 95(17):172515, 2009.

[104] J. Reif, J. C. Zink, C.-M. Schneider, and J. Kirschner. Effects of surface magnetism on optical second harmonic generation. *Phys. Rev. Lett.*, 67 (20):2878–2881, 1991.

[105] G. Spierings, V. Koutsos, H. A. Wierenga, M. W. J. Prins, D. Abraham, and T. Rasing. Optical second harmonic generation study of interface magnetism. *Surf. Sci.*, 287–288(2):747–749, 1993.

[106] T. Rasing. Nonlinear magneto-optics. *J. Magn. Magn. Mater.*, 175(1–2): 35–50, 1997.

[107] C. Train, M. Gruselle, and M. Verdaguer. The fruitful introduction of chirality and control of absolute configurations in molecular magnets. *Chem. Soc. Rev.*, 40:3297–3312, 2011.

[108] C. Train, T. Nuida, R. Gheorghe, M. Gruselle, and S. I. Ohkoshi. Large Magnetization-Induced Second Harmonic Generation in an Enantiopure Chiral Magnet. *J. Am. Chem. Soc.*, 131(46):16838–16843, 2009.

[109] X. Liu, J. Gu, R. Singh, Y. Ma, J. Zhu, Z. Tian, M. He, J. Han, and W. Zhang. Electromagnetically induced transparency in terahertz plasmonic metamaterials via dual excitation pathways of the dark mode. *Appl. Phys. Lett.*, 100(13):131101, 2012.

[110] H. A. Wierenga, M. W. J. Prins, D. L. Abraham, and T. Rasing. Magnetization-induced optical second-harmonic generation: A probe for interface magnetism. *Phys. Rev. B*, 50(2):1282–1285, 1994.

[111] C. Lacroix, P. Mendels, and F. Mila. *Introduction to Frustrated Magnetism: Materials, Experiments, Theory*. Solidstate Sciences. Springer, 2011. ISBN 9783642105890.

[112] E. Hecht. *Optics*. Pearson Education, 2008. ISBN 9788131718070.

[113] P. Ginzburg, F. J. Rodríguez Fortuño, G. A. Wurtz, W. Dickson,

A. Murphy, F. Morgan, R. J. Pollard, I. Iorsh, A. Atrashchenko, P. A. Belov, Y. S. Kivshar, A. Nevet, G. Ankonina, M. Orenstein, and A. V. Zayats. Manipulating polarization of light with ultrathin epsilon-near-zero metamaterials. *Opt. Express*, 21(12):14907–14917, 2013.

[114] Y. Zhao and A. Alù. Manipulating light polarization with ultrathin plasmonic metasurfaces. *Phys. Rev. B*, 84(20):205428, 2011.

[115] M. Kauranen, S. Van Elshocht, T. Verbiest, and A. Persoons. Tensor analysis of the second-order nonlinear optical susceptibility of chiral anisotropic thin films. *J. Chem. Phys.*, 112(3):1497–1502, 2000.

[116] S. Kleinlogel and A. G. White. The Secret World of Shrimps: Polarisation Vision at Its Best. *PLoS ONE*, 3(5):e2190 EP, 2008.

[117] M. Vedel, N. Lechocinski, and S. Breugnot. 3D shape reconstruction of optical element using polarization. In D. B. Chenault and D. H. Goldstein, editors, *Polarization: Measurement, Analysis, and Remote Sensing IX, 767203*, page 767203. SPIE, 2010.

[118] B. Cohen, C. Martin, S. K. Iyer, U. Wiesner, and A. Douhal. Single Dye Molecule Behavior in Fluorescent Core–Shell Silica Nanoparticles. *Chem. Mater.*, 24(2):361–372, 2011.

[119] V. J. lafelice and W. S. Bickel. Polarized light-scattering matrix elements for select perfect and perturbed optical surfaces. *Appl. Opt.*, 26(12): 2410–2415, 1987.

[120] C.-S. Guo, S.-J. Yue, X.-L. Wang, J. Ding, and H.-T. Wang. Polarization-selective diffractive optical elements with a twisted-nematic liquid-crystal display. *Appl. Opt.*, 49(7):1069–1074, 2010.

[121] E. Hasman, V. Kleiner, G. Biener, and A. Niv. Polarization dependent focusing lens by use of quantized Pancharatnam–Berry phase diffractive optics. *Appl. Phys. Lett.*, 82(3):328–330, 2003.

[122] D. Yang, J. C. Canit, and E. Gaignebet. Photoelastic modulator: polarization modulation and phase modulation. *J. Opt.*, 26(4):151, 1995.

[123] S. A. Hall, P. A. Covert, B. R. Blinn, S. Shakeri, and D. K. Hore. Rapid and Sensitive Polarization Measurement for Characterizing Protein Adsorption at the Solid–Liquid Interface. *J. Phys. Chem. C*, 117(4):1796–1803, 2013.

[124] O. Núñez-Olvera, R. E. Balderas-Navarro, J. Ortega-Gallegos, L. E. Guevara-Macías, A. Armenta-Franco, M. A. Lastras-Montaño, L. F. Lastras-Martínez, and A. Lastras-Martínez. A rapid reflectance-difference spectrometer for real-time semiconductor growth monitoring with sub-second time resolution. *Rev. Sci. Instrum.*, 83(10):103109, 2012.

[125] A. D. L. Chandani, A. Fukuda, S. Kumar, and J. K. Vij. Discovery of

a novel ferrielectric phase of five-layer periodicity in binary mixtures of chiral smectic liquid crystals exhibiting unusual reversed phase sequence. *Liq. Cryst.*, 38(5):663–668, 2011.

[126] M. Maisonneuve, I.-H. Song, S. Patskovsky, and M. Meunier. Polarimetric total *internal reflection* biosensing. *Opt. Express*, 19(8):7410–7416, 2011.

[127] C.-Y. Han, C.-W. Lai, Y.-F. Chao, K.-C. Leou, and T.-L. Lin. Assessment of interface roughness during plasma etching through the use of real-time ellipsometry. *Appl. Surf. Sci.*, 257(7):2536–2539, 2011.

[128] M.-H. Kim, V. Kurz, G. Acbas, C. T. Ellis, and J. Cerne. Measurement of the infrared complex Faraday angle in semiconductors and insulators. *J. Opt. Soc. Am. B*, 28(2):199–207, 2011.

[129] E. Roedel, A. Urakawa, and A. Baiker. *In situ* PM-IRRAS study of powder catalyst: Dynamic evolutions of species on catalyst and in gas phase during NO_x storage-reduction. *Catal. Today*, 155(3–4):172–176, 2010.

[130] S. Vandendriessche, S. Van Cleuvenbergen, P. Willot, G. Hennrich, M. Srebro, V. K. Valev, G. Koeckelberghs, K. Clays, J. Autschbach, and T. Verbiest. Giant Faraday Rotation in Mesogenic Organic Molecules. *Chem. Mater.*, 25(7):1139–1143, 2013.

[131] P. J. Cook, J. Zhang, Y. Liu, W. Guan, N. Wang, L. Qin, T. H. Shen, G. A. Jones, and P. J. Grundy. Magneto-Optical Stokes Polarimetry and Nanostructured Magnetic Materials. *J. Nanosci. Nanotechno.*, 12(2): 1067–1073, 2012.

[132] A. Joshua and V. Venkataraman. Enhanced sensitivity in detection of Kerr rotation by double modulation and time averaging based on Allan variance. *Rev. Sci. Instrum.*, 80(2):023908, 2009.

[133] T. K. Xia, P. M. Hui, and D. Stroud. Theory of Faraday rotation in granular magnetic materials. *J. Appl. Phys.*, 67(6):2736–2741, 1990.

[134] J. Y. Chin, T. Steinle, T. Wehlus, D. Dregely, T. Weiss, V. I. Belotelov, B. Stritzker, and H. Giessen. Nonreciprocal plasmonics enables giant enhancement of thin-film Faraday rotation. *Nat. Commun.*, 4:1599, 2013.

[135] S. Vandendriessche, V. K. Valev, and T. Verbiest. Faraday rotation and its dispersion in the visible region for saturated organic liquids. *Phys. Chem. Chem. Phys.*, 14:1860–1864, 2012.

[136] J. M. Bradley, J. N. Butt, and M. R. Cheesman. Electrochemical titrations and reaction time courses monitored in situ by magnetic circular dichroism spectroscopy. *Anal. Biochem.*, 419(2):110–116, 2011.

[137] G. H. Wagnière and G. L. J. A. Rikken. Chirality and magnetism: Free

electron on an infinite helix, NCD, MCD, and magnetochiral dichroism. *Chem. Phys. Lett.*, 481(4–6):166–168, 2009.

[138] T. Kjærgaard, K. Kristensen, J. Kauczor, P. Jørgensen, S. Coriani, and A. J. Thorvaldsen. Comparison of standard and damped response formulations of magnetic circular dichroism. *J. Chem. Phys.*, 135(2): 024112–16, 2011.

[139] S. C. Bera and S. Chakraborty. Study of magneto-optic element as a displacement sensor. *Measurement*, 44(9):1747–1752, 2011.

[140] J. Nelissen, K. Nuyts, M. De Zotti, R. Lavigne, C. Lamberigts, and W. M. De Borggraeve. Total Synthesis of Septocylindrin B and C-Terminus Modified Analogues. *PLoS ONE*, 7(12):e51708, 2012.

[141] M. Farrag, M. Tschurl, and U. Heiz. Chiral Gold and Silver Nanoclusters: Preparation, Size Selection, and Chiroptical Properties. *Chem. Mater.*, 25(6):862–870, 2013.

[142] Y. Gu and K. G. Kornev. Plasmon enhanced direct and inverse Faraday effects in non-magnetic nanocomposites. *J. Opt. Soc. Am. B*, 27(11): 2165–2173, 2010.

[143] H. Jans, K. Jans, P.-J. Demeyer, K. Knez, T. Stakenborg, G. Maes, and L. Lagae. A simple double-bead sandwich assay for protein detection in serum using UV–vis spectroscopy. *Talanta*, 83(5):1580–1585, 2011.

[144] W. Sempels, R. De Dier, H. Mizuno, J. Hofkens, and J. Vermant. Auto-production of biosurfactants reverses the coffee ring effect in a bacterial system. *Nat. Commun.*, 4:1757, 2013.

[145] M. Bloemen, W. Brullot, C. Denis, L. Vanysacker, and T. Verbiest. Core–shell nanoparticles as enhanced probes for imaging applications. In J. Popp, W. Drexler, V. V. Tuchin, and D. L. Matthews, editors, *Biophotonics: Photonic Solutions for Better Health Care III*, page 84272Q, 2012.

[146] P. J. Demeyer, M. Bloemen, T. Verbiest, and K. Clays. Tuning the properties of colloidal magneto-photonic crystals by controlled infiltration with superparamagnetic magnetite nanoparticles. In H. R. Míguez, S. G. Romanov, L. C. Andreani, and C. Seassal, editors, *Photonic Crystal Materials and Devices X*, pages 84251R–1–84251R–7. SPIE, 2012.

[147] E. Castiglioni, P. Albertini, and S. Abbate. Evaluation of instrumental errors built in circular dichroism spectrometers. *Chirality*, 22(1E):E142–E148, 2010.

[148] H. Takechi, O. Arteaga, J. M. Ribo, and H. Watarai. Chiroptical Measurement of Chiral Aggregates at Liquid–Liquid Interface in Centrifugal Liquid Membrane Cell by Mueller Matrix and Conventional

Circular Dichroism Methods. *Molecules*, 16(5):3636–3647, 2011.

[149] O. Arteaga and A. Canillas. Pseudopolar decomposition of the Jones and Mueller-Jones exponential polarization matrices. *J. Opt. Soc. Am. A*, 26 (4):783–793, 2009.

[150] C. G. Hu, L. D. Sun, Y. N. Li, M. Hohage, J. M. Flores-Camacho, X. T. Hu, and P. Zeppenfeld. Retardation correction for photoelastic modulator-based multichannel reflectance difference spectroscopy. *J. Opt. Soc. Am. A*, 25(6):1240–1245, 2008.

[151] N. Ghosh, M. F. G. Wood, and I. A. Vitkin. Mueller matrix decomposition for extraction of individual polarization parameters from complex turbid media exhibiting multiple scattering, optical activity, and linear birefringence. *J. Biomed. Opt.*, 13(4):044036, 2008.

[152] W. S. Bickel and W. M. Bailey. Stokes vectors, Mueller matrices, and polarized scattered light. *Am. J. Phys.*, 53(5):468–478, 1985.

[153] H. G. Tompkins and E. A. Irene. *Handbook of ellipsometry*. William Andrew Pub., 2005. ISBN 9783540222934.

[154] B. A. Wallace and R. W. Janes. *Modern Techniques for Circular Dichroism and Synchrotron Radiation Circular Dichroism Spectroscopy*. IOS Press, 2009. ISBN 9781607500001.

[155] G. E. Jellison and F. A. Modine. Two-modulator generalized ellipsometry: experiment and calibration. *Appl. Opt.*, 36(31):8184–8189, 1997.

[156] D. Budker, D. F. Kimball, S. M. Rochester, V. V. Yashchuk, and M. Zolotorev. Sensitive magnetometry based on nonlinear magneto-optical rotation. *Phys. Rev. A*, 62(4):043403, 2000.

[157] P. Jørgensen, J. Oddershede, and N. H. F. Beebe. Polarization propagator calculations of frequency-dependent polarizabilities, Verdet constants, and energy weighted sum rules. *J. Chem. Phys.*, 68(6):2527–2532, 1978.

[158] S. Coriani, C. Hättig, P. Jørgensen, A. Halkier, and A. Rizzo. Coupled cluster calculations of Verdet constants. *Chem. Phys. Lett.*, 281(4–6): 445–451, 1997.

[159] E. Botek, B. Champagne, P. Gangopadhyay, A. Persoons, and T. Verbiest. Theoretical Evaluation of the Faraday Effect in Organic Compounds. *Computing Lett.*, 3(2–4):193–200, 2007.

[160] A. B. Villaverde and D. A. Donatti. Verdet constant of liquids; measurements with a pulsed magnetic field. *J. Chem. Phys.*, 71(10): 4021–4024, 1979.

[161] K. Isai, M. Suwa, and H. Watarai. Pulsed Magnetic Field Faraday Imaging of Diamagnetic Liquids. *Anal. Sci.*, 25(1):1–3, 2009.

[162] S. Egami and H. Watarai. Microscopic Faraday rotation measurement system using pulsed magnetic fields. *Rev. Sci. Instrum.*, 80(9):093705, 2009.

[163] D. R. Lide, editor. *CRC Handbook of Chemistry and Physics, 90th Edition*. CRC Press, 90 edition, 2009. ISBN 9781420090840.

[164] DALTON, a molecular electronic structure program, Release Dalton2011, 2011.

[165] NIST Computational Chemistry Comparison and Benchmark Database, NIST Standard Reference Database Number 101 Release 15b, Editor: Russell D. Johnson III, 2011.

[166] G. A. Bain and J. F. Berry. Diamagnetic Corrections and Pascal's Constants. *J. Chem. Edu.*, 85(4):532, 2008.

[167] L. Mu, C. Feng, and H. He. Modeling Diamagnetic Susceptibilities of Organic Compounds with a Novel Connectivity Index. *Ind. Eng. Chem. Res.*, 47(7):2428–2433, 2008.

[168] L. B. Kier and L. H. Hall. *Molecular connectivity in chemistry and drug research*. Academic Press, 1976. ISBN 9780124065604.

[169] H. Takeda and S. John. Compact optical one-way waveguide isolators for photonic-band-gap microchips. *Phys. Rev. A*, 78(2):023804, 2008.

[170] K. Bohnert, P. Gabus, J. Kostovic, and H. Brändle. Optical fiber sensors for the electric power industry. *Opt. Laser Eng.*, 43(3–5):511–526, 2005.

[171] E. Bullmore and O. Sporns. Complex brain networks: graph theoretical analysis of structural and functional systems. *Nat. Rev. Neurosci.*, 10(3): 186–198, 2009.

[172] A. I. Lvovsky, B. C. Sanders, and W. Tittel. Optical quantum memory. *Nat. Photonics*, 3(12):706–714, 2009.

[173] P. Hansen, K. Witter, and W. Tolksdorf. Magnetic and magneto-optical properties of bismuth-substituted gadolinium iron garnet films. *Phys. Rev. B*, 27(7):6608, 1983.

[174] M. Huang and S.-Y. Zhang. Growth and characterization of cerium-substituted yttrium iron garnet single crystals for magneto-optical applications. *Appl. Phys. A-Mater.*, 74(2):177–180, 2002.

[175] G. Abulafya and H. Le Gall. Temperature dependence of the octahedral and tetrahedral magnetooptical coefficients in YIG. *Solid State Commun.*, 11(5):629–633, 1972.

[176] L. R. Dalton. Organic electro-optic materials. *Pure Appl. Chem.*, 76(7–8): 1421–1433, 2004.

[177] M. Jaszunski, P. Jørgensen, A. Rizzo, K. Ruud, and T. Helgaker. MCSCF calculations of Verdet constants. *Chem. Phys. Lett.*, 222(3):263–266, 1994.

[178] M. Kimura, H. Kondo, and S. Hattori. Characteristic of Magnetic Rotation Spectra at Singlet–Triplet Transition Frequencies. *J. Phys. Soc. Jpn.*, 20 (10):1778–1782, 1965.

[179] W. H. Eberhardt and H. Renner. The magnetic rotation spectrum of singlet–triplet transitions. *J. Mol. Spectrosc.*, 6:483–491, 1961.

[180] B. S. Snowden Jr. and W. H. Eberhardt. Magnetic rotation spectrum of singlet–triplet transitions: Part II. Pyrazine. *J. Mol. Spectrosc.*, 18(4): 372–383, 1965.

[181] S. H. Brown and Y.-N. Chiu. Spin-dependent magneto-optical rotation for free radicals and for singlet–triplet transitions. *J. Chem. Phys.*, 69(8): 3579–3588, 1978.

[182] G. Hennrich, A. Omenat, I. Asselberghs, S. Foerier, K. Clays, T. Verbiest, and J. L. Serrano. Liquid Crystals from C_3-Symmetric Mesogens for Second-Order Nonlinear Optics. *Angew. Chem. Int. Ed.*, 45(25):4203–4206, 2006.

[183] L. de Vega, S. van Cleuvenbergen, G. Depotter, E. M. García-Frutos, B. Gómez-Lor, A. Omenat, R. M. Tejedor, J. L. Serrano, G. Hennrich, and K. Clays. Nonlinear Optical Thin Film Device from a Chiral Octopolar Phenylacetylene Liquid Crystal. *J. Org. Chem.*, 77(23):10891–10896, 2012.

[184] Turbomole, version 5.7.1; Quantum Chemistry Group, University of Karlsruhe: Karlsruhe, Germany, 2005.

[185] R. Ahlrichs, M. Bär, M. Häser, H. Horn, and C. Kölmel. Electronic structure calculations on workstation computers: The program system turbomole. *Chem. Phys. Lett.*, 162(3):165–169, 1989.

[186] A. D. Becke. Density-functional exchange-energy approximation with correct asymptotic behavior. *Phys. Rev. A*, 38(6):3098–3100, 1988.

[187] J. P. Perdew. Density-functional approximation for the correlation energy of the inhomogeneous electron gas. *Phys. Rev. B*, 33(12):8822–8824, 1986.

[188] J. P. Perdew. Erratum: Density-functional approximation for the correlation energy of the inhomogeneous electron gas. *Phys. Rev. B*, 34(10):7406–7406, 1986.

[189] F. Weigend and R. Ahlrichs. Balanced basis sets of split valence, triple zeta valence and quadruple zeta valence quality for H to Rn: Design

and assessment of accuracy. *Phys. Chem. Chem. Phys.*, 7(18):3297–3305, 2005.

[190] A. D. Becke. Density-functional thermochemistry. III. the role of exact exchange. *J. Chem. Phys.*, 98(7):5648–5652, 1993.

[191] C. Lee, W. Yang, and R. G. Parr. Development of the Colle–Salvetti correlation–energy formula into a functional of the electron density. *Phys. Rev. B*, 37(2):785–789, 1988.

[192] P. J. Stephens, F. J. Devlin, C. F. Chabalowski, and M. J. Frisch. Ab Initio Calculation of Vibrational Absorption and Circular Dichroism Spectra Using Density Functional Force Fields. *J. Chem. Phys.*, 98(45): 11623–11627, 1994.

[193] M. J. G. Peach, M. J. Williamson, and D. J. Tozer. Influence of Triplet Instabilities in TDDFT. *J. Chem. Theory Comput.*, 7(11):3578–3585, 2011.

[194] I. Tamm. Relativistic interaction of elementary particles. *J. Phys.(USSR)*, 9:449, 1945.

[195] S. M. Dancoff. Non-Adiabatic Meson Theory of Nuclear Forces. *Phys. Rev.*, 78(4):382–385, 1950.

[196] M. M. Oliva, J. Casado, J. T. López Navarrete, G. Hennrich, S. van Cleuvenbergen, I. Asselberghs, K. Clays, M. C. Ruiz Delgado, J.-L. Brédas, J. S. Seixas de Melo, and L. De Cola. Synthesis, Spectroscopy, Nonlinear Optics, and Theoretical Investigations of Thienylethynyl Octopoles with a Tunable Core. *Chem.-Eur. J.*, 15(33):8223–8234, 2009.

[197] V. Ho, B. W. Boudouris, and R. A. Segalman. Tuning Polythiophene Crystallization through Systematic Side Chain Functionalization. *Macromolecules*, 43(19):7895–7899, 2010.

[198] G. Hennrich, R. Tejedor, J. Serrano, and F. Ramirez. Chiral response from achiral discotic liquid crystals. *Langmuir, submitted*, 2013.

[199] R. H. Kodama. Magnetic nanoparticles. *J. Magn. Magn. Mater.*, 200 (1–3):359–372, 1999.

[200] L. Zhou, J. Yuan, and Y. Wei. Core–shell structural iron oxide hybrid nanoparticles: from controlled synthesis to biomedical applications. *J. Mater. Chem.*, 21(9):2823–2840, 2011.

[201] D.-X. Chen, O. Pascu, A. Roig, and A. Sanchez. Size analysis and magnetic structure of nickel nanoparticles. *J. Magn. Magn. Mater.*, 322 (24):3834–3840, 2010.

[202] Q. A. Pankhurst, J. Connolly, S. K. Jones, and J. Dobson. Applications

of magnetic nanoparticles in biomedicine. *J. Phys. D: Appl. Phys.*, 36 (13):R167, 2003.

[203] X. Batlle and A. Labarta. Finite-size effects in fine particles: magnetic and transport properties. *J. Phys. D: Appl. Phys.*, 35(6):R15, 2002.

[204] N. A. Frey, S. Peng, K. Cheng, and S. Sun. Magnetic nanoparticles: synthesis, functionalization, and applications in bioimaging and magnetic energy storage. *Chem. Soc. Rev.*, 38(9):2532–2542, 2009.

[205] A. K. Gupta and M. Gupta. Synthesis and surface engineering of iron oxide nanoparticles for biomedical applications. *Biomaterials*, 26(18): 3995–4021, 2005.

[206] A. Moser, K. Takano, D. T. Margulies, M. Albrecht, Y. Sonobe, Y. Ikeda, S. Sun, and E. E. Fullerton. Magnetic recording: advancing into the future. *J. Phys. D: Appl. Phys.*, 35(19):R157, 2002.

[207] D.-X. Chen, A. Sanchez, E. Taboada, A. Roig, N. Sun, and H.-C. Gu. Size determination of superparamagnetic nanoparticles from magnetization curve. *J. Appl. Phys.*, 105(8):083924–6, 2009.

[208] S. Foner. Versatile and Sensitive Vibrating-Sample Magnetometer. *Rev. Sci. Instrum.*, 30(7):548–557, 1959.

[209] S. Vandeleene, M. Jivanescu, A. Stesmans, J. Cuppens, M. J. Van Bael, H. Yamada, N. Sato, T. Verbiest, and G. Koeckelberghs. Magnetic Properties of Substituted Poly(thiophene)s in Their Neutral State. *Macromolecules*, 43(6):2910–2915, 2010.

[210] V. Salgueiriño-Maceira, M. A. Correa-Duarte, E. Duman, and M. Farle. FePt nanocrystals embedded in methylmethacrylate polymers. *J. Magn. Magn. Mater.*, 299(2):467–471, 2006.

[211] V. K. Valev, A. Kirilyuk, F. Dalla Longa, J. T. Kohlhepp, B. Koopmans, and T. Rasing. Observation of periodic oscillations in magnetization-induced second harmonic generation at the Mn/Co interface. *Phys. Rev. B*, 75(1):012401, 2007.

[212] G. Rosa, H. Guerrero, D. Levy, A. Álvarez-Herrero, and R. P. del Real. Surface effects in magnetic nanoparticles measured by means of a magneto-optical method. *J. Appl. Phys.*, 97(6):064314–5, 2005.

[213] F. Hussain, M. Hojjati, M. Okamoto, and R. E. Gorga. Review article: Polymer-matrix Nanocomposites, Processing, Manufacturing, and Application: An Overview. *J. Compos. Mater.*, 40(17):1511–1575, 2006.

[214] J. B. Goodenough and Y. Kim. Challenges for Rechargeable Li Batteries. *Chem. Mater.*, 22(3):587–603, 2010.

[215] Y. F. Joya, Z. Liu, K. S. Joya, and T. Wang. Preparation and antibacterial properties of laser-generated silver–anatase nanocomposite film against *Escherichia coli* and *Staphylococcus aureus*. *Nanotechnology*, 23(49): 495708, 2012.

[216] H. Wu, B. Xu, A. Liu, and G. Chai. Strain-modulated magnetocapacitance of vertical ferroelectric–ferromagnetic nanocomposite heteroepitaxial films. *J. Phys. D: Appl. Phys.*, 45(45):455306, 2012.

[217] G. Vleminckx, S. Bose, J. Leys, J. Vermant, M. Wübbenhorst, A. A. Abdala, C. Macosko, and P. Moldenaers. Effect of Thermally Reduced Graphene Sheets on the Phase Behavior, Morphology, and Electrical Conductivity in Poly[(α-methyl styrene)-co-(acrylonitrile)/poly(methyl-methacrylate) Blends. *ACS Appl. Mater. Interfaces*, 3(8):3172–3180, 2011.

[218] Science Policy Section. Nanoscience and nanotechnologies: opportunities and uncertainties. Technical report, The Royal Society & the Royal Academy of Engineering, 2004. URL `http://www.nanotec.org.uk/finalReport.htm`.

[219] T. M. Buzug and J. Borgert, editors. *Magnetic Particle Imaging: A Novel SPIO Nanoparticle Imaging Technique*, volume 140. Springer Berlin Heidelberg, 2012.

[220] B. Gleich and J. Weizenecker. Tomographic imaging using the nonlinear response of magnetic particles. *Nature*, 435(7046):1214–1217, 2005.

[221] S.-H. Chung, M. Grimsditch, A. Hoffmann, S. D. Bader, J. Xie, S. Peng, and S. Sun. Magneto-optic measurement of Brownian relaxation of magnetic nanoparticles. *J. Magn. Magn. Mater.*, 320(3–4):91–95, 2008.

[222] M. Xu and P. J. Ridler. Linear dichroism and birefringence effects in magnetic fluids. *J. Appl. Phys.*, 82(1):326–332, 1997.

[223] D. M. Hawkins. The Problem of Overfitting. *J. Chem. Inf. Comp. Sci.*, 44(1):1–12, 2004.

[224] G. F. Goya, T. S. Berquó, F. C. Fonseca, and M. P. Morales. Static and dynamic magnetic properties of spherical magnetite nanoparticles. *J. Appl. Phys.*, 94(5):3520–3528, 2003.

[225] J. S. Beveridge, J. R. Stephens, and M. E. Williams. The Use of Magnetic Nanoparticles in Analytical Chemistry. *Annu. Rev. Anal. Chem.*, 4: 251–273, 2011.

[226] A.-H. Lu, E. L. Salabas, and F. Schüth. Magnetic Nanoparticles: Synthesis, Protection, Functionalization, and Application. *Angew. Chem. Int. Ed.*, 46(8):1222–1244, 2007.

[227] E. Katz and I. Willner. Integrated Nanoparticle–Biomolecule Hybrid Systems: Synthesis, Properties, and Applications. *Angew. Chem. Int. Ed.*, 43(45):6042–6108, 2004.

[228] I. V. Kityk, J. Ebothé, I. Fuks-Janczarek, A. A. Umar, K. Kobayashi, M. Oyama, and B. Sahraoui. Nonlinear optical properties of Au nanoparticles on indium–tin oxide substrate. *Nanotechnology*, 16(9): 1687, 2005.

[229] M. M. Kauranen, T. Verbiest, A. Persoons, E. W. Meijer, M. N. Teerenstra, A. J. Schouten, R. J. M. Nolte, and E. E. Havinga. Chiral effects in the second-order optical nonlinearity of a poly(isocyanide) monolayer. *Adv. Mater.*, 7(7):641–644, 1995.

[230] P. S. Pershan. Nonlinear Optical Properties of Solids: Energy Considerations. *Phys. Rev.*, 130(3):919–929, 1963.

[231] R.-P. Pan, H. D. Wei, and Y. R. Shen. Optical second-harmonic generation from magnetized surfaces. *Phys. Rev. B*, 39(2):1229–1234, 1989.

[232] A. Kirilyuk and T. Rasing. Magnetization-induced-second-harmonic generation from surfaces and interfaces. *J. Opt. Soc. Am. B*, 22(1): 148–167, 2005.

[233] V. K. Valev, M. Gruyters, A. Kirilyuk, and T. Rasing. Direct Observation of Exchange Bias Related Uncompensated Spins at the CoO/Cu Interface. *Phys. Rev. Lett.*, 96(6):067206, 2006.

[234] O. A. Aktsipetrov, T. V. Murzina, E. M. Kim, R. V. Kapra, A. A. Fedyanin, M. Inoue, A. F. Kravets, S. V. Kuznetsova, M. V. Ivanchenko, and V. G. Lifshits. Magnetization-induced second- and third-harmonic generation in magnetic thin films and nanoparticles. *J. Opt. Soc. Am. B*, 22(1):138–147, 2005.

[235] L. L. Beecroft and C. K. Ober. Nanocomposite Materials for Optical Applications. *Chem. Mater.*, 9(6):1302–1317, 1997.

[236] I. A. Kolmychek, T. V. Murzina, S. Fourier, J. Wouters, V. K. Valev, T. Verbiest, and O. A. Aktsipetrov. Second Harmonic Generation in Core (Shell) γ-Fe_2O_3 (Au) Nanoparticles. *Sol. St. Phen.*, 152–153:508–511, 2009.

[237] J. Wouters, O. I. Lebedev, G. V. Tendeloo, H. Yamada, N. Sato, J. Vanacken, V. V. Moshchalkov, T. Verbiest, and V. K. Valev. Preparing polymer films doped with magnetic nanoparticles by spin-coating and melt-processing can induce an in-plane magnetic anisotropy. *J. Appl. Phys.*, 109(7):076105, 2011.

[238] J. J. Maki, M. Kauranen, and A. Persoons. Surface second-harmonic generation from chiral materials. *Phys. Rev. B*, 51(3):1425–1434, 1995.

[239] J. J. Maki, M. Kauranen, T. Verbiest, and A. Persoons. Uniqueness of wave-plate measurements in determining the tensor components of second-order surface nonlinearities. *Phys. Rev. B*, 55(8):5021–5026, 1997.

[240] V. K. Valev, M. Gruyters, A. Kirilyuk, and T. Rasing. Influence of quadratic contributions in magnetization-induced second harmonic generation studies of magnetization reversal. *Phys. Status Solidi B*, 242 (15):3027–3031, 2005.

[241] A. Pais. *Subtle is the Lord: The Science and the Life of Albert Einstein*. OUP Oxford, 2005. ISBN 9780192806727.

[242] J. L. Synge and A. Schild. *Tensor Calculus*. Dover Publications, 1978. ISBN 9780486636122.

[243] U. C. De, A. A. Shaikh, and J. Sengupta. *Tensor Calculus*. Alpha Science International Limited, 2008. ISBN 9781842654484.

[244] D. F. Lawden. *Introduction to Tensor Calculus, Relativity, and Cosmology*. Dover Publications, 1982. ISBN 9780486132143.

Health, safety & environment considerations

At the KU Leuven Association, the Health, Safety & Environment (HSE) department attempts to support researchers in defining the constraints of health, safety and environment. By doing this they try to reduce the risks for the researchers to a minimum. As a part of the KU Leuven, the Laboratory for Molecular Imaging and Photonics is required to implement the relevant safety protocols. For the work presented in this dissertation, the relevant HSE risks and safety protocols are those concerning chemical, laser and magnet safety.

Chemical safety concerns safety during the entire process, starting with acquiring the chemical products, going over storage and the actual use of the chemicals to disposing of the waste. Before starting any chemical experiment, however small or seemingly riskless, a risk analysis must be completely filled in and correctly classified or submitted to the relevant safety officers. In order to ensure that no confusion is possible, the researcher must clearly write down in their lab book before each experiment which risk analyses are relevant. During all work with chemicals and/or in the laboratory, a lab coat and safety goggles must be worn, and when necessary gloves are also used.

Laser safety is very important in the Laboratory for Molecular Imaging and Photonics as there are many high power, class 3B and class 4 lasers present. In order to minimize the risks, a laser safety training is mandatory. I attended a laser safety training organized by Newport, on October 14th 2010, in order to receive the necessary training. Key points of laser safety are always wearing safety goggles appropriate for the laser in use, constantly taking into account and blocking or minimizing reflections and never allowing reflective objects (such as watches or rings) near the laser beam. A final crucial element is a red warning light outside the door indicating to others that the room is not safe to enter due to the fact that a high power laser is in operation.

Magnet safety concerns both risks for people and devices. The most important effect is the attraction of magnetic objects in or on the body by the magnetic field, which can cause serious injury. Special care must be taken with pacemakers, which not only can be attracted by a magnetic field but can also be reprogrammed or disturbed by a magnetic field.

List of publications

Articles in internationally peer reviewed academic journals

- Nonlinear superchiral meta-surfaces: tuning chirality and disentangling non-reciprocity at the nanoscale
  Advanced Materials (2014), in press
  V. K. Valev, J. J. Baumberg, B. De Clercq, N. Braz, X. Zheng, E. J. Osley, **S. Vandendriessche**, M. Hojeij, C. Blejean, J. Mertens, C. G. Biris, V. Volskiy, M. Ameloot, Y. Ekinci, G. A. E. Vandenbosch, P. A. Warburton, V. V. Moshchalkov, N. C. Panoiu, T. Verbiest

- Anisotropy versus circular dichroism in second harmonic generation from fourfold symmetric arrays of G-shaped nanostructures
  Physical Review B (2014), 89, 121113
  E. A. Mamonov, I. A. Kolmychek, **S. Vandendriessche**, M. Hojeij, Y. Ekinci, V. K. Valev, T. Verbiest and T. V. Murzina

- Sandwich Approach toward Inverse Opals with Linear and Nonlinear Optical Functionalities
  ACS Applied Materials & Interfaces (2014), 6 (6), 3870–3878
  P.-J. Demeyer, **S. Vandendriessche**, S. Van Cleuvenbergen, S. Carron, K. Bogaerts, T. N. Parac-Vogt, T. Verbiest and K. Clays

- Poly(3-alkylthiophene)s show unexpected second-order nonlinear optical response
  Chemical Communications (2014), 50 (21), 2741–2743
  S. Deckers, **S. Vandendriessche**, D. Cornelis, F. Monnaie, G. Koeckelberghs, I. Asselberghs, T. Verbiest and M. A. van der Veen

- Synthesis and Characterization of Holmium-Doped Iron Oxide Nanoparticles
  Materials (2014), 7 (2), 1155–1164
  M. Bloemen, **S. Vandendriessche**, V. Goovaerts, W. Brullot, M. K. Vanbel, S. Carron, N. Geukens, T. Parac-Vogt and T. Verbiest

- Magneto-optical harmonic susceptometry of superparamagnetic materials
  Applied Physics Letters (2013), 102 (16), 161903
  S. Vandendriessche, W. Brullot, D. Slavov, V. K. Valev and T. Verbiest

- Giant Faraday Rotation in Mesogenic Organic Molecules
  Chemistry of Materials (2013), 25 (7), 1139–1143
  S. Vandendriessche, S. Van Cleuvenbergen, P. Willot, G. Hennrich, M. Srebro, V. K. Valev, G. Koeckelberghs, K. Clays, J. Autschbach and T. Verbiest

- The role of chiral local field enhancements below the resolution limit of Second Harmonic Generation microscopy
  Optics Express (2012), 20 (1), 256–264
  V. K. Valev, B. Clercq, X. Zheng, D. Denkova, E. Osley, **S. Vandendriessche**, A. Silhanek, V. Volskiy, P. Warburton, G. Vandenbosch, M. Ameloot, V. Moshchalkov and T. Verbiest

- Faraday rotation and its dispersion in the visible region for saturated organic liquids
  Physical Chemistry Chemical Physics (2012), 14 (6), 1860–1864
  S. Vandendriessche, V. K. Valev and T. Verbiest

- Distributing the Optical Near-Field for Efficient Field-Enhancements in Nanostructures
  Advanced Materials (2012), 24 (35), OP208–OP215
  V. K. Valev, B. De Clercq, C. Biris, X. Zheng, **S. Vandendriessche**, M. Hojeij, D. Denkova, Y. Jeyaram, N. Panoiu, Y. Ekinci, A. Silhanek, V. Volskiy, G. Vandenbosch, M. Ameloot, V. Moshchalkov and T. Verbiest

- Characterization of magnetization-induced second harmonic generation in iron oxide polymer nanocomposites
  Applied Optics (2012), 51 (2), 209–213
  S. Vandendriessche, V. K. Valev and T. Verbiest

- Adsorption Kinetics of Ultrathin Polymer Films in the Melt Probed by Dielectric Spectroscopy and Second-Harmonic Generation
  Langmuir (2011), 27 (22), 13533–13538
  C. Rotella, S. Napolitano, **S. Vandendriessche**, V. K. Valev, T. Verbiest, M. Larkowska, S. Kucharski and M. Wübbenhorst

Papers at international scientific conferences and symposia, published in full in proceedings

- Photoelastic modulator non-idealities in magneto-optical polarization measurements
  In Shaw, J. A. (Ed.), LeMaster, D. A. (Ed.), Polarization Science and Remote Sensing VI: Vol. 8873. Optics and Photonics, San Diego, USA, Aug 25, 2013 (pp. 88730Z1–88730Z11)
  S. Vandendriessche and T. Verbiest

- Magneto-optical Characterization of Magnetic-Plasmonic Gold-Magnetite Hybrid Nanoparticle Networks (AuMag-HyNANs)
  In Kang, I. (Ed.), Reitze, D. (Ed.), Alic, N. (Ed.), and Hagan, D. (Ed.), Quantum Electronics II: Vol. FTh4C. Frontiers in Optics, Orlando, USA, Oct 6–10, 2013 (pp. FTh4C.1)
  W. Brullot, **S. Vandendriessche** and T. Verbiest

- Fast Fourier-Transform Second-Harmonic Generation (FFT-SHG) Provides a Solution for Measuring Nonlinear Effects on Fragile Structures
  In Kang, I. (Ed.), Reitze, D. (Ed.), Alic, N. (Ed.), and Hagan, D. (Ed.), Microscopy and OCT: Vol. FTu2F. Frontiers in Optics, Orlando, USA, Oct 6–10, 2013 (pp. FTu2F.5)
  M. K. Vanbel, R. Paesen, W. Brullot, **S. Vandendriessche**, I. Asselberghs, K. Markey, P. Valvekens, M. van der Veen, D. De Vos, M. Ameloot, V. K. Valev, J.-P. Locquet, and T. Verbiest

- Magneto-optical effects in clusters of superparamagnetic iron oxide and plasmonic gold nanoparticles
  In CLEO: 2013. Conference on Lasers and Electro-Optics, San Jose, USA, Jun 9–14, 2013 (pp. JTu4A.77)
  W. Brullot, **S. Vandendriessche** and T. Verbiest

- Second-harmonic generation from complex chiral samples
  In 17th International school on quantum electronics: laser physics and applications: Vol. 8770. ISQE, Nessebar: Bulgaria, Sep 24–28, 2012 (pp. 87701F–87701F)
  M. K. Vanbel, **S. Vandendriessche**, M. Van der Veen, D. Slavov, P. Heister, R. Paesen, V. K. Valev, M. Ameloot and T. Verbiest

- Switching Faraday rotation on a molecular level
  In Eggleton, B. (Ed.), Gaeta, A. (Ed.), Broderick, N. (Ed.), Nonlinear optics and applications VI: Vol. 8434. SPIE Europe, Brussels, Belgium, Apr 16–18, 2012 (pp. 84341E1–84341E6)
  S. Vandendriessche, W. Brullot and T. Verbiest

- Spectral measurements to probe the magneto-optical properties of commonly used organic dyes
  In Eggleton, B. (Ed.), Gaeta, A. (Ed.), Broderick, N. (Ed.), Nonlinear optics and applications VI: Vol. 8434. SPIE Europe, Brussels, Belgium, Apr 16–18, 2012 (pp. 84341G1–84341G9)
  W. Brullot, **S. Vandendriessche** and T. Verbiest

Meeting abstracts, presented at international scientific conferences and symposia, published or not published in proceedings or journals

- An ac magnetic field technique to optically characterize superparamagnetism
  CC3DMR. Jeju Island, South Korea, 24–28 June 2013
  S. Vandendriessche and T. Verbiest

- Second harmonic generation from chiral gold nanoparticles
  NLO - 50 Years of Nonlinear Optics International Symposium. Barcelona, 8–10 October 2012
  S. Vandendriessche, V. K. Valev and T. Verbiest

FACULTY OF SCIENCE
DEPARTMENT OF CHEMISTRY
MOLECULAR IMAGING AND PHOTONICS
Celestijnenlaan 200D box 2425
B-3001 Heverlee